



# Acoustic near field of a contra-rotating propeller in wetted conditions

Antonio Posa<sup>1</sup> , Alessandro Capone<sup>1</sup>, Francisco Alves Pereira<sup>1</sup>,  
Fabio Di Felice<sup>1</sup> and Riccardo Broglio<sup>1</sup> 

<sup>1</sup>CNR-INM, Institute of Marine Engineering, National Research Council of Italy, Via di Vallerano 139, 00128 Roma, Italy

**Corresponding author:** Antonio Posa, [antonio.posa@cnr.it](mailto:antonio.posa@cnr.it)

(Received 29 May 2024; revised 20 December 2024; accepted 28 December 2024)

---

The acoustic field radiated by a system of contra-rotating propellers in wetted conditions (with no cavitation) is reconstructed by exploiting the Ffowcs Williams–Hawkings acoustic analogy and a database of instantaneous realizations of the flow. They were generated by high-fidelity computations using a large eddy simulation approach on a cylindrical grid of 4.6 billion points. Results are also compared against the cases of the front and rear propellers working alone. The analysis shows that the importance of the quadrupole component of sound, originating from wake turbulence and instability of the tip vortices, is reinforced, relative to the linear component radiated from the surface of the propeller blades. The sound from the contra-rotating propellers decays at a slower rate for increasing radial distances, compared with the cases of the isolated front and rear propellers, again due to the quadrupole component. The quadrupole sound is often neglected in the analysis of the acoustic signature of marine propellers, by considering the only linear component. In contrast, the results of this study point out that the quadrupole component becomes the leading one in the case of contra-rotating propulsion systems, due to the increased complexity of their wake. This is especially the result of the mutual inductance phenomena between the tip vortices shed by the front and rear propellers of the contra-rotating system.

**Key words:** hydrodynamic noise, turbulence simulation, wakes

---

## 1. Introduction

Contra-rotating propellers are a propulsion system aimed at achieving improved performance, in comparison with isolated propellers. Typically the flow through a propeller gains both axial and azimuthal momentum. While the former is useful to produce

© The Author(s), 2025. Published by Cambridge University Press. This is an Open Access article, distributed under the terms of the Creative Commons Attribution licence (<https://creativecommons.org/licenses/by/4.0/>), which permits unrestricted re-use, distribution and reproduction, provided the original article is properly cited.

thrust, the latter is actually wasted and is a source of unwanted lateral loads. The underlying idea of contra-rotating propulsion systems consists in using a rear propeller to recover the azimuthal momentum gained by the flow through the front propeller.

Despite the potential benefits of contra-rotating propellers, our understanding of their flow physics is much more limited, in comparison with more conventional propulsion systems. This limitation comes from the technical challenges of performing both experiments and numerical simulations on this subject. Therefore, while to date several studies were able to tackle the problem of the flow through and downstream of isolated propellers (Felli *et al.* 2006, 2008, 2011; Liefvendahl 2010; Baek *et al.* 2015; Balaras, Schroeder & Posa 2015; Kumar & Mahesh 2017; Posa *et al.* 2019; Posa, Broglia & Balaras 2022; Ahmed, Croaker & Doolan 2020; Villa *et al.* 2020; Wang *et al.* 2021; Wang, Liu & Wu 2022*b*; Wang, Luo & Li 2022*c*; Wang *et al.* 2022*a*; Abbasi *et al.* 2023; Kan, Li & Yang 2023; Posa 2023*a*), the research on contra-rotating propellers is still at its early stages. In addition, works on contra-rotating propellers are usually limited to the analysis of their global performance (Min, Chang & Seo 2009; Grassi *et al.* 2010; Chang & Go 2011; Xiong *et al.* 2016; Su & Kinnas 2017; Su, Kinnas & Jukola 2017; Khan *et al.* 2018; Nouri, Mohammadi & Zarezadeh 2018; Huang *et al.* 2019; Hou *et al.* 2021; Tadros, Ventura & Guedes Soares 2022). Only a few exceptions (Paik *et al.* 2015; Hu *et al.* 2019; Zhang *et al.* 2019, 2020) provide some more insight about their flow features, which are much more complex than those of isolated propellers. This increased complexity is especially the result of the interaction between the helical tip vortices shed by the front and rear propellers. This interaction originates a system of isolated vortex rings just downstream of the rear propeller, as revealed by the recent experimental studies by Capone & Alves Pereira (2020), Capone, Di Felice & Alves Pereira (2021) and Alves Pereira, Capone & Di Felice (2021) and the large eddy simulation (LES) computations by Posa *et al.* (2024).

A major issue of marine propulsion is represented by its environmental impact through its acoustic signature (Vakili, Ölçer & Ballini 2021; Chahouri, Elouahmani & Ouchene 2022; Smith & Rigby 2022). This is also problematic for the stealth capabilities of military vessels. As acknowledged in the literature, the ability to capture the complex wake features of marine propellers is important for the accurate reconstruction of their acoustic emission (Cianferra *et al.* 2019*b*; Cianferra & Armenio 2021; Kimmerl, Mertes & Abdel-Maksoud 2021; Posa, Broglia & Felli 2022*c*). The several flow structures populating the wake have indeed an impact on noise through the quadrupole component of sound. This cannot be neglected *a priori*, compared with the linear component radiated from the surface of the blades, as typical in the field of aeroacoustics. In aeroacoustics the quadrupole sound is indeed expected to be negligible as long as the values of the Mach number keep in the low subsonic regime (see, for instance, Glegg & Devenport 2017). It becomes significant only starting from the high subsonic regime, playing an important role in the definition of the overall acoustic field (Lowson 1965; Hanson & Fink 1979; Ardavan 1991; Peake & Crighton 1991; Envia 1994; Farassat & Brentner 1998*a,b*; Ianniello 1999; Taghaddosi & Agarwal 2000; Brentner & Farassat 2003; Brentner & Farassat 2003). For aeronautical contra-rotating propellers, the problem has been investigated by Hanson (1985).

To date, a number of studies were reported on the acoustic signature of marine propellers (see, for instance, Lidtke *et al.* 2016, 2022; Özden *et al.* 2016; Viitanen *et al.* 2018; Ku *et al.* 2021; Sezen *et al.* 2021*a,b*; Stark & Shi 2021; Sezen & Atlar 2023), exploiting high-fidelity, eddy-resolving methodologies to resolve the flow and the acoustic analogy (Lighthill 1952) to reconstruct the acoustic field in post-process. They are based on the assumption that the hydroacoustic phenomena have a negligible impact on the fluid dynamics. Therefore, it is legitimate to resolve the fluid dynamics without taking into account the acoustic phenomena and then using the database of instantaneous realizations

of the solution for the computation of the acoustic field. However, in contrast with the field of the aeroacoustics of contra-rotating aeronautical rotors (Blandeau & Joseph 2010; Akkermans, Stuermer & Delfs 2016; Kingan & Parry 2019, 2020a,b; Parry & Kingan 2019, 2021; McKay *et al.* 2021; Chaitanya *et al.* 2022; Smith, Filippone & Barakos 2022; Chen *et al.* 2023; Casagrande Hirono, Robertson & Torija Martinez 2024; Casagrande Hirono *et al.* 2024), studies on the acoustic characterization of contra-rotating marine propellers are practically missing in the literature. To the authors' knowledge, the only work on the subject is due to Hu *et al.* (2021). They adopted a detached eddy simulation approach to resolve the flow through a contra-rotating propeller, using a multi-block grid consisting of almost 7 million cells. They were able to reconstruct the sound radiated from the propellers in both non-cavitating and cavitating conditions. They verified, besides the expected increase of the sound pressure levels (SPLs) in cavitating conditions, the generation of a more isotropic acoustic radiation pattern, compared with the non-cavitating case: in the latter condition noise was found more intense in the axial direction than in the radial one. However, this study was limited to the acoustic field in the vicinity of the propellers, within five diameters from them, and considered the only contribution of the linear component of sound, radiated from the surface of their blades. No details were provided on both the wake features and the quadrupole component of the acoustic signature originating from them. However, this may be expected to be even more important than for isolated propellers, due to the intense shear developing between the wake structures shed by the two propellers of the contra-rotating system.

In the present work, results of numerical computations, carried out by LES in the framework of one of our earlier studies (Posa *et al.* 2024), are utilized to reconstruct the acoustic field of contra-rotating propellers, providing also details on the flow physics: the database of instantaneous realizations of the solution allowed us to compute the acoustic pressure by exploiting the Ffowcs Williams–Hawkings (FWH) acoustic analogy (Ffowcs Williams & Hawkings 1969). Thanks to an immersed-boundary (IB) methodology (Balaras 2004; Yang & Balaras 2006), a cylindrical grid consisting of about 4.6 billion points was adopted, which is three orders of magnitude more extensive than in the studies available in the current literature on the subject. In contrast with the majority of the works in the field, the quadrupole component of sound radiated from the near wake is also included, which is especially important in this case, because of the complexity of the flow structures originating from the interplay between the tip vortices shed by the front and rear propellers. The exploitation of the direct formulation of the acoustic analogy, in contrast with the more typical permeable formulation (Di Francescantonio 1997), allowed us to separate the contributions to the acoustic signature attributable to the front and rear propellers as well as that from the wake flow. A detailed reconstruction of the acoustic field is provided, by using a large number of hydrophones (about 6000), up to 128 diameters away from the contra-rotating system. In addition, comparisons with the cases of the two front and rear propellers working alone are given, which are helpful in isolating the effect of the interaction between them on both their fluid dynamics and radiated sound. Also comparisons against the results of experiments on the fluid dynamics of the same system are presented (Capone & Alves Pereira 2020; Capone *et al.* 2021; Alves Pereira *et al.* 2021), for validation purposes.

This paper is organized as follows: § 2 describes the methodology used throughout the paper, § 3 presents the flow problem, § 4 discusses the set-up of the LES computations and § 5 the set-up of the acoustic post-process, § 6 presents the results of both the fluid dynamics and hydro-acoustics of the system, and § 7 summarizes the conclusions of this study.

## 2. Methodology

### 2.1. Solution of the fluid dynamics

The filtered Navier–Stokes equations (NSEs) for incompressible flows were resolved in non-dimensional form:

$$\frac{\partial \tilde{u}_i}{\partial x_i} = 0, \quad i = 1, 2, 3, \quad (2.1)$$

$$\frac{\partial \tilde{u}_i}{\partial t} + \frac{\partial \tilde{u}_i \tilde{u}_j}{\partial x_j} = -\frac{\partial \tilde{p}}{\partial x_i} - \frac{\partial \tau_{ij}}{\partial x_j} + \frac{1}{Re} \frac{\partial^2 \tilde{u}_i}{\partial x_j^2} + f_i, \quad i, j = 1, 2, 3, \quad (2.2)$$

where  $x_i$  is the coordinate in space in the direction  $i$ ,  $t$  is time,  $\tilde{u}_i$  is the filtered velocity component in the direction  $i$  and  $\tilde{p}$  is the filtered pressure. The Reynolds number is defined as  $Re = \mathcal{V}\mathcal{L}/\nu$ , where  $\mathcal{V}$  and  $\mathcal{L}$  are the reference velocity and length scales, respectively, while  $\nu$  is the kinematic viscosity of the fluid. The quantity  $\tau_{ij} = \overline{u_i u_j} - \tilde{u}_i \tilde{u}_j$  is the sub-grid scale (SGS) stress tensor, while  $f_i$  is a forcing term, representing the action of the bodies immersed within the flow on the fluid.

The SGS tensor,  $\tau_{ij}$ , results from filtering the NSEs, practically by resolving them on a computational grid that is coarser than the smallest scale of the flow (the Kolmogorov scale). This is always the case at the typical Reynolds numbers of flows of interest in engineering, as in the current study. Therefore, the SGS tensor represents the action of the unresolved scales, smaller than the grid spacing, on the resolved ones. It requires to be modelled. In this work, we adopted the wall-adaptive local eddy-viscosity (WALE) model, developed by Nicoud & Ducros (1999). This is an eddy-viscosity model, which assumes that the deviatoric part of the SGS tensor,  $\tau_{ij}^d$ , and the deformation tensor of the resolved velocity field,  $\tilde{S}_{ij}$ , are aligned:

$$\tau_{ij}^d = \tau_{ij} - \frac{1}{3} \delta_{ij} \tau_{kk} = -2\nu_t \tilde{S}_{ij}, \quad i, j = 1, 2, 3. \quad (2.3)$$

Here  $\delta_{ij}$  is the Kronecker delta,  $\tau_{kk}$  is the trace of the SGS tensor and  $\nu_t$  is the eddy viscosity. The assumption in (2.3) reduces the number of unknowns of the problem from six to one, the only eddy viscosity.

The WALE model reconstructs  $\nu_t$  by using the square of the velocity gradient tensor of the resolved velocity field,  $\tilde{G}_{ij}$ :

$$\nu_t = (C_w \Delta)^2 \frac{(\tilde{G}_{ij}^d \tilde{G}_{ij}^d)^{3/2}}{(\tilde{S}_{ij} \tilde{S}_{ij})^{5/2} + (\tilde{G}_{ij}^d \tilde{G}_{ij}^d)^{5/4}}, \quad i, j = 1, 2, 3. \quad (2.4)$$

Here  $C_w = 0.5$  is a constant,  $\Delta$  is the local size of the computational grid, computed as the cubic root of the volume of its cells, while  $\tilde{G}_{ij}^d$  represents the deviatoric part of  $\tilde{G}_{ij}$ . This model was designed by Nicoud & Ducros (1999) to reproduce the correct limiting trend of the eddy viscosity in the near wall region, behaving like  $x_n^3$ , where  $x_n$  is the local distance from the wall, without the need of *ad hoc* corrections, which may be problematic to implement in case of complex geometries. In addition, (2.4) results properly in  $\nu_t = 0$  in regions of laminar gradients without turbulence. Furthermore, the WALE model requires only local information on the resolved field, which is beneficial in terms of computational cost. It was successfully utilized in several earlier studies dealing with the wake flow of marine propellers within the same solver adopted to conduct the present simulations (Posa *et al.* 2019, 2022a; Posa & Broglia 2023; Posa 2023a).

The last term in the momentum equation (2.2),  $f_i$ , was adopted in the framework of an IB methodology to enforce the no-slip conditions on the surface of the bodies immersed within the flow. The IB method allows relaxing the requirement of the Eulerian grid, discretizing the computational domain, to conform the geometries of the bodies, typical of more conventional body-fitted techniques. This is especially problematic in case of complex, moving geometries. In contrast, IB methods allow using regular Eulerian grids, while the geometry of the bodies immersed within the flow is represented by Lagrangian grids, discretizing their surface and free to move across the cells of the Eulerian grid. The enforcement of the no-slip condition on the surface of the Lagrangian grids is achieved through the term  $f_i$  in (2.2). This is defined based on the position of the Eulerian points, relative to the Lagrangian grids of the immersed boundaries. The Eulerian points are separated in fluid, solid and interface points. The fluid points are those located outside the immersed boundaries and having no neighbouring solid points, which are located inside. The interface points are the Eulerian points outside the immersed boundaries, but having at least one neighbouring solid point. At the fluid points no condition is required and  $f_i = 0$ . At the solid points the velocity boundary condition to be enforced,  $\mathcal{U}_i$ , is the velocity of the body where those points are located, to mimic its rigid motion. At the interface points the condition  $\mathcal{U}_i$  is computed from a linear reconstruction of the solution along the direction normal to the surface of the Lagrangian grid representing the body. This reconstruction utilizes as boundary conditions the no-slip requirement on the surface of the body and the solution at the fluid points surrounding the particular interface point. Then, the forcing term  $f_i$  is computed as

$$f_i = \frac{\mathcal{U}_i - \tilde{u}_i}{\Delta t} - \mathcal{R}_i, \quad i = 1, 2, 3, \quad (2.5)$$

where  $\tilde{u}_i$  is the local solution of the flow at the particular solid or interface point,  $\Delta t$  is the step of the advancement in time of the numerical solution, while  $\mathcal{R}_i$  is the sum of the convective, viscous, SGS and pressure gradient terms of the momentum equation, which are discretized explicitly. The particular implementation of the IB method is discussed in more detail in the works by Balaras (2004) and Yang & Balaras (2006) and was already successfully adopted in a number of our earlier studies on the flow through marine propellers (Posa & Broglia 2022a,b; Posa 2022, 2023b).

The NSEs were discretized on a staggered cylindrical grid, using second-order central differences. The advancement in time utilized a fractional-step methodology (Van Kan 1986). The discretization in time of all convective, viscous and SGS terms of radial and axial derivatives adopted the explicit, three-step Runge–Kutta scheme. Due to the anisotropy of cylindrical grids at small radii, the discretization in time of all terms of azimuthal derivatives instead utilized an implicit scheme (Crank–Nicolson), to relax the stability requirements on the size of the step of the advancement in time of the numerical solution. The discretization of the continuity equation (2.1) results in a hepta-diagonal Poisson problem. For efficiency, this was reduced into a series of penta-diagonal problems by trigonometric transformations across the periodic azimuthal direction. Then, each of them was inverted by an efficient direct solver (Rossi & Toivanen 1999), rather than by costly iterative techniques. The overall NSEs solver was demonstrated to be second-order accurate in both space and time on canonical problems by Balaras (2004) and Yang & Balaras (2006) and was validated in several cases dealing with marine propellers in the framework of our earlier studies (Balaras *et al.* 2015; Posa *et al.* 2019; Posa & Broglia 2022a; Posa 2023a).

It is worth mentioning that in the following discussion only resolved quantities will be considered. Therefore, for convenience, the notation  $\tilde{\cdot}$  utilized in this section for filtered velocity and pressure will be omitted hereafter.

### 2.2. Reconstruction of the acoustic signature of the system

In this study the acoustic field was reconstructed by exploiting the acoustic analogy, which assumes that the acoustic phenomena have a negligible influence on the fluid dynamics. Therefore, it is legitimate to resolve the fluid dynamics without taking into account the hydroacoustics and then reconstructing the latter by using the database of realizations of the solution generated by the simulation of the former. The flow is treated as a collection of acoustic sources and the acoustic field is radiated in the far field by using the wave theory, assuming that the propagation of sound occurs in a homogeneous, unbounded medium. In particular, in the present work this result was achieved by considering the FWH equation in integral form (Ffowcs Williams & Hawkings 1969). The same methodology was already successfully adopted in our earlier studies on marine propellers, including also comparisons with physical measurements (Posa *et al.* 2022*b,c,d,e*):

$$\begin{aligned}
 4\pi \langle p \rangle(\mathbf{x}, t) = & \frac{\partial}{\partial t} \int_{\mathcal{S}} \left[ \frac{\rho^* v_n}{r|1 - M_r|} \right]_{\mathcal{T}} dS + \frac{1}{c} \frac{\partial}{\partial t} \int_{\mathcal{S}} \left[ \frac{p' \hat{n}_i \hat{r}_i}{r|1 - M_r|} \right]_{\mathcal{T}} dS \\
 & + \int_{\mathcal{S}} \left[ \frac{p' \hat{n}_i \hat{r}_i}{r^2|1 - M_r|} \right]_{\mathcal{T}} dS + \frac{1}{c^2} \frac{\partial^2}{\partial t^2} \int_{\mathcal{V}} \left[ \frac{T_{rr}}{r|1 - M_r|} \right]_{\mathcal{T}} dV \\
 & + \frac{1}{c} \frac{\partial}{\partial t} \int_{\mathcal{V}} \left[ \frac{3T_{rr} - T_{kk}}{r^2|1 - M_r|} \right]_{\mathcal{T}} dV + \int_{\mathcal{V}} \left[ \frac{3T_{rr} - T_{kk}}{r^3|1 - M_r|} \right]_{\mathcal{T}} dV, \quad i = 1, 2, 3.
 \end{aligned} \tag{2.6}$$

In (2.6),  $\langle p \rangle$  is the acoustic pressure, while  $\mathbf{x}$  is the position vector of the receiver. The scalar  $r$  is the magnitude of the vector  $\mathbf{r} = \mathbf{x} - \mathbf{y}$ , representing the position of the receiver, relative to the position  $\mathbf{y}$  of the acoustic source. Here  $M_r$  is the Mach number of the flow in the direction defined by the vector  $\mathbf{r}$ , while  $\hat{r}_i$  is the component in the direction  $i$  of the unit vector of  $\mathbf{r}$ . The quantity  $\rho^*$  is a reference density, assumed equal to the density,  $\rho$ , of the fluid,  $v_n$  is the velocity of the elemental surface  $dS$  in its normal direction,  $c$  is the speed of sound in the fluid,  $\hat{n}_i$  is the component in the direction  $i$  of the unit vector normal to the elemental surface  $dS$  and  $p'$  is the fluctuation in time of the hydrodynamic pressure on  $dS$ . The scalar  $T_{rr}$  is given by  $T_{rr} = T_{ij} \hat{r}_i \hat{r}_j$ , where  $T_{ij}$  is the  $ij$  element of the Lighthill tensor, defined as

$$T_{ij} = \rho u_i u_j + [(p - p^*) - c^2(\rho - \rho^*)] \delta_{ij} - \sigma_{ij}. \tag{2.7}$$

In (2.7),  $p^*$  is a reference pressure, assumed in this case equal to its free-stream value,  $p_\infty$ , while  $\sigma_{ij}$  is the  $ij$  element of the viscous stress tensor. The scalar  $T_{kk}$  in (2.6) is the trace of the Lighthill tensor.

The time  $\mathcal{T}$  is given by

$$\mathcal{T} = t - r/c = t - \frac{|\mathbf{x}(t) - \mathbf{y}(\mathcal{T})|}{c}, \tag{2.8}$$

where  $\mathcal{T}$  is the emission time, that is, the time when the sound waves start from the source of position  $\mathbf{y}$  to arrive at the receiver of position  $\mathbf{x}$  at the instant in time  $t$ , while  $r/c$  represents the time delay, that is, the time interval required for the propagation of the acoustic waves from the source at position  $\mathbf{y}$  to the receiver at position  $\mathbf{x}$ . It should be

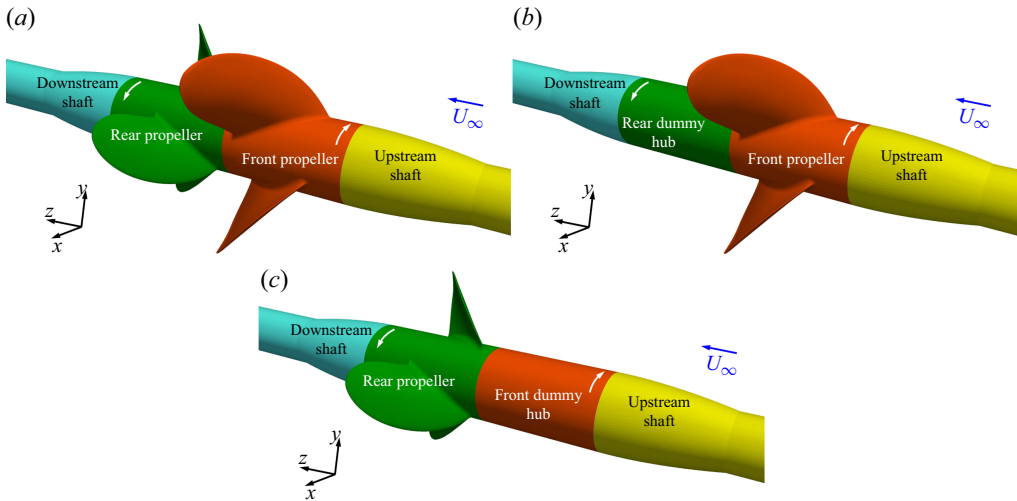


Figure 1. Geometries of the cases (a) CRP, (b) FRONT and (c) REAR.

noted that, for the typical Mach numbers relevant to marine propellers, the time delay is very small and can be neglected, as discussed in detail by Cianferra *et al.* (2019b). In particular, Cianferra, Armenio & Ianniello (2018, 2019a) introduced the criterion of the maximum frequency parameter, MFP, defined as

$$\text{MFP} = \frac{1}{\Delta_{del} f_{max}}, \quad (2.9)$$

where  $\Delta_{del} = [\max(|\mathbf{x} - \mathbf{y}|) - \min(|\mathbf{x} - \mathbf{y}|)]/c$ , while  $f_{max}$  is the maximum frequency at which the acoustic phenomena are investigated. If  $\text{MFP} < 1$  the time delay needs to be taken into account, otherwise it can be neglected. It was verified for the present case that  $\text{MFP} \approx 1.74$ , based on the highest considered frequency, corresponding to  $f = 30f_b$ , where  $f_b$  is the blade frequency. Therefore, the time delay can be neglected. This allows a substantial simplification in the computation of the integrals on the right-hand side of (2.6). Therefore, also in this work we assumed that  $\mathcal{T} \approx t$ .

In this study we adopted the direct approach of the FWH acoustic analogy, in contrast with the more typical permeable formulation by Di Francescantonio (1997). The former avoids the issue of the spurious noise resulting from the integration over a permeable surface encompassing the overall system: in the direct formulation the surface integrals of (2.6) are computed directly on the surface of the bodies immersed within the flow, while the volume integrals are computed across a volume encompassing all important acoustic sources in the wake. This approach allows us to separate the different components of the acoustic signature of the propulsion system, as discussed in detail in § 6. In particular, the following analysis of the acoustic field in § 6 will compare the contributions from the linear and nonlinear (quadrupole) components of the acoustic signature, associated with the surface and volume integrals on the right-hand side of (2.6), respectively. In this study the surfaces of integration  $\mathcal{S}$  were selected on the Lagrangian grids representing the immersed boundaries. The volume of integration  $\mathcal{V}$  was chosen as a cylindrical volume large enough to include all important acoustic sources. More details dealing with  $\mathcal{S}$  and  $\mathcal{V}$  are reported below in § 5.

### 3. Flow problem

A system of contra-rotating propellers was simulated by LES. As illustrated in figure 1(a), it consists of front and rear three-bladed, fixed-pitch propellers rotating with opposite angular speeds and ingesting a uniform flow, whose free-stream velocity  $U_\infty$  was assumed as the reference velocity scale. The front propeller is characterized by a larger diameter,  $D$ , adopted in this study to scale all lengths. The rear propeller has a smaller diameter  $d \approx 0.91D$ . To mimic the same conditions considered in the reference experiments by Capone & Alves Pereira (2020), Capone *et al.* (2021) and Alves Pereira *et al.* (2021), upstream and downstream stationary shafts were also included in the set-up of the LES computations. In the following discussion, the system of the two propellers working together will be denoted as CRP.

For comparison purposes and in order to isolate the effect of the interaction between the two propellers on the flow physics and their acoustic signature, the front and rear propellers were also simulated working alone. These two cases will be denoted as FRONT and REAR, respectively. They are represented in the panels of figures 1(b) and 1(c). In those cases the missing rear and front propellers, respectively, were replaced by dummy hubs, rotating at the same angular speed of the propellers they were replacing. This is the same strategy adopted in the reference experiments.

All cases were simulated at an advance coefficient

$$J = \frac{V}{nD} = 0.7, \quad (3.1)$$

where  $V$  is the advance velocity, equal to the free-stream velocity,  $U_\infty$ , while  $n$  is the rotational frequency of the propellers. It is worth mentioning that this is a highly loaded condition, since the design value of the advance coefficient of the CRP system is equal to about 1.4. This working condition was selected for exploring a case with stronger wake structures and acoustic signature, compared with design.

The Reynolds number, based on the front propeller, is equal to

$$Re_p = \frac{c_{70\%R} \sqrt{(2\pi n 0.7R)^2 + V^2}}{\nu} \approx 250\,000, \quad (3.2)$$

where  $c_{70\%R}$  is the chord of the blades of the front propeller at 70 % of its radial extent,  $R$ , while  $\sqrt{(2\pi n 0.7R)^2 + V^2}$  is the magnitude of the relative velocity of the flow at the same radial location.

In the present work all systems were simulated at the same advance coefficient, since the study is mainly aimed at assessing the effect of the interaction between tip vortices on both the fluid dynamics, discussed in Posa *et al.* (2024), and the nonlinear component of the acoustic signature, which is the main subject of the present study. In these conditions tip vortices of similar intensities are generated by the front and rear propellers in the contra-rotating and isolated configurations. The following discussion will show indeed that each propeller working in the contra-rotating system produces similar levels of thrust as the same propellers working alone. In spite of this, we demonstrate an increased importance of the quadrupole components of sound in the overall acoustic field, in comparison with the linear ones, as a result of the shear developed between the wakes of the front and rear propellers operating together and, in particular, between the tip vortices they shed. However, it is important to acknowledge that this choice affects the comparison of the intensity of the acoustic fields across systems, since they are not producing the same levels of thrust. The following discussion in § 6 will report indeed that the overall CRP system generates roughly twice the thrust produced by the two propellers of the system

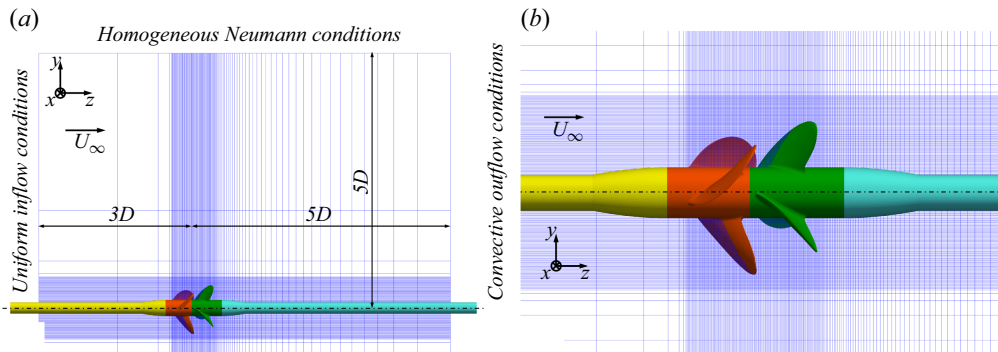


Figure 2. Meridian slice of the fine grid: (a) global view and (b) detail in the vicinity of the propellers. For visibility, 1 of every 256 and 64 points in panels (a) and (b), respectively.

operating alone. For the achievement of similar levels of thrust, it would be necessary to simulate the isolated propellers at lower advance coefficients, adjusting their values to get the same overall thrust produced by the CRP system. Meanwhile, in that case the tip vortices shed by the isolated propellers would be significantly more intense than those shed by the propellers of the CRP system. Therefore, the comparisons of the present study are aimed at demonstrating the increased importance of the nonlinear component of sound in the overall acoustic signature of contra-rotating propellers, even in the presence of tip vortices of similar intensity as those populating the wake of isolated propellers, rather than assessing whether contra-rotating propellers are a more or less noisy alternative to the isolated ones.

#### 4. Set-up of the LES computations

The LES computations were conducted within a cylindrical domain with a radial extent equivalent to  $5D$ . Its inflow and outflow sections were located respectively  $3D$  and  $5D$  upstream and downstream of the plane of interface between the hubs of the front and rear propellers, where the origin of the streamwise coordinates was placed. Since the reference experiments by Capone & Alves Pereira (2020), Capone *et al.* (2021) and Alves Pereira *et al.* (2021) were conducted in open water, at the inflow section a condition of uniform streamwise velocity,  $U_\infty$ , was enforced, while the radial and azimuthal velocities were equal to 0. At the outflow section, convective conditions were utilized for all three velocity components, using the free-stream velocity,  $U_\infty$ , as the convective velocity. At the lateral, cylindrical boundary of the domain, homogeneous Neumann conditions were imposed to mimic the free stream. Across all boundaries of the cylindrical domain homogeneous Neumann conditions were also utilized for both pressure and eddy viscosity. The no-slip requirement on the surface of the bodies immersed within the flow was enforced by using the IB technique discussed in § 2.

Thanks to the IB methodology, the computational domain was discretized by using a regular, cylindrical grid, where the NSEs were resolved. This grid consisted of  $722 \times 3586 \times 1794 \approx 4.6$  billion points in the radial, azimuthal and axial directions, respectively, for all CRP, FRONT and REAR cases we simulated. A meridian slice of the grid is shown in figure 2, where only a small sample of points is illustrated, for visibility of the grid lines. This grid adopts stretching in the radial and axial directions, with the purpose of clustering points in the regions of the domain populated by the propellers and their wake. The radial grid is uniform in the region of the propellers, with a spacing  $\Delta r = 7.5 \times 10^{-4} D$

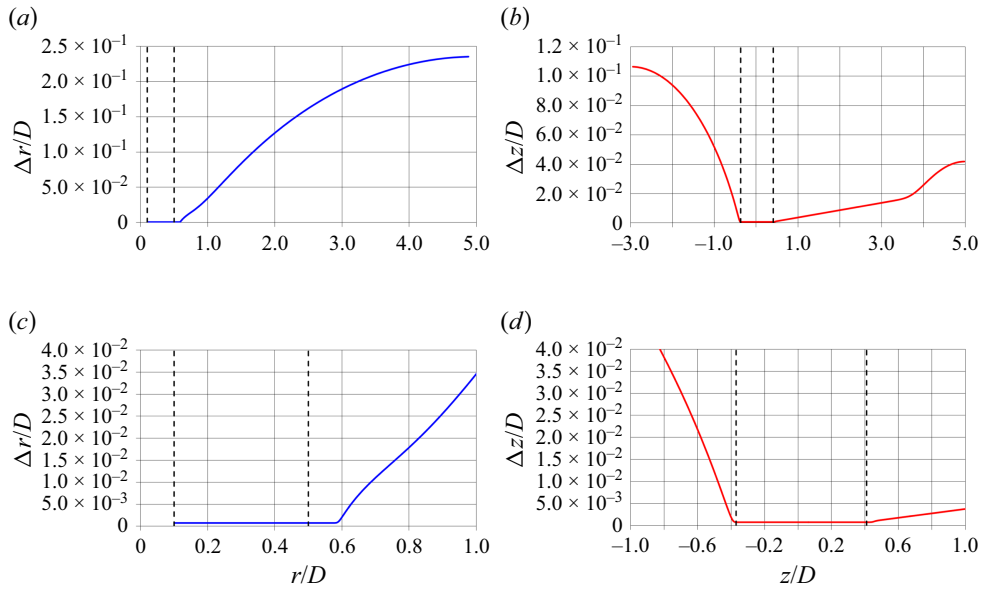


Figure 3. Radial and axial distributions of the grid spacing: across the whole computational domain in panels (a) and (b) and in the vicinity of the propellers in panels (c) and (d). Vertical dashed lines for the radial and axial boundaries of the region of the blades of the front and rear propellers.

up to about  $r/D = 0.6$ , while it is stretched up to the lateral boundary of the domain. The axial grid is uniform between  $-0.35 < z/D < 0.45$ , in the region encompassing the two propellers, with a resolution  $\Delta z = 7.5 \times 10^{-4} D$ , and is stretched both upstream and downstream. However, its downstream stretching is slower than the upstream one, in order to resolve properly the wake features of the system up to  $z/D = 3.5$ . Further downstream the grid coarsening accelerates, up to the outflow boundary of the domain. More details on the distribution of the radial and axial grid spacings are reported in figure 3. In the azimuthal direction the angular spacing of the grid is uniform. The choice of a cylindrical grid is actually convenient, since a uniform angular spacing results in a finer linear spacing towards inner radii, where the propellers and their wakes are located. Therefore, the cylindrical topology allows saving grid points, compared with a Cartesian grid. The linear, azimuthal spacing of the grid at the reference location of 70 %R is equivalent to  $0.7R\Delta\vartheta = 6.1 \times 10^{-4} D$ , resulting in an almost isotropic grid across the three directions in space. This design of the Eulerian grid was based on our earlier experience in Posa *et al.* (2019, 2022a), where similar or even coarser levels of resolution were able to capture with accuracy the wake flow, as demonstrated by the comparison with the Particle Imaging Velocimetry (PIV) experiments by Felli & Falchi (2018). We verified that the resolution of this grid in the near wall region of the propellers is equivalent to about 5 wall-units. This grid will be denoted hereafter as fine grid. Unless otherwise stated, all results reported below will refer to the data produced using this particular resolution. In addition, a grid refinement study was carried out on the CRP case, considering two additional resolutions. They were generated by reducing the number of grid points across all directions in space by factors equal to about  $2^{1/3}$  and  $2^{2/3}$  and are denoted here as medium and coarse grids. They consist of  $572 \times 2818 \times 1410 \approx 2.3$  billion points and  $454 \times 2370 \times 1186 \approx 1.3$  billion points. They were useful to verify a good grid-independence of both fluid dynamic and acoustic results.

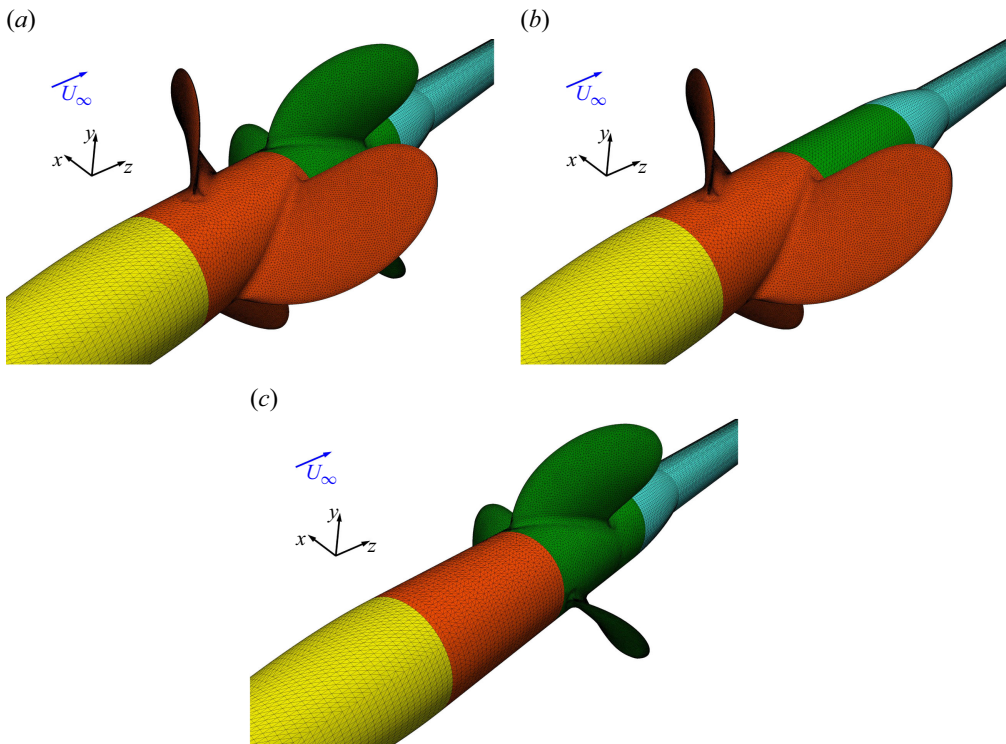


Figure 4. Lagrangian grids for the cases (a) CRP, (b) FRONT and (c) REAR.

Lagrangian grids were utilized to represent the surface of the bodies immersed within the flow. They consist of triangular elements and are free to move across the cells of the Eulerian grids discussed above, which discretize the computational domain. In the simulations of the CRP system the Lagrangian grids consist of about 32 000 (upstream shaft), 66 000 (front propeller), 69 000 (rear propeller) and 51 000 (downstream shaft) elements. As discussed in § 3, for the simulations of the FRONT and REAR cases the rear and front propellers were replaced by their respective dummy hubs, consisting of about 10 000 triangles each. A representation of the Lagrangian grids is provided in the three panels of figure 4 for the CRP, FRONT and REAR systems.

The resolution in time of all computations was very fine, since tied to the resolution in space through the stability requirements of the Runge–Kutta scheme, which was adopted for the explicit discretization of the convective terms of the momentum equation in the radial and axial directions. As discussed in § 2, the exploitation of an implicit scheme allowed relaxing the otherwise prohibitive stability requirements in the azimuthal direction of the cylindrical grid. All simulations were carried out at a constant Courant–Friedrichs–Lewy number equal to 1.0. For the computations conducted on the fine grid, the resolution in time resulted in more than 7000 time steps per rotation of the propellers in all CRP, FRONT and REAR cases. The resolution in time for the computations of the CRP case on the medium and coarse grids was lower, but still very fine: more than 5000 time steps were required on the coarse grid for a full revolution of both propellers.

For all cases, the simulations were advanced across 20 rotations of the propellers, with the purpose of achieving statistically steady conditions in the wake. Then, 20 additional rotations were simulated to compute phase-averaged statistics of the flow on the fly. In

the following discussion, results for the phase-averaged turbulent kinetic energy,  $\widehat{k}$ , are reported. It is defined as

$$\widehat{k} = \frac{1}{2}(\widehat{u'^2} + \widehat{v'^2} + \widehat{w'^2}), \quad (4.1)$$

where  $\widehat{\cdot}$  is the notation adopted to indicate phase-averaged statistics,  $u, v, w$  are the radial, azimuthal and axial velocity components,  $u', v', w'$  their fluctuations in time and  $\widehat{u'}, \widehat{v'}, \widehat{w'}$  their root mean squares in time. Results for the turbulent shear stress  $\widehat{u'w'}$ , dealing with the fluctuations in time of the radial and axial velocity components, are also provided below. In addition, time-averaged statistics of the turbulent stresses are reported, for comparison between the relative magnitude of the resolved and modelled components. Time-averaged quantities are indicated as  $\bar{\cdot}$ .

Time-averaged statistics of the Lamb vector,  $L$ , are discussed as well, both as time average of its magnitude,  $\bar{L}$ , and as root mean squares in time of its magnitude,  $\overline{L'}$ . The Lamb vector is the cross-product of the vorticity and velocity vectors. It is a quantity relevant to the acoustic emission from the coherent structures populating the wake, as demonstrated by the Powell acoustic analogy (Powell 1964), where its time history appears as a source term. More details on the subject are reported in the work of Felli, Falchi & Dubbioso (2015). In addition, also results for the scalar  $\partial^2 T_{ij} / \partial x_i \partial x_j$  will be provided, following the earlier work by Cianferra *et al.* (2019b). It is worth recalling that the Lighthill tensor is the source term of the quadrupole component of the acoustic signature in the advective, differential form of the FWH equation (for more details, see Cianferra *et al.* 2018, 2019a).

All computations were carried out in a high performance computing environment, using a parallel, in-house developed Fortran solver. It exploits a domain decomposition strategy, splitting the overall domain in smaller cylindrical subdomains across the streamwise direction. They are allocated across cores of distributed-memory supercomputers. In particular, the computations of the present study were carried out on MeluXina CPU at LuxProvide (Luxembourg), thanks to a grant from EuroHPC Joint Undertaking. Communications across subdomains were handled by means of calls to message-passing interface libraries. For the simulations on the fine, medium and coarse grids, 1792, 1408 and 1184 cores were utilized, respectively, resulting in an overall cost of the computations of about 13 million CPU hours.

## 5. Set-up of the acoustic post-processing

The acoustic signature was reconstructed in post-processing from instantaneous realizations of the solution generated by the LES computations. They were saved on disk with a frequency equivalent to  $1^\circ$  of rotation of both front and rear propellers. As discussed in § 4, the resolution in time of our computations was 20 times finer, but the size of the data to be stored, tied to the resolution in space of the computational grids, did not allow for a higher sampling frequency.

The computation of the linear terms of the acoustic pressure, corresponding to the surface integrals of (2.6), was carried out on the Lagrangian grids representing the bodies immersed within the flow. In particular, the fluctuations of hydrodynamic pressure were interpolated from the Eulerian points on the triangles of the Lagrangian grids. For the computation of the quadrupole component of the acoustic signature, corresponding to the volume integrals of (2.6), we selected a control volume including all acoustic sources. This was a cylinder having a radial extent equivalent to  $0.9D$  and upstream/downstream boundaries located  $2.5D$  and  $4.5D$ , respectively, from the interface between the hubs of

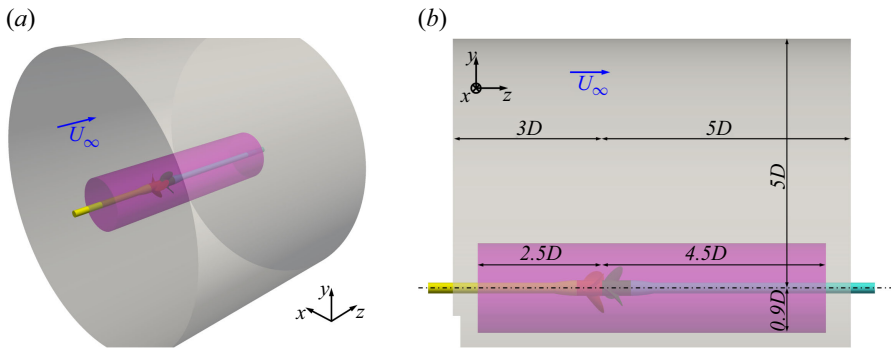


Figure 5. Control volume utilized for the reconstruction of the acoustic field shown in magenta. The grey cylinder represents the cylindrical domain of the LES computations. (a) Isometric and (b) lateral views.

the front and rear propellers (see figure 5). This control volume was selected to encompass the whole resolved wake of the propellers, which is a source of nonlinear sound. Note that the downstream boundary of the control volume was not placed exactly on the outflow boundary of the LES computations, at  $z/D = 5.0$ , because of the effect on the accuracy of the solution by the outflow boundary conditions and grid coarsening in the most downstream region of the computational domain.

A number of hydrophones equal to 5760 were utilized to reconstruct the acoustic near field, spanning eight radial locations ( $r/D = 1, 2, 4, 8, 16, 32, 64$  and  $128$ ) and 10 streamwise locations ( $z/D = -2.0, -1.0, -0.5, -0.1, 0.3, 0.5, 1.0, 2.0, 3.0$  and  $4.0$ ), with the purpose of reconstructing the radial and streamwise evolutions of sound. The distribution of the hydrophones along the radial direction took into account the decreasing gradients of the acoustic field while moving away from the source of sound. The range of streamwise locations considered was bounded by the size of the computational domain, limiting the extent of the wake we were able to simulate downstream of the propeller. Note also that the streamwise coordinates  $z/D = -0.1$  and  $z/D = 0.3$  are aligned with the planes of the front and rear propellers, respectively. With the purpose of increasing the size of the statistical sample, 72 hydrophones were distributed along the azimuthal direction at each of the radial and streamwise locations above, with a uniform spacing of  $5^\circ$ . The directivity of the nonlinear component of sound was also analysed considering additional hydrophones located on the planes of equations  $y/D = 0.0$  and  $z/D = 0, 0$ , which are respectively a meridian plane and a cross-stream plane. On those planes 72 hydrophones were placed at both distances from the origin of the reference frame equivalent to  $8D$  and  $128D$ , with the purpose of analysing the dependence of the acoustic pressure on the polar angle.

The time history of the acoustic pressure,  $\langle p \rangle$ , reconstructed from (2.6), was utilized to compute the SPLs in decibels (dB) as

$$\text{SPL} = 20 \log_{10} \left( \frac{A_{FFT}[\langle p \rangle]}{\langle p_0 \rangle} \right), \quad (5.1)$$

where  $A_{FFT}[\langle p \rangle]$  is the amplitude at each particular frequency of the fast Fourier transform (FFT) of the time history of the acoustic pressure, while  $\langle p_0 \rangle$  is a reference value for the acoustic pressure, taken in this study equal to  $1 \mu\text{Pa}$ , as typical for underwater radiated noise. It should be noted that in this study the values for the acoustic pressure will be dimensionalized based on the conditions considered in the experiments by Capone & Alves Pereira (2020), Capone *et al.* (2021) and Alves Pereira *et al.* (2021): a diameter of

	CRP (front)	CRP (rear)	FRONT	REAR
$\overline{K}_T$	0.392 (+2.44 %)	0.357 (+1.99 %)	0.388 (+0.95 %)	0.308 (+1.79 %)
$10\overline{K}_Q$	0.869 (−0.23 %)	0.886 (+1.15 %)	0.883 (−1.59 %)	0.743 (−2.54 %)
$\overline{\eta}$	50.2% (+2.68 %)	44.8% (+0.83 %)	48.9% (+2.58 %)	46.2% (+4.44 %)

Table 1. Global parameters of performance from the LES computations on the fine grid. The errors relative to the experiments are given in parentheses.

the front propeller equal to  $D = 0.219$  m, a free-stream velocity equal to  $U_\infty = 3.68$  m s<sup>−1</sup>, a density of water equal to  $\rho = 998.2$  kg m<sup>−3</sup> and a speed of sound in water equal to  $c = 1482$  m s<sup>−1</sup>. Results for the SPLs will be given below in narrow-band spectra as well as in the third-octave bands centred at six particular frequencies:  $f/f_b = 1/3, 1, 2, 5, 10, 30$ .

Due to the size of the data to be post-processed and the resulting memory requirements, this activity was performed on a distributed-memory cluster as well, by means of parallel, in-house developed Fortran codes. Again, the full problem was split in cylindrical subdomains across 1792, 1408 and 1184 cores respectively for the fine, medium and coarse grids.

## 6. Results

### 6.1. Performance of propulsion

The parameters of global performance of the CRP, FRONT and REAR systems were already reported in one of our earlier publications (Posa *et al.* 2024). However, for the sake of clarity, for validation against experimental measurements and to provide evidence of grid convergence, those results are also briefly recalled in the present study. Table 1 provides the time-averaged values from the LES simulations on the fine grid for the thrust coefficient,  $K_T$ , the torque coefficient,  $K_Q$ , and the propulsion efficiency,  $\eta$ , defined as

$$K_T = \frac{T}{\rho n^2 D^4}, \quad K_Q = \frac{Q}{\rho n^2 D^5}, \quad \eta = \frac{J K_T}{2\pi K_Q}, \quad (6.1)$$

where  $T$  and  $Q$  are the axial force and moment, respectively, acting between the propellers and the flow. In table 1 the percentages in parentheses represent the error of the LES computations, relative to the experiments conducted by Capone *et al.* (2021) and Alves Pereira *et al.* (2021), while the headers CRP (front) and CRP (rear) deal with the front and rear propellers working together within the CRP system, respectively.

Table 1 shows that the deviations of the present computations from the experiments are small, providing confidence on the accuracy of the LES results. The same data show that the efficiency of the front propeller is slightly improved when working within the CRP system, especially due to a small reduction of the moment acting on its blades, which is consistent with the experiments. Meanwhile, the rear propeller experiences a significant increase of both thrust and torque of more than 15 %, when working together with the front propeller, which is also in agreement with the measurements. In other words, the CRP system is able to generate a larger thrust, compared with the overall thrust produced by the isolated front and rear propellers.

As discussed above in § 4, LES computations were also conducted on the CRP system on two additional grids, indicated as medium and coarse grids. Tables 2 and 3 provide the results on those grids in terms of parameters of global performance, together with

	CRP (front)	CRP (rear)
$\overline{K}_T$	0.390 (+2.13 %) [−0.30 %]	0.355 (+1.43 %) [−0.56 %]
$10\overline{K}_Q$	0.871 (−0.05 %) [+0.18 %]	0.882 (+0.68 %) [−0.47 %]
$\overline{\eta}$	50.0% (+2.18 %) [−0.48 %]	44.8% (+0.74 %) [−0.09 %]

Table 2. Global parameters of performance from the LES computations on the medium grid. The errors relative to the experiments are given in round brackets. The errors relative to the LES results on the fine grid are given in square brackets.

	CRP (front)	CRP (rear)
$\overline{K}_T$	0.389 (+1.76 %) [−0.66 %]	0.351 (+0.37 %) [−1.59 %]
$10\overline{K}_Q$	0.874 (+0.30 %) [+0.54 %]	0.882 (+0.63 %) [−0.52 %]
$\overline{\eta}$	49.6% (+1.46 %) [−1.19 %]	44.3% (−0.26 %) [−1.08 %]

Table 3. Global parameters of performance from the LES computations on the coarse grid. The errors relative to the experiments are given in round brackets. The errors relative to the LES results on the fine grid are given in square brackets.

their relative deviations from the experiments and from the LES results on the fine grid, indicated respectively in round and square brackets. The data in tables 2 and 3 demonstrate: (i) the close agreement with the measurements even on coarser grids, and (ii) the small grid dependence in the range of resolutions we are considering in the present study.

## 6.2. Wake flow

The main features of the wake flow are illustrated in this section, to demonstrate the increased complexity of its topology, due to the interaction between the tip vortices shed by the two propellers working together, in comparison with each of them working in isolation. This discussion will explain the stronger contribution of the quadrupole component to the overall sound radiated from the contra-rotating propellers, if compared with the isolated propellers, demonstrated by the following analysis of the acoustic signatures of the CRP, FRONT and REAR systems.

### 6.2.1. Coherent structures in the wake

Instantaneous realizations of the solution are shown in figure 6, where isosurfaces of the pressure coefficient, coloured by vorticity magnitude, are adopted to isolate the tip vortices, which are locations of pressure minima. The pressure coefficient is defined as  $c_p = (p - p_\infty)/(0.5\rho U_\infty^2)$ . The cases of the isolated front and rear propellers in figures 6(b) and 6(c) display the typical helical tip vortices shed by marine propellers (Kerwin 1986; Stella *et al.* 2000; Felli, Camussi & Di Felice 2011). This topology experiences a dramatic change downstream of the CRP system. In agreement with the visualizations from the experimental work by Capone & Alves Pereira (2020), isolated vortex rings are generated, each of them consisting of six helical arms, coming alternatively from the tip vortices shed by the front and rear propellers and linked by U-shaped vortex lobes. The shear between the U-shaped vortex lobes of consecutive vortex rings produces their radial shift towards outer and inner coordinates. The three upstream

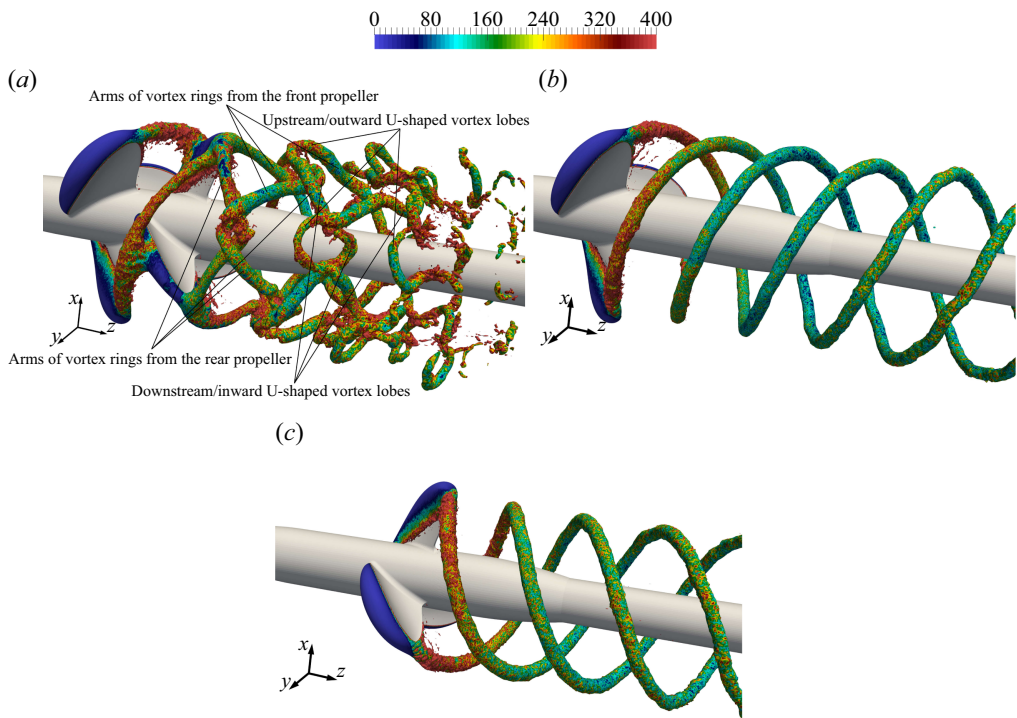


Figure 6. Instantaneous isosurfaces of pressure coefficient ( $c_p = -1.5$ ), coloured by vorticity magnitude, scaled by  $U_\infty/D$ . Comparison across cases (a) CRP, (b) FRONT and (c) REAR.

vortex lobes of each vortex ring move outwards, while the three downstream vortex lobes move inwards. This is the same wake dynamics observed in the experiments by Capone & Alves Pereira (2020), Capone *et al.* (2021) and Alves Pereira *et al.* (2021). This is shown in figure 7, where the tip vortices were visualized by inducing cavitation at their core by decreasing the pressure levels within the experimental facility. These results provide evidence of the accuracy of the simulations in reproducing this complex flow physics.

Additional comparisons with the experiments are reported in figure 8, where panel (a) deals with the phase-averaged azimuthal component of the vorticity vector from PIV measurements in the near wake, just downstream of the rear propeller. A similar visualization from the LES computations is given in figure 8(b), where the area encompassed by the dashed line indicates the window of the PIV experiments. The signature of three vortices is well distinguishable in both experimental and computational results. They are also outlined in panels (c) and (d) of figure 8. In particular, the phase-averaged isosurfaces of the second invariant  $Q$  of the velocity gradient tensor (Jeong & Hussain 1995) reveal that they are the signatures of the tip vortices coming from the front (A and C) and rear (B) propellers, respectively.

More details are provided in figure 9, where radial profiles across the core of the three tip vortices A, B and C were extracted from the contours of figure 8(a,b). Overall, the agreement between LES and PIV is satisfactory. The PIV results display smaller maxima of vorticity, due to the coarser resolution of the experimental grid ( $1.5 \times 10^{-2}D$ ), if compared with the computational one ( $7.5 \times 10^{-4}D$ ), as shown by the blunted shape of the peak of the experimental profiles. The coarser grid of the PIV measurement and the averaging nature of the PIV velocity estimation through cross-correlation tend to diffuse

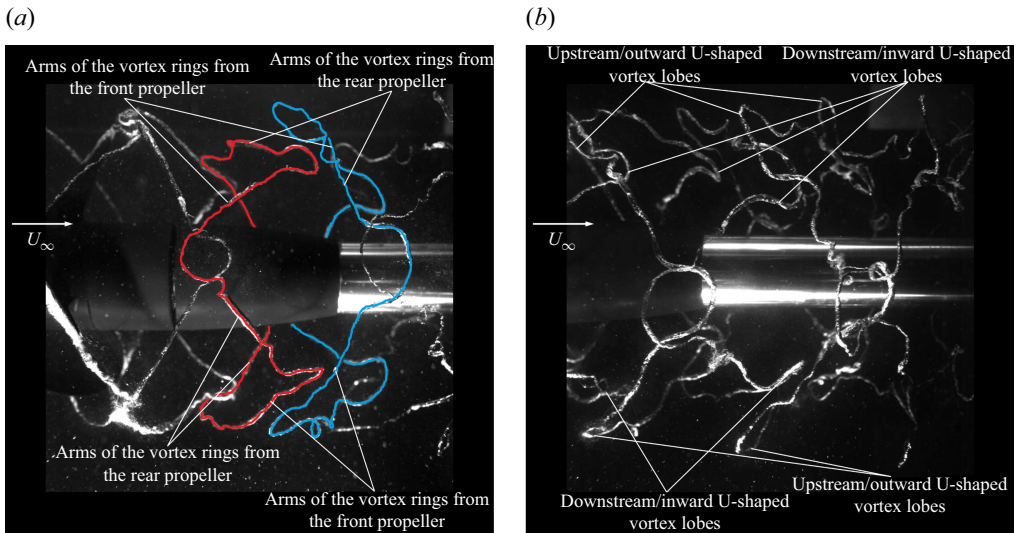


Figure 7. Instantaneous visualizations from experiments: (a) identification of two isolated vortex rings and their helical arms from the tip vortices of the front and rear propellers, respectively; (b) identification of the outward and inward U-shaped vortex lobes.

the vorticity peaks, especially when in the presence of strong and concentrated velocity gradients such as those found around vortex cores.

Figure 10 shows radial profiles of time-averaged streamwise velocity in the wake of the CRP system from both experiments and computations, extracted from the contours in panels (a) and (b). Note that in the experimental results of figure 10(a) some memory of the trailing wake from the propeller blades is still visible, due to the smaller number of angular positions considered for the computation of the time-averaged statistics, in comparison with the results from LES. Time-averaged statistics from experiments were computed from instantaneous fields with an angular resolution of  $1^\circ$  for the front propeller and  $40^\circ$  for the rear propeller, while the time resolution of LES was equivalent to a rotation of about  $0.05^\circ$  for both propellers. The profiles in figure 10(c–f) show that the acceleration of the flow in the wake of the propellers is very similar between PIV and LES, which is consistent with the agreement found between experiments and computations on the global performance and, in particular, on the thrust generated by the two propellers working together.

For better clarity, the comparison across CRP, FRONT and REAR cases is also illustrated by means of phase-averaged isosurfaces of  $Q$  in figure 11. It is evident that the interaction between the tip vortices from the front and rear propellers has the effect of accelerating the breakup of their coherence. Vorticity, colouring the isosurfaces of  $Q$ , is reported to increase in the CRP case, compared with both FRONT and REAR cases, in particular in the near-wake region, which is characterized by intense interactions between the tip vortices shed by the front and rear propellers. Turbulent fluctuations are also significantly reinforced, promoting higher levels of acoustic emission. This is demonstrated in figure 12, where isosurfaces of the phase-averaged turbulent kinetic energy are shown, coloured by contours of the turbulent shear stress  $\overline{u'w'}$ . Besides the area of large turbulence shed from the blades of both propellers, large values are achieved in the core of the tip vortices. However, they affect a wider region in the CRP case, compared with FRONT and REAR cases. In particular, the areas of shear between consecutive vortex

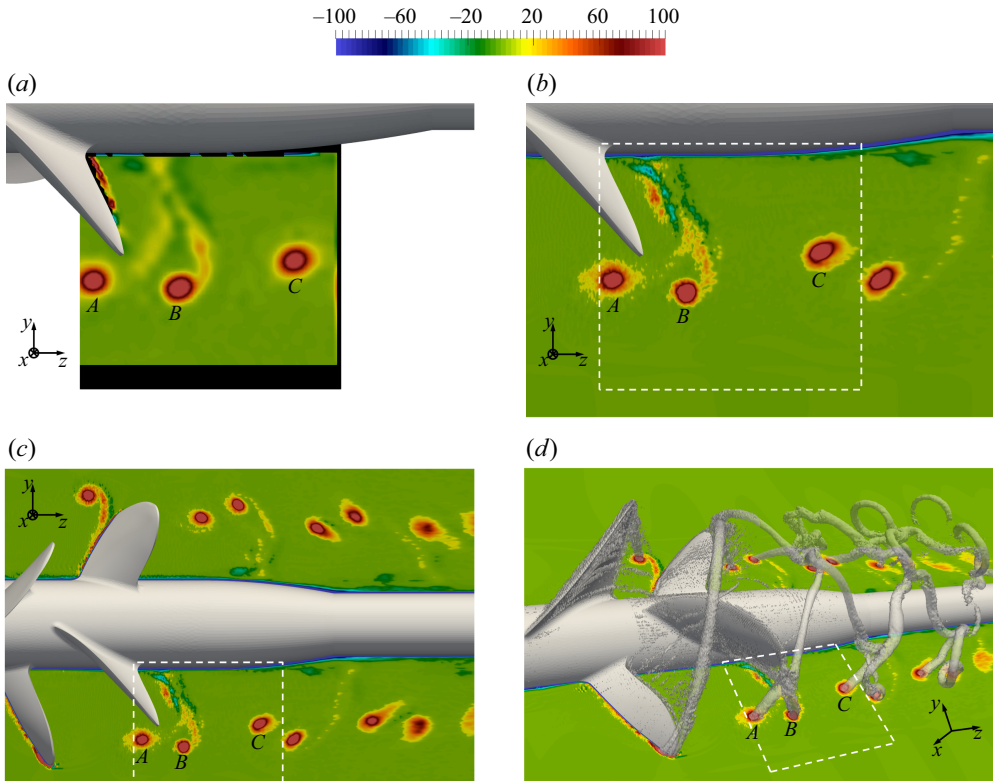


Figure 8. Contours of phase-averaged azimuthal vorticity, scaled by  $U_\infty/D$ , from PIV and LES in panels (a) and (b), respectively. Contours from LES computations in a wider domain in panel (c), together with phase-averaged isosurfaces of the second invariant of the velocity gradient tensor ( $Q$ -criterion by Jeong & Hussain 1995,  $\hat{Q}D^2/U_\infty^2 = 2000$ ) in panel (d). Dashed lines in panels (b), (c) and (d) represent the window of the PIV experiments.

rings downstream of the CRP system are those experiencing the highest turbulence, which grows downstream as the instability of the wake system develops. The flow physics is substantially different in the wake of the isolated propellers. Turbulence at the core of the tip vortices is initially below the threshold limit of  $k/U_\infty^2 = 0.15$  adopted for the isosurfaces in figure 12. Then, their growing instability leads to higher levels, making the signature of the tip vortices visible at downstream coordinates, as shown in the panels (b) and (c) of figure 12. However, if compared with the CRP case, they still affect a much smaller region, limited to the core of the tip vortices. In contrast, downstream of the CRP system they extend not only to the helical branches of the vortex rings originating from the tip vortices shed by the front and rear propellers, but also to the U-shaped inward and outward vortex lobes resulting from their interaction.

A satisfactory grid independence was also verified for the wake flow. The three panels of figure 13 show phase-averaged isosurfaces, based on the  $Q$ -criterion and coloured with vorticity magnitude, from the solutions of the CRP case on the fine, medium and coarse grids, respectively. The agreement of the results is very close, up to the breakup of the coherence of the isolated vortex rings originating from the interaction of the tip vortices shed by the front and rear propellers, respectively. This comparison is extended to the second-order statistics in figure 14, where isosurfaces of phase-averaged turbulent kinetic

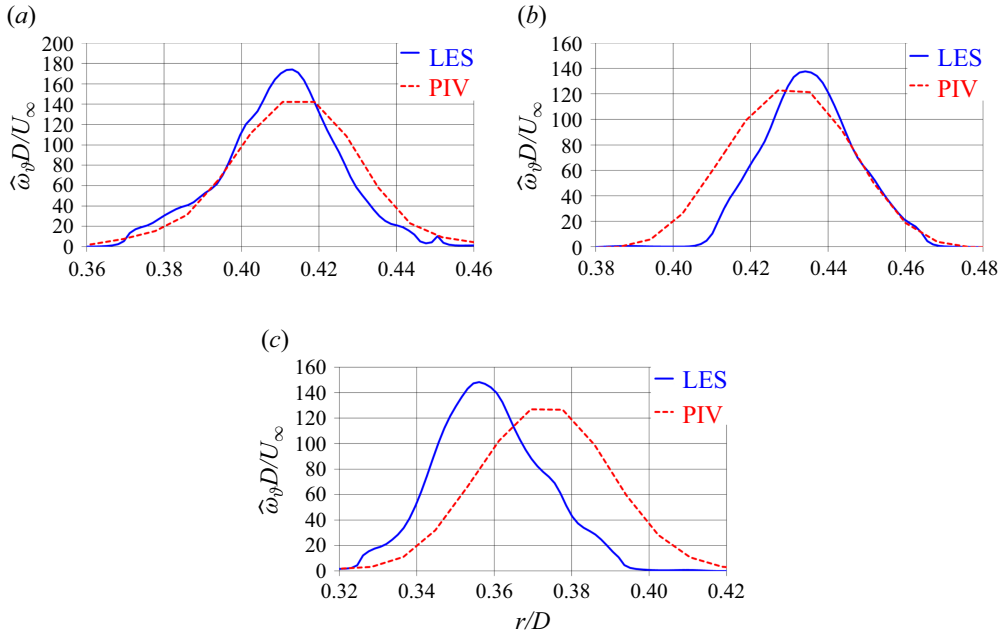


Figure 9. Radial profiles of phase-averaged azimuthal vorticity across the vortices *A*, *B* and *C* of figure 8: (a)  $z/D = 0.350$ , (b)  $z/D = 0.515$ , (c)  $z/D = 0.760$ . Comparison between LES and PIV.

energy are shown, coloured by contours of the turbulent shear stress  $\widehat{u'w'}$ . Although this comparison across resolutions is more challenging than that of figure 13, also the three panels of figure 14 show a good agreement. The same flow features are observed with similar levels of turbulent stresses, demonstrating that the dynamics of the near wake is accurately resolved, at least up to  $z/D = 3.5$ , where grid coarsening in the streamwise direction is accelerated up to the outflow boundary of the domain. These results provide further evidence of the adequacy of the resolution of the fine grid in capturing the physics of the near wake downstream of the contra-rotating propellers, which is the source of the quadrupole component of the acoustic signature of the system.

Additional evidence of the ability of the simulations at resolving the most energetic scales is provided in the wake of the CRP system in figure 15, where the deviatoric parts of the resolved and modelled Reynolds stresses are shown in the left and right panels, respectively. Note that we cannot compute explicitly the isotropic part of the modelled stresses. Different colour scales are adopted in the left and right panels of figure 15, due to the huge difference between resolved and modelled stresses. The latter are more than two orders of magnitude lower than the former. For the resolved stresses, figure 15 highlights the fact that the near wake is dominated by the components (a)  $rr$ , (c)  $\vartheta\vartheta$ , (e)  $zz$  and (i)  $rz$ , achieving their largest values in the region of mutual inductance between the tip vortices shed by the front and rear propellers of the contra-rotating system. The modelled stresses are by far dominated by the  $rz$  component, shown in figure 15(j). However, this is more than two orders of magnitude lower than the corresponding component of the tensor of the resolved stresses in figure 15(i). It is definitely evident that most turbulent stresses are resolved rather than modelled, demonstrating the adequacy of the computational grid. The results of the simulations of the isolated front and rear propellers agree with this conclusion, as shown in figures 16 and 17. As expected, results are similar between FRONT

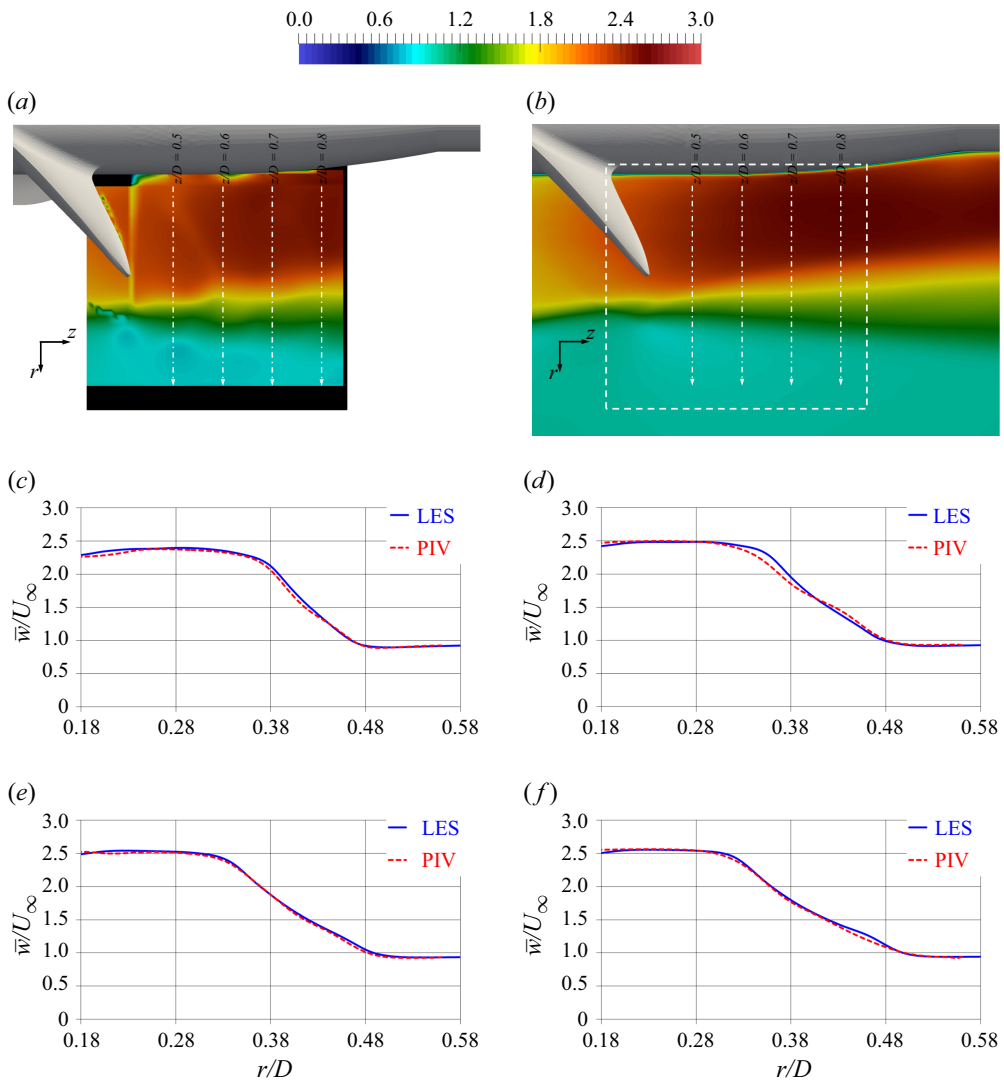


Figure 10. Radial profiles of time-averaged streamwise velocity in the wake of the CRP system, extracted from the contours of (a) the PIV experiments and (b) the LES computations: (c)  $z/D = 0.5$ , (d)  $z/D = 0.6$ , (e)  $z/D = 0.7$ , (f)  $z/D = 0.8$ . The dashed line in panel (b) represents the window of the PIV experiments. Dot-dashed arrows in panels (a) and (b) show the streamwise locations relative to the radial profiles in panels (c-f).

and REAR cases, although their (g)  $r\vartheta$  and (k)  $\vartheta z$  stresses have opposite orientations, since the two propellers rotate in opposite directions, affecting also the rotation of the tip vortices they shed. The deviatoric part of the resolved turbulent stresses is again dominated by the components (a)  $rr$ , (c)  $\vartheta\vartheta$ , (e)  $zz$ , while in these cases the near wake is characterized by higher levels of the (k)  $\vartheta z$  stress than the (i)  $rz$  one as downstream of the CRP system. The maxima in figures 16 and 17 are less diffused, compared with those in figure 15, since the tip vortices shed by the isolated propellers remain more stable further downstream. In figures 16 and 17 the highest modelled stresses are the components (h)  $r\vartheta$  and (j)  $rz$  across the trajectory of the tip vortices, but they are again more than two orders of magnitude smaller than their resolved counterparts.

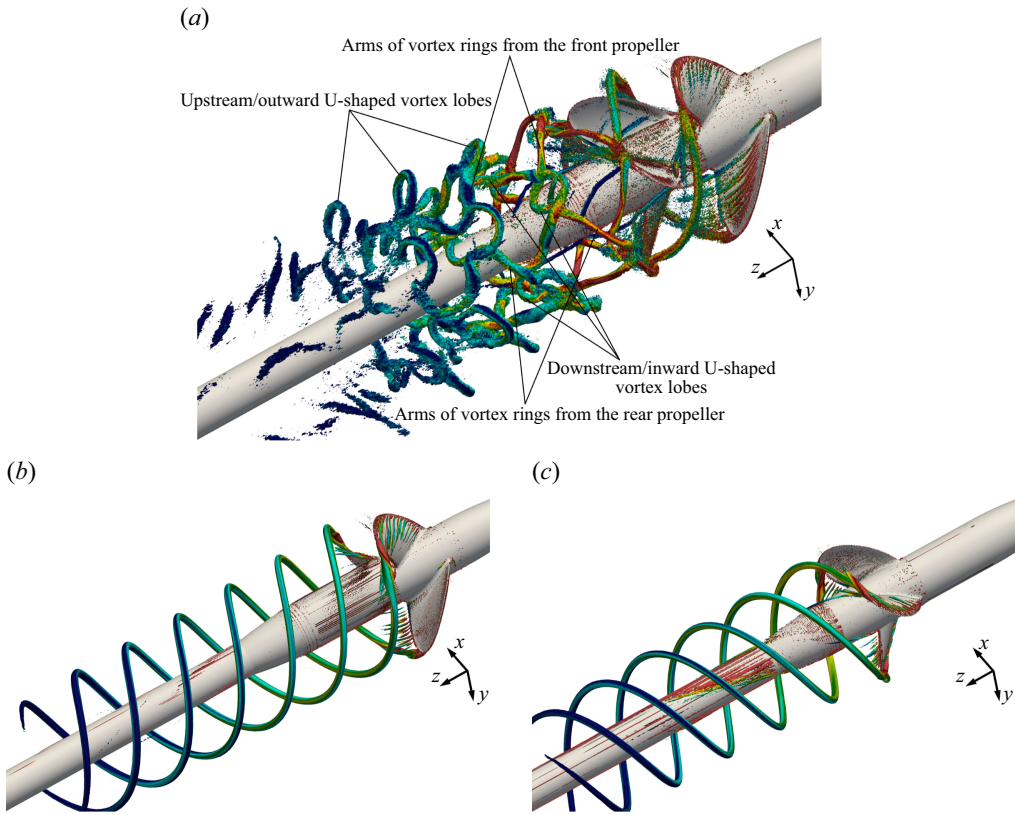
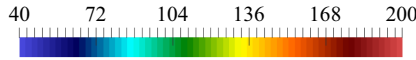


Figure 11. Isosurfaces of phase-averaged second invariant of the velocity gradient tensor ( $Q$ -criterion by Jeong & Hussain 1995,  $\widehat{Q}D^2/U_\infty^2 = 800$ ), coloured by vorticity magnitude, scaled by  $U_\infty/D$ . Comparison across cases (a) CRP, (b) FRONT and (c) REAR.

### 6.2.2. Statistics of the Lamb vector and Lighthill tensor

Figures 18 and 19 show a meridian slice with contours of  $\bar{L}$  and  $\partial^2 \bar{T}_{ij} / \partial x_i \partial x_j$ , respectively, for the three simulated propulsion systems. These quantities are tied to the nonlinear component of sound. The results in figures 18 and 19 highlight the major, dominant role of the tip vortices in the quadrupole component of the acoustic signature for all cases. It is also very clear the dramatic change in the average wake topology, due to the interaction between the tip vortices shed by the two contra-rotating propellers, having therefore an impact on the radiated sound. For the CRP system, large values of both quantities are found in an extended region in the near wake, where a faster diffusion takes place, as a result of the faster instability of the wake system, in comparison with the cases of the two propellers working alone. In these cases, two sharper maxima are observed at the outer boundary of the wake, which are the signatures of their tip vortices. In contrast, in the wake of the CRP system these maxima undergo a deflection towards both inner and outer radial coordinates. They are the signatures of the U-shaped vortex lobes produced by the shear between consecutive vortex rings. Overall, the wake of the CRP system experiences an expansion, in contrast with those of the two isolated front and rear propellers.

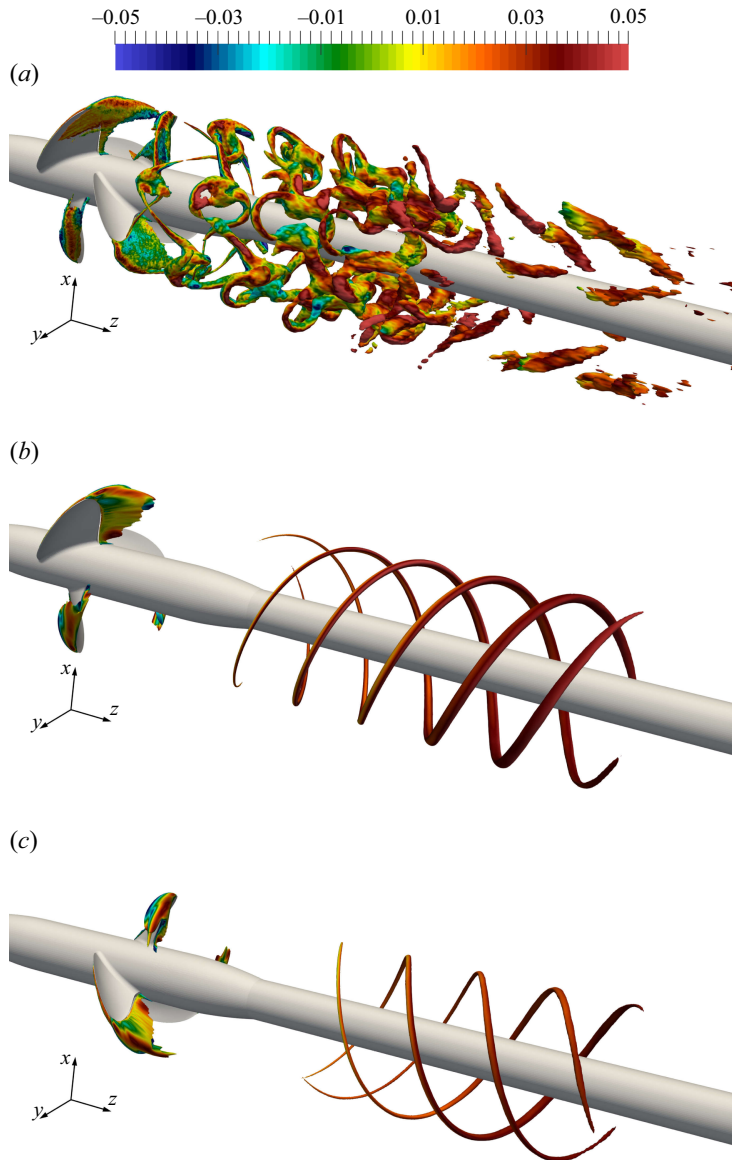


Figure 12. Isosurfaces of phase-averaged turbulent kinetic energy ( $\widehat{k}/U_\infty^2 = 0.15$ ), coloured by the turbulent shear stress  $\widehat{u'w'}$ , scaled by  $U_\infty^2$ . Comparison across cases (a) CRP, (b) FRONT and (c) REAR.

The dramatic change of the flow physics in the wake becomes even more obvious when the root mean squares of the fluctuations in time,  $\overline{L'}$ , are considered (figure 20). The achievement of substantially higher values downstream of the CRP system, in comparison with the FRONT and REAR ones, is consistent with the higher levels of the nonlinear component of sound demonstrated by the following discussion of the acoustic signature. Even more than in figure 18, the contours of figure 20 show higher and broader maxima spanning the whole radial extent of the CRP wake, while much lower and narrower peaks are achieved downstream of the isolated propellers at the radial coordinates of their tip

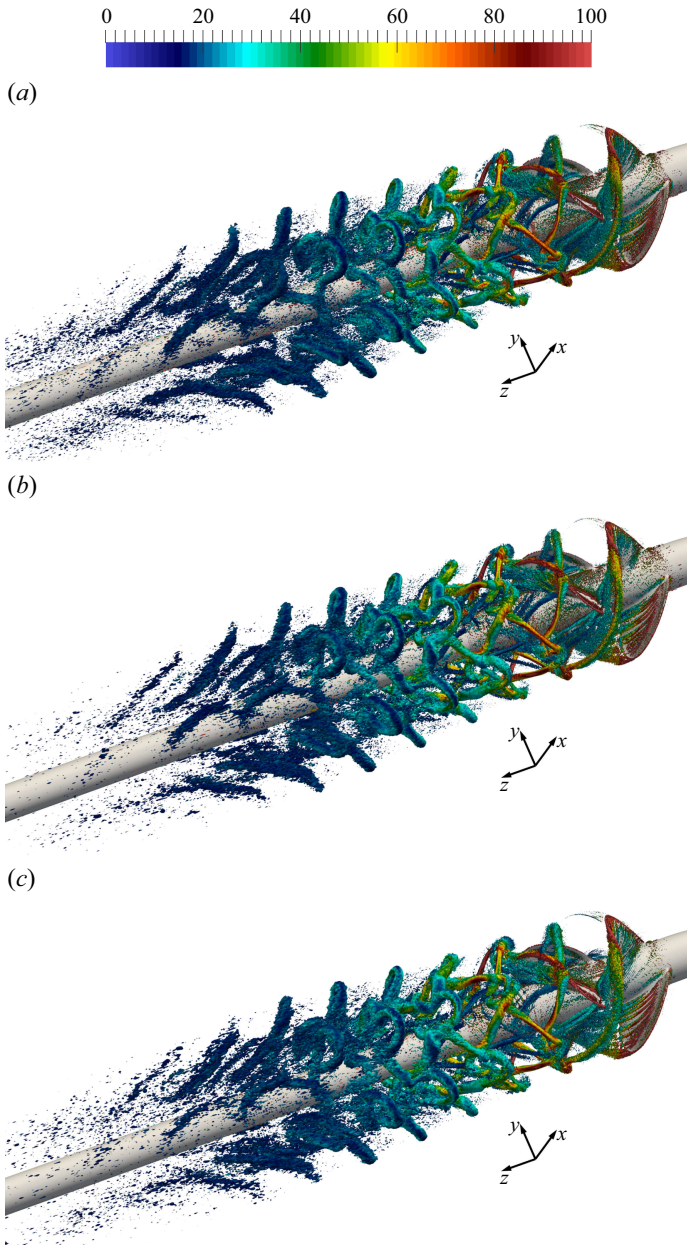


Figure 13. Isosurfaces of phase-averaged second invariant of the velocity gradient tensor ( $Q$ -criterion by Jeong & Hussain 1995,  $\hat{Q}D^2/U_\infty^2 = 200$ ), coloured by vorticity magnitude, scaled by  $U_\infty/D$ . Comparison across the solutions of the CRP system on the (a) fine, (b) medium and (c) coarse grids.

vortices. For instance, at  $z/D = 1.0$  the peak value at the outer boundary of the wake, corresponding to the signature of the tip vortices, is  $\overline{L'}D/U_\infty^2 \approx 218$  for the CRP system, about 86 % and 61 % higher than those in the wake of the FRONT and REAR propellers ( $\overline{L'}D/U_\infty^2 \approx 117$  and  $\overline{L'}D/U_\infty^2 \approx 135$ , respectively). This comparison is reported in more detail in figure 21, where radial profiles are shown at the streamwise coordinates (a)  $z/D = 1.0$ , (b)  $z/D = 2.0$ , (c)  $z/D = 3.0$  and (d)  $z/D = 4.0$ . While a sharp peak is

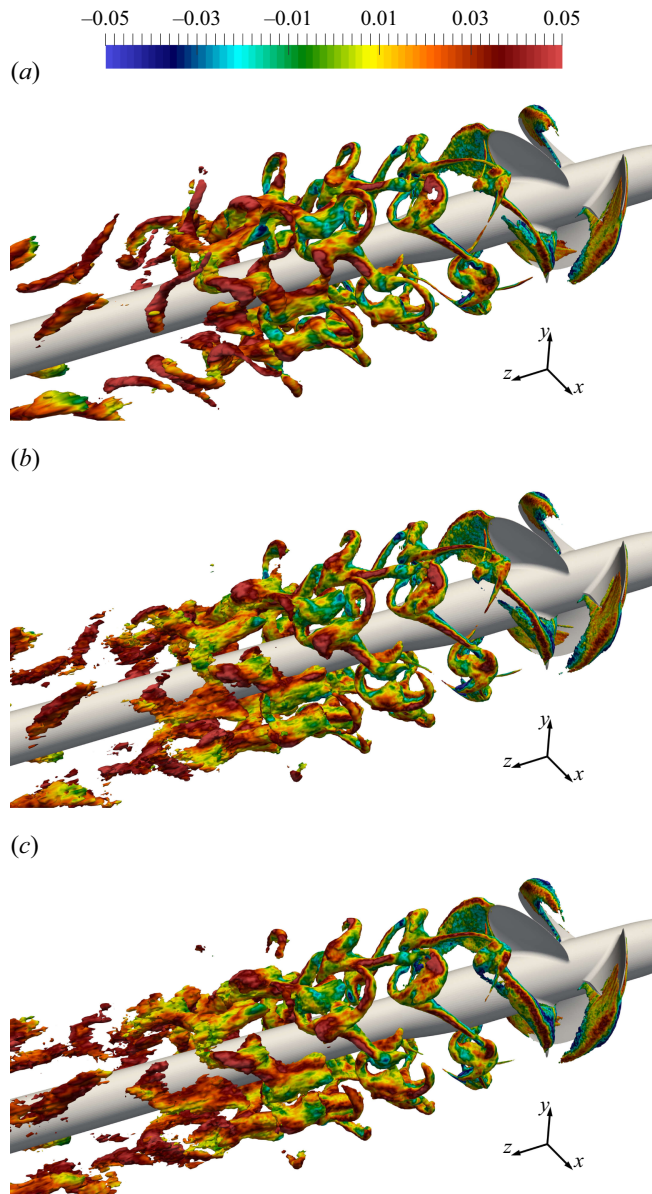


Figure 14. Isosurfaces of phase-averaged turbulent kinetic energy ( $\widehat{k}/U_\infty^2 = 0.15$ ), coloured by the turbulent shear stress  $\widehat{u'w'}$ , scaled by  $U_\infty^2$ . Comparison across the solutions of the CRP system on the (a) fine, (b) medium and (c) coarse grids.

generated in the boundary layer of the downstream shaft, all radial coordinates display higher values of  $\overline{L'}$  for the CRP system.

The overall comparison in the wake across cases is provided in figure 22. The values of  $\overline{L}$  and  $\overline{L'}$  were integrated over cross-sections downstream of the propellers, up to the radial coordinate  $r^*$ , where  $\overline{w}(r^*) = U_\infty$ , assumed as the outer boundary of the wake. This strategy also takes into account the wider radial extent of the wake of the CRP system. Integrals were scaled by using the frontal area of the front propeller,  $A = \pi D^2/4$ , besides

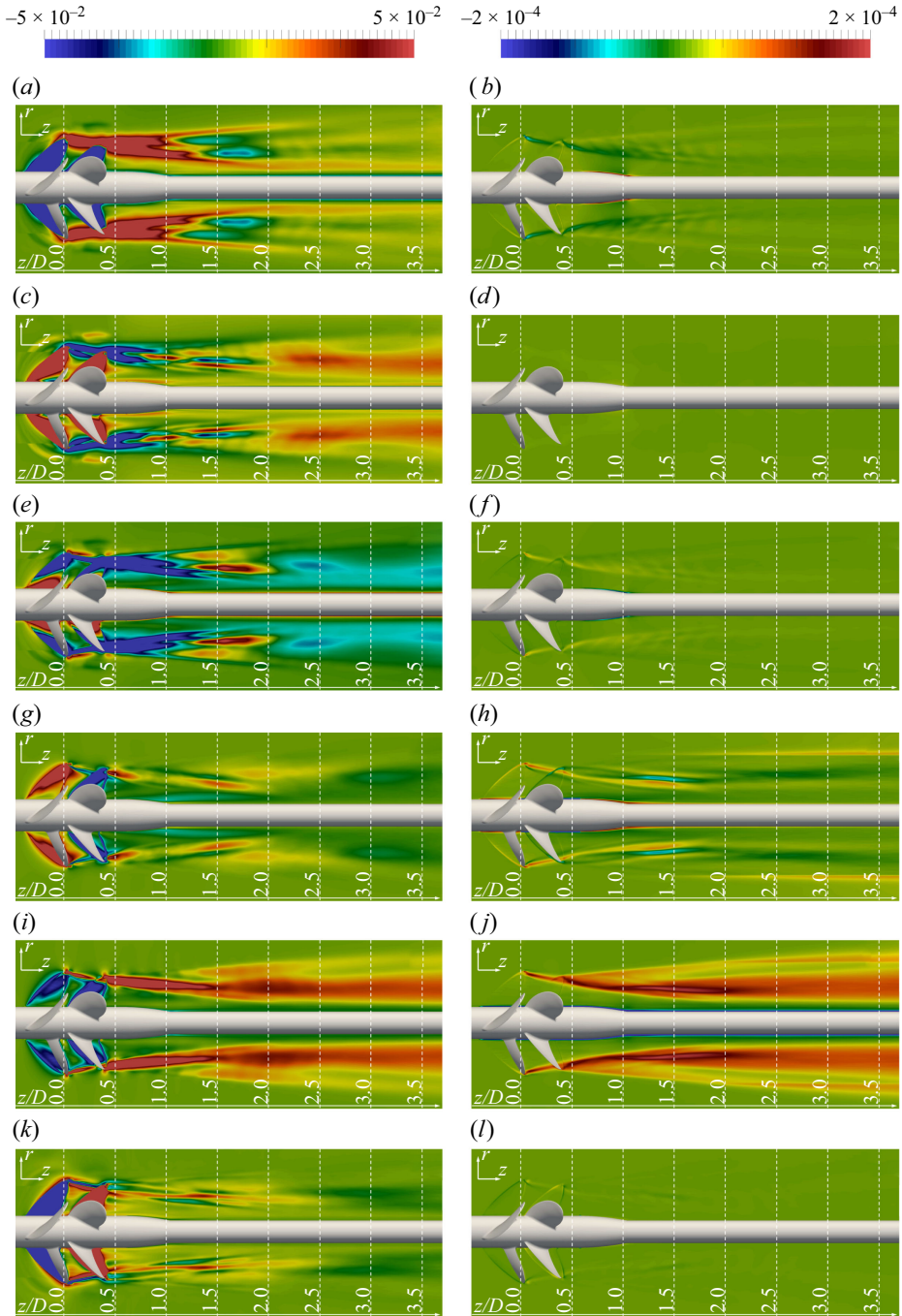


Figure 15. Comparison between the deviatoric parts of the resolved and modelled Reynolds stresses in the wake of the CRP system in the left and right panels. Contours on a meridional plane of the elements (a,b)  $rr$ , (c,d)  $\vartheta\vartheta$ , (e,f)  $zz$ , (g,h)  $r\vartheta$ , (i,j)  $rz$  and (k,l)  $\vartheta z$  of the time-averaged tensors, scaled by  $U_\infty^2$ . Note the difference in the colour scales between left and right panels.

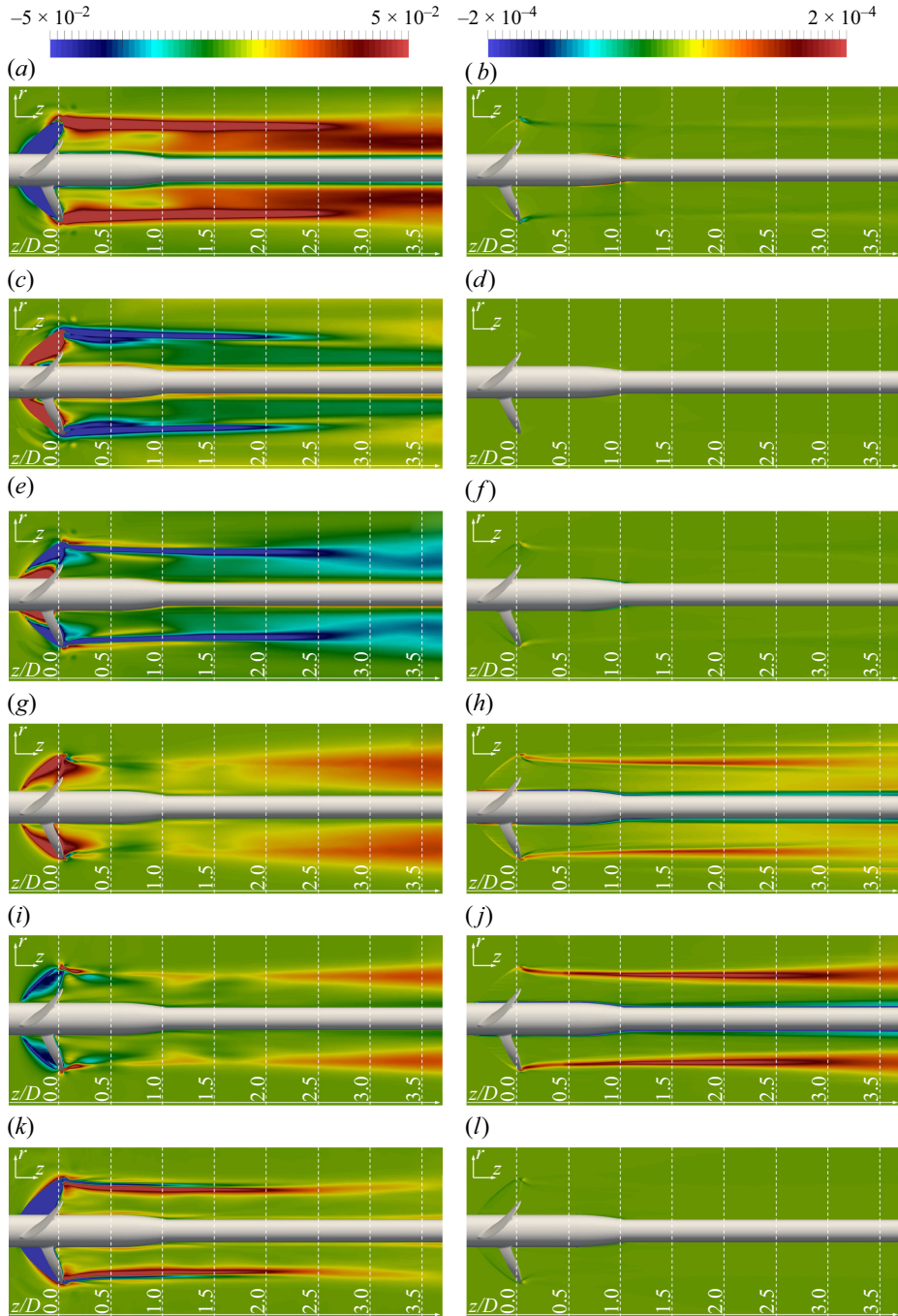


Figure 16. Comparison between the deviatoric parts of the resolved and modelled Reynolds stresses in the wake of the FRONT system in the left and right panels. Contours on a meridional plane of the elements (a,b)  $rr$ , (c,d)  $\vartheta\vartheta$ , (e,f)  $zz$ , (g,h)  $r\vartheta$ , (i,j)  $rz$  and (k,l)  $\vartheta z$  of the time-averaged tensors, scaled by  $U_\infty^2$ . Note the difference in the colour scales between left and right panels.

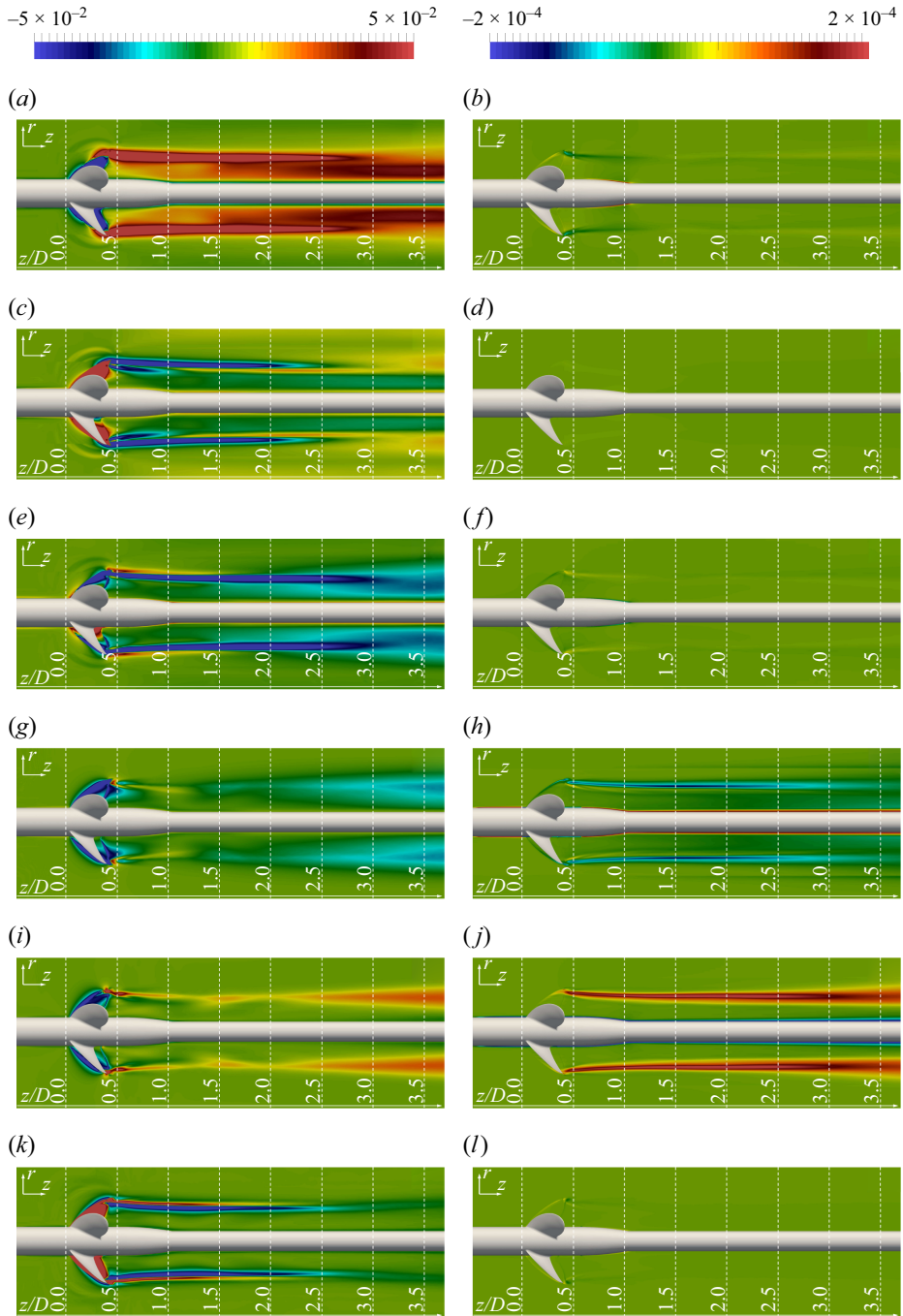


Figure 17. Comparison between the deviatoric parts of the resolved and modelled Reynolds stresses in the wake of the REAR system in the left and right panels. Contours on a meridional plane of the elements (a,b)  $rr$ , (c,d)  $\vartheta\vartheta$ , (e,f)  $zz$ , (g,h)  $r\vartheta$ , (i,j)  $rz$  and (k,l)  $\vartheta z$  of the time-averaged tensors, scaled by  $U_\infty^2$ . Note the difference in the colour scales between left and right panels.

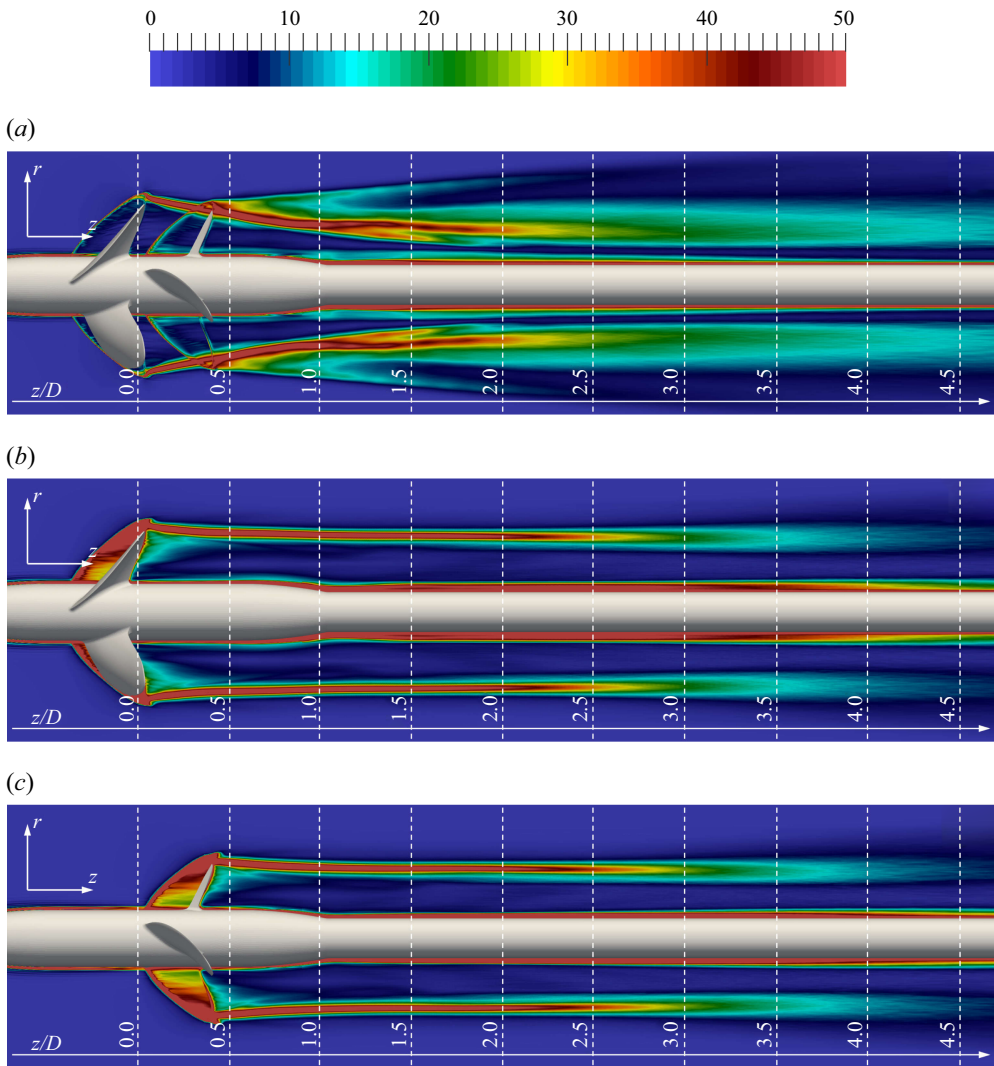


Figure 18. Contours of time-averaged magnitude of the Lamb vector, scaled by  $U_\infty^2/D$ . Comparison across cases (a) CRP, (b) FRONT and (c) REAR.

the free-stream velocity,  $U_\infty$ , and the diameter of the front propeller,  $D$ . Figure 22(a) shows that the radial extent of the wake of the CRP system is significantly larger than that of the two isolated propellers. At  $z/D = 1.0$  it is  $r^*/D \approx 0.516$  for the CRP case, while it is  $r^*/D \approx 0.460$  and  $r^*/D \approx 0.419$  for the FRONT and REAR cases, respectively. This difference grows further at downstream coordinates. At  $z/D = 4.0$  we found a value of  $r^*/D \approx 0.747$  for the CRP case, in contrast with the smaller values of  $r^*/D \approx 0.633$  and  $r^*/D \approx 0.598$  for the FRONT and REAR cases, respectively. This was discussed above as a result of the shear developed between neighbouring vortex rings, projecting their U-shaped vortex lobes towards outer coordinates. The wake of the front propeller is wider than that of the rear propeller, since the former is larger. The overall comparison for the first-order and especially the second-order statistics of  $L$  displays higher values for the CRP case in figures 22(b) and 22(c), respectively. For instance, at  $z/D = 1.0$  the values of  $I[\bar{L}]$  and  $I[\bar{L}']$  for the CRP case are respectively about 1.5 and 3.0 times higher than

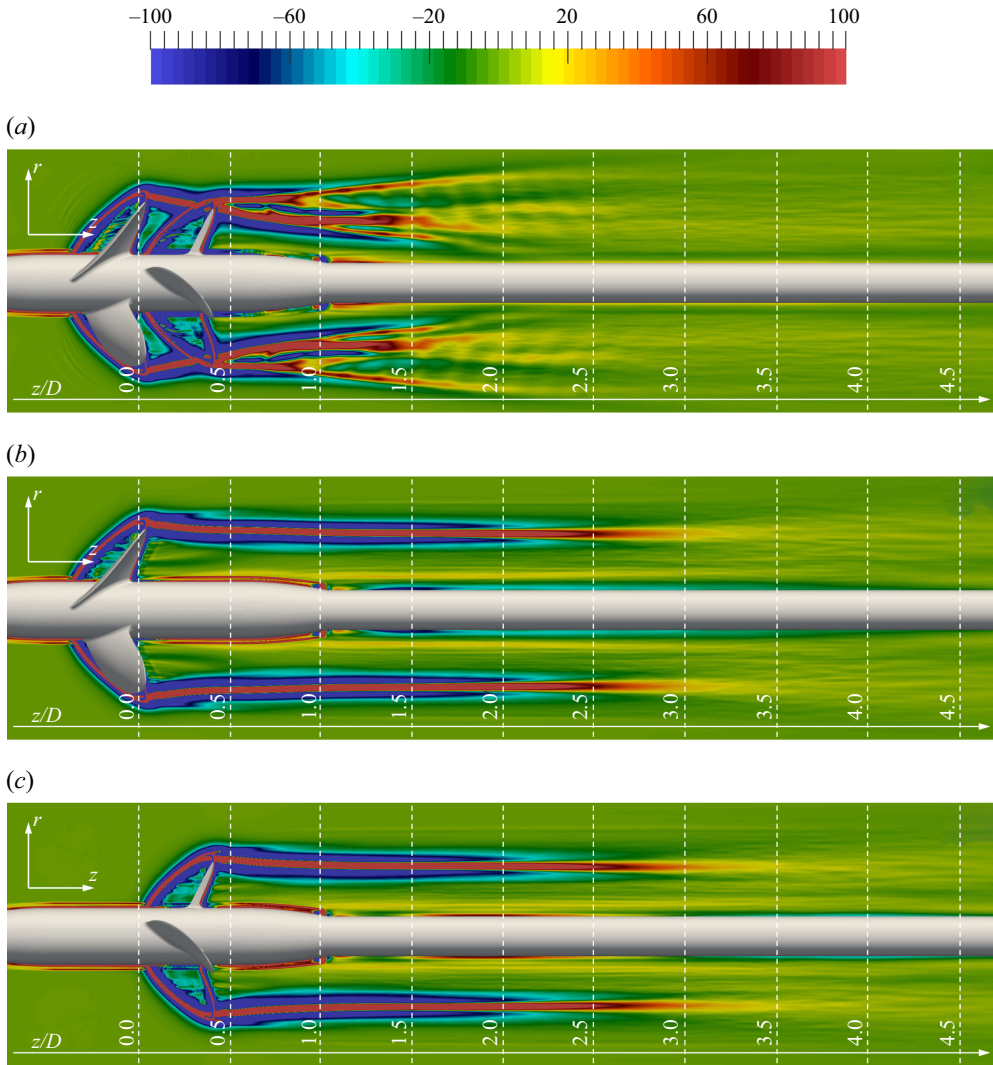


Figure 19. Contours of  $\partial^2 \overline{T}_{ij} / \partial x_i \partial x_j$ , scaled by  $U_\infty^2 / D^2$ . Comparison across cases (a) CRP, (b) FRONT and (c) REAR.

those in the near wake of the isolated propellers. Results are instead more similar between the FRONT and REAR cases. On average, for them, the relative differences on  $I[\overline{L}]$  and  $I[\overline{L}']$  are within 10 % and 20 %, respectively. The statistics of the Lamb vector reported in this section are consistent with the increase of the quadrupole component of the sound coming from vorticity and turbulence in the wake of the CRP system, if compared with the isolated front and rear propellers, as demonstrated in detail in the following sections.

### 6.3. Pressure fluctuations on the surface of the blades

In this section the fluctuations in time of hydrodynamic pressure on the surface of the propellers are discussed, since they are the source of the loading sound radiated from them, which is the component of the acoustic signature associated with the second and third surface integrals in (2.6). This was verified to be the leading linear component of

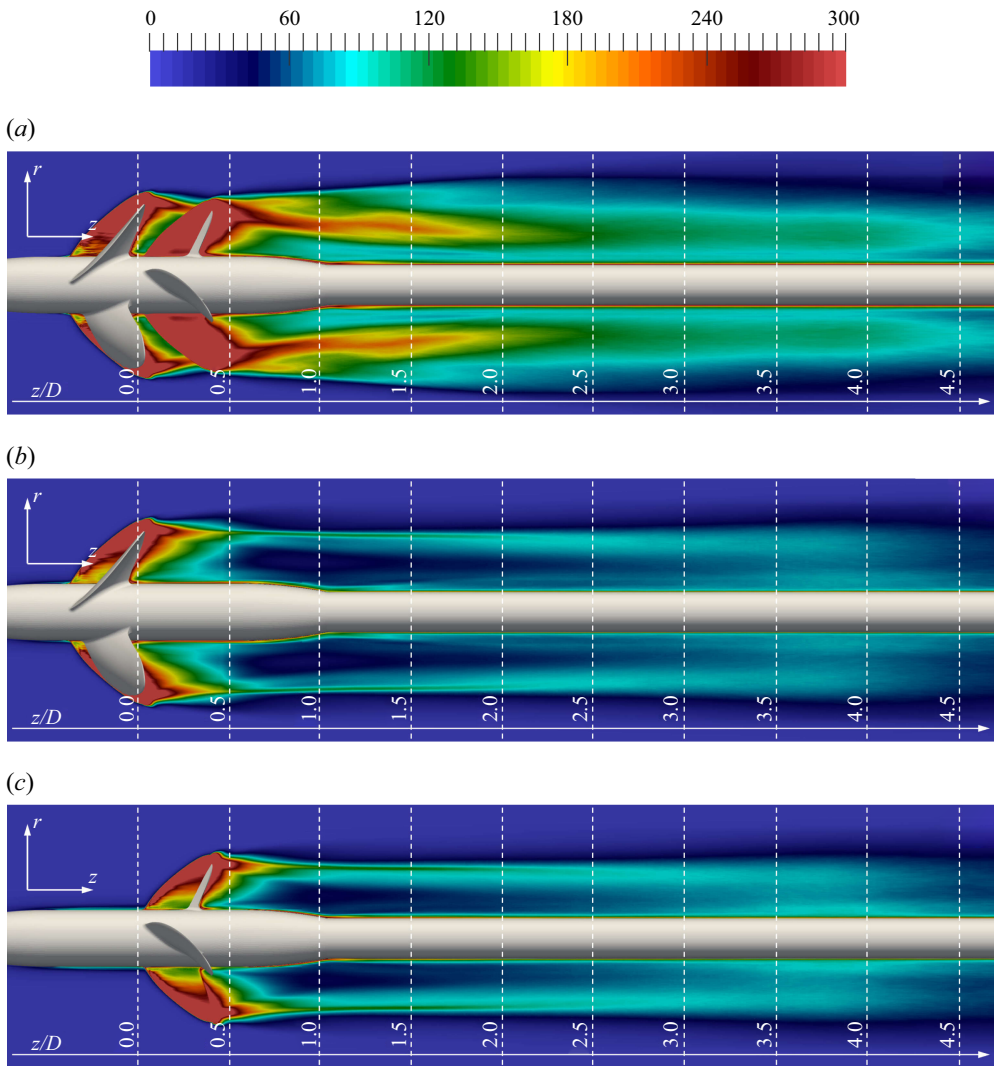


Figure 20. Contours of the root mean squares in time of the magnitude of the Lamb vector, scaled by  $U_\infty^2/D$ . Comparison across cases (a) CRP, (b) FRONT and (c) REAR.

sound, compared with the thickness component, tied to the displacement of fluid by the blades of the propellers and represented by the first surface integral in (2.6).

Figure 23 shows the phase-averaged root mean squares in time of the pressure coefficient at a distance from the suction side of the propeller blades equal to  $0.2\%D$ . It is worth recalling that an IB methodology was adopted for representing the bodies immersed within the flow. This means that, in general, no Eulerian points are placed on the surface of the propeller blades and the no-slip boundary condition is enforced as discussed in § 2. Therefore, the pressure fluctuations in the vicinity of the surface of the blades were extracted by projecting the points of the Lagrangian grids representing the propellers in the outward normal direction towards the fluid region of the computational domain at a distance equivalent to  $0.2\%D$ . Then, the pressure fluctuations from phase-averaged statistics of the solution of the flow were interpolated at those projected points by exploiting the information at the neighbouring Eulerian points. As expected, the levels

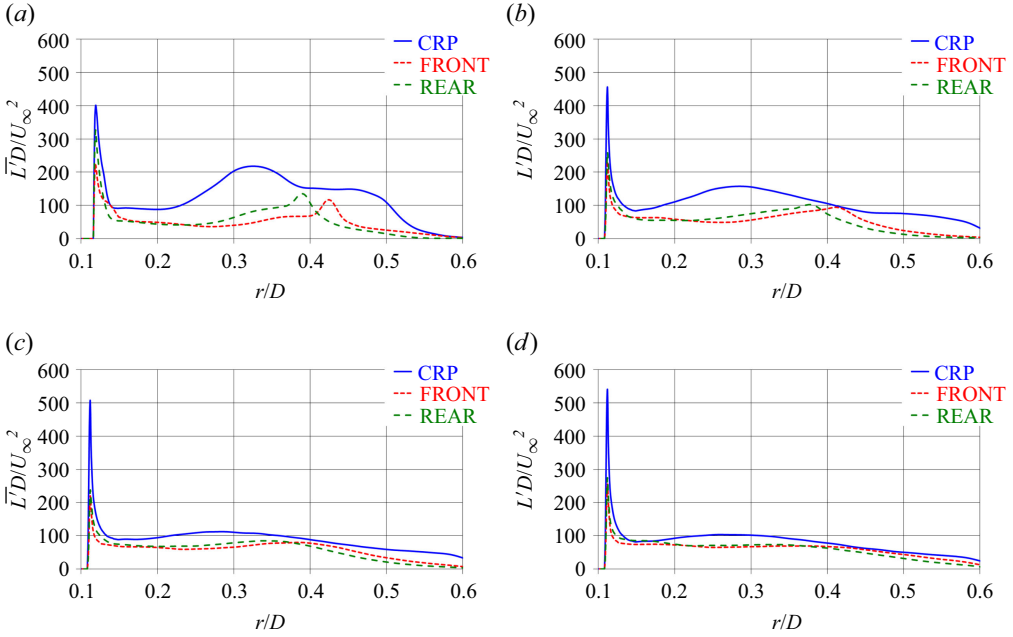


Figure 21. Radial profiles of the root mean squares in time of the magnitude of the Lamb vector, extracted from the data of figure 20 at the streamwise locations (a)  $z/D = 1.0$ , (b)  $z/D = 2.0$ , (c)  $z/D = 3.0$  and (d)  $z/D = 4.0$ .

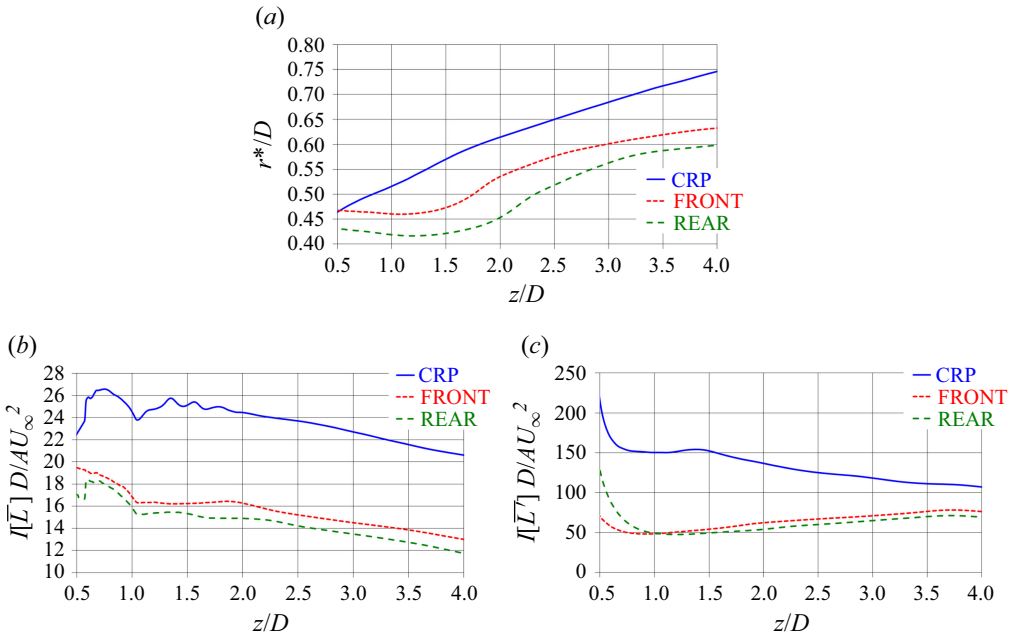


Figure 22. (a) Radial extent of the wake, defined by the condition  $\bar{w}(r^*) = U_\infty$ . (b) Integrals of  $\bar{L}$  over cross-sections of the wake. (c) Integrals of  $\bar{L}'$  over cross-sections of the wake.

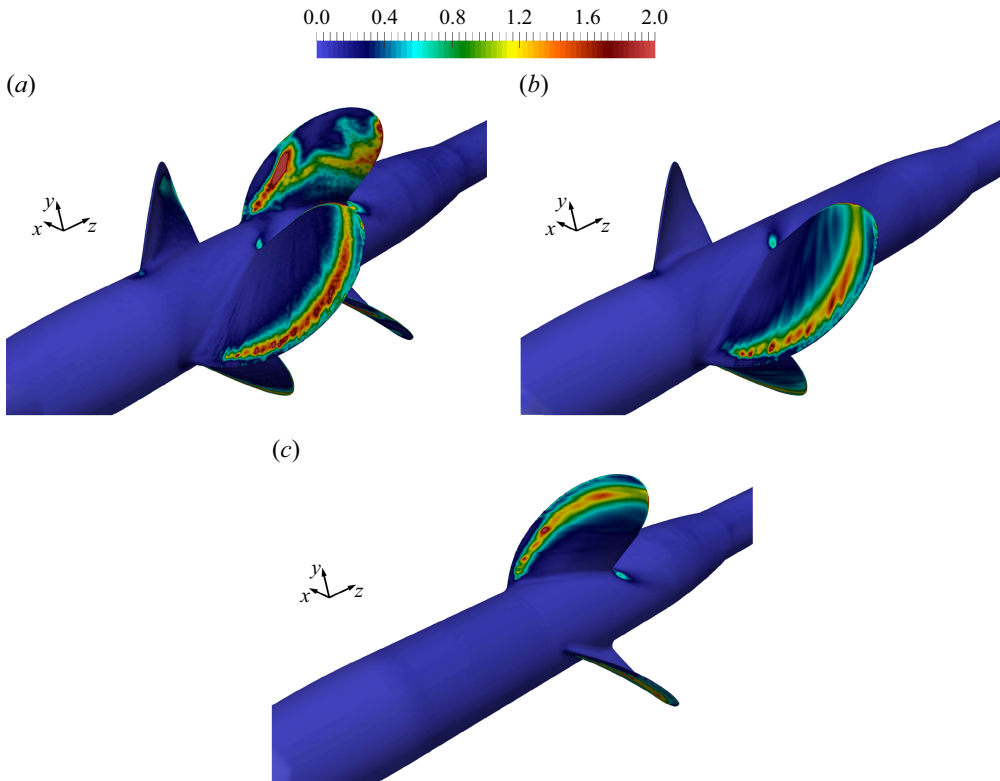


Figure 23. Phase-averaged root mean squares of the fluctuations in time of the pressure coefficient at a distance of  $0.2\%D$  from the suction side of the blades (view from upstream). Comparison across cases (a) CRP, (b) FRONT and (c) REAR.

of pressure fluctuations on the blades of the front propeller are not affected by the presence of the rear propeller. In both the CRP and FRONT cases the boundary layer experiences separation in the vicinity of the leading edge, resulting in an increase of the turbulence levels. The minor differences between the results of figures 23(a) and 23(b), dealing with the CRP and FRONT cases, respectively, are attributable to the suction effect of the rear propeller as well as to the size of the statistical sample. This is larger in the latter case, resulting in more diffused contours. Results display more significant differences between the CRP and REAR cases on the suction side of the blades of the rear propeller. When working in isolation, the distribution of the pressure fluctuations is similar to that observed on the front propeller, resulting from separation phenomena in the vicinity of the leading edge of the blades. This is modified by the wake of the front propeller in the CRP case, resulting in overall higher levels of pressure fluctuations on the rear propeller.

Phase-averaged pressure fluctuations are illustrated also on the pressure side of the propeller blades in figure 24. For comparison purposes, the same colour scale was adopted as in figure 23. Pressure fluctuations are much lower than those produced on the suction side of the blades: (i) no separation phenomena occur on the pressure side of the blades, where the streamwise pressure gradient is favourable and opposes the separation of the boundary layer; (ii) the pressure side of the blades of the rear propeller in the CRP case does not experience the impingement by the wake of the front propeller, therefore, its working condition is not too much modified, in comparison with the REAR case. For the same reason, the distribution of the pressure fluctuations on the pressure side of the blades

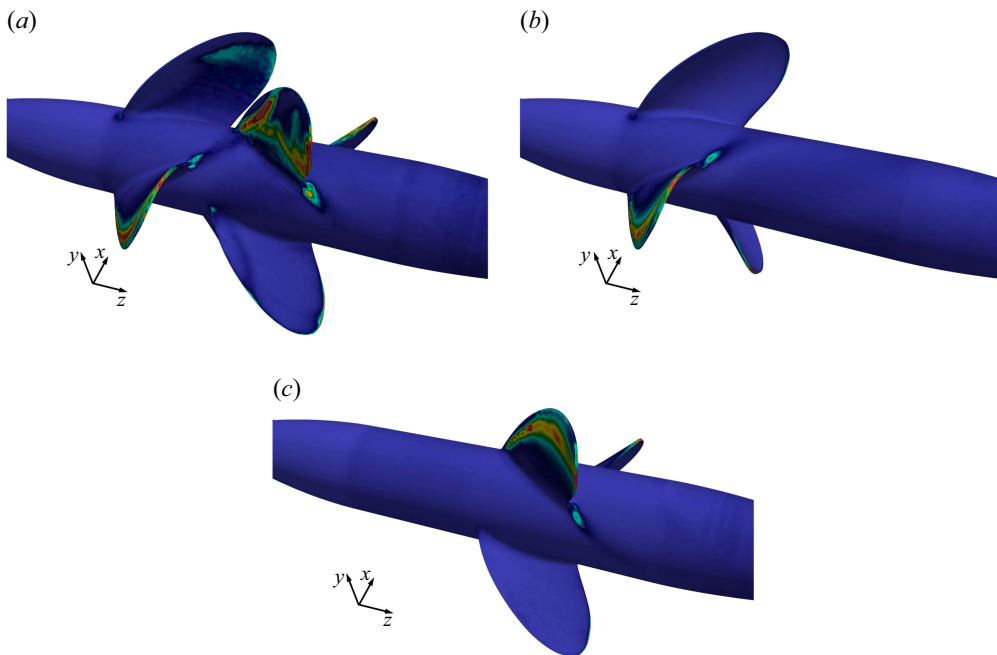
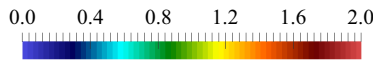


Figure 24. Phase-averaged root mean squares of the fluctuations in time of the pressure coefficient at a distance of  $0.2\%D$  from the pressure side of the blades (view from downstream). Comparison across cases (a) CRP, (b) FRONT and (c) REAR.

of the rear propeller was found practically independent of its position relative to the front propeller, keeping much lower values than on the suction side.

Comparisons across resolutions of the computational grid are reported in [figure 25](#). Although second-order statistics are considered, the agreement across grids is fairly good. In all panels of [figure 25](#), the pressure fluctuations on the suction side of the blades of the front propeller are dominated by the separation of the boundary layer just downstream of their leading edge. This is also the case for the pressure fluctuations on the suction side of the blades of the rear propeller at their inner radial coordinates, while the impingement of the wake and tip vortices shed by the blades of the front propeller is visible at outer radii. This topology of the contours as well as their maxima are not modified across grid resolutions.

#### 6.4. Narrow-band spectra of the SPLs

Comparisons across cases are reported in terms of narrow-band spectra in [figure 26](#), which refers to the radial location  $r/D = 1.0$  (hydrophones located at  $x/D = 0.0$  and  $y/D = 1.0$  are considered) and the streamwise locations at (a)  $z/D = -0.1$ , (b)  $z/D = 0.3$ , (c)  $z/D = 2.0$  and (d)  $z/D = 3.0$ . The first two streamwise coordinates are aligned with the front and rear propellers, respectively. There, the SPLs from the CRP system at the blade frequency are only slightly higher, in comparison with those from the isolated propellers, within 10 dB. Interestingly, differences become more obvious, even above 20 dB, at higher harmonics of the blade frequency, where the acoustic signature of the CRP system is actually stronger than those of the two isolated propellers. Differences of about 10 dB are also visible at the highest resolved frequencies of the acoustic field. The increase in

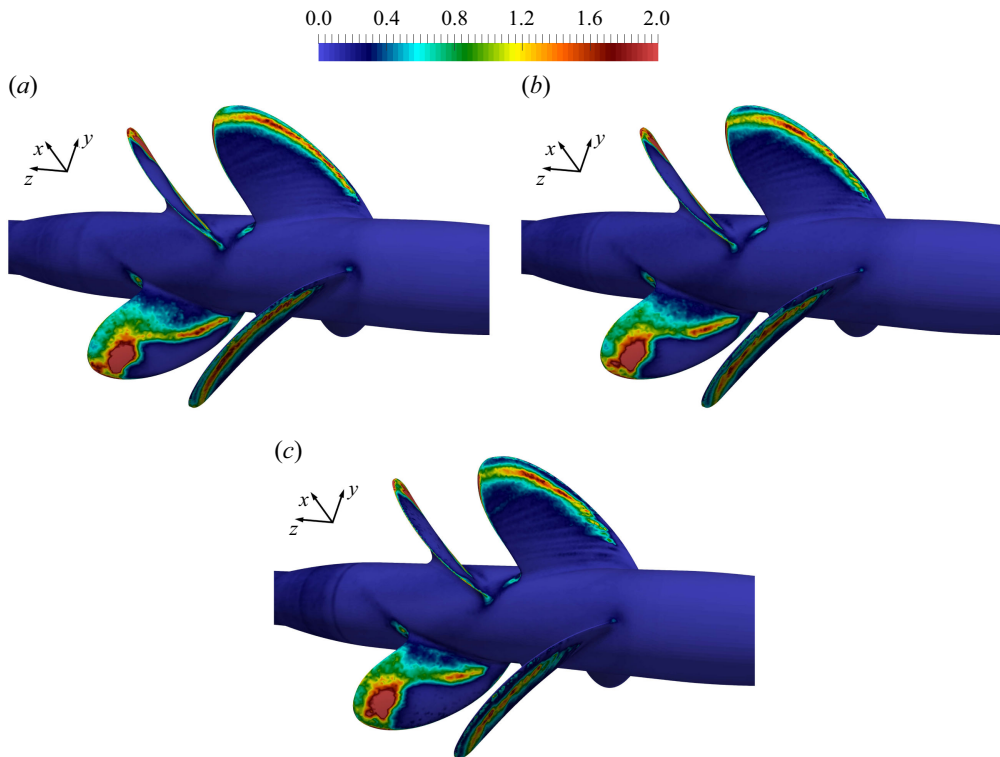


Figure 25. Phase-averaged root mean squares of the fluctuations in time of the pressure coefficient at a distance of  $0.2\%D$  from the suction side of the blades (view from upstream). Comparison across the solutions of the CRP system on the (a) fine, (b) medium and (c) coarse grids.

sound levels for the CRP system is likely due to the turbulent flow interaction between the trailing wake of the front blades and the leading edge of the rear blades. The spectra at  $z/D = 2.0$  in [figure 26\(c\)](#) display a substantial change. For all CRP, FRONT and REAR cases, compared with the upstream locations in the vicinity of the propellers, higher SPLs occur at low frequencies (below the blade frequency), above the values around 120 dB achieved in [figure 26\(a,b\)](#), due to the growing importance of the nonlinear component of sound, which is especially affected by the structures populating the wake. For the CRP case, the SPLs at the smallest frequencies are above 140 dB, while they keep slightly below this threshold for both FRONT and REAR cases. At this location, the increase of the sound levels of the CRP case, relative to both FRONT and REAR cases, is evident also at the smallest frequencies, which is a result of the reinforced complexity of the wake system, compared with the isolated propellers. This result becomes even more obvious at  $z/D = 3.0$ , where the SPLs from the CRP system are higher than those from the FRONT and REAR systems across the whole range of frequencies. It is also interesting to see that the sound from the isolated front propeller, despite its larger distance from the particular hydrophone of [figure 26\(d\)](#), is more intense than that from the isolated rear propeller, since the former is more loaded than the latter.

Results are reported in [figure 27](#) at the same hydrophones as in [figure 26](#), but exploiting the data of the LES computations conducted on the CRP system on the medium and coarse grids, together with those from the fine grid. The spectra in [figure 27](#) show an acceptable agreement across resolutions also in terms of acoustic field radiated from the

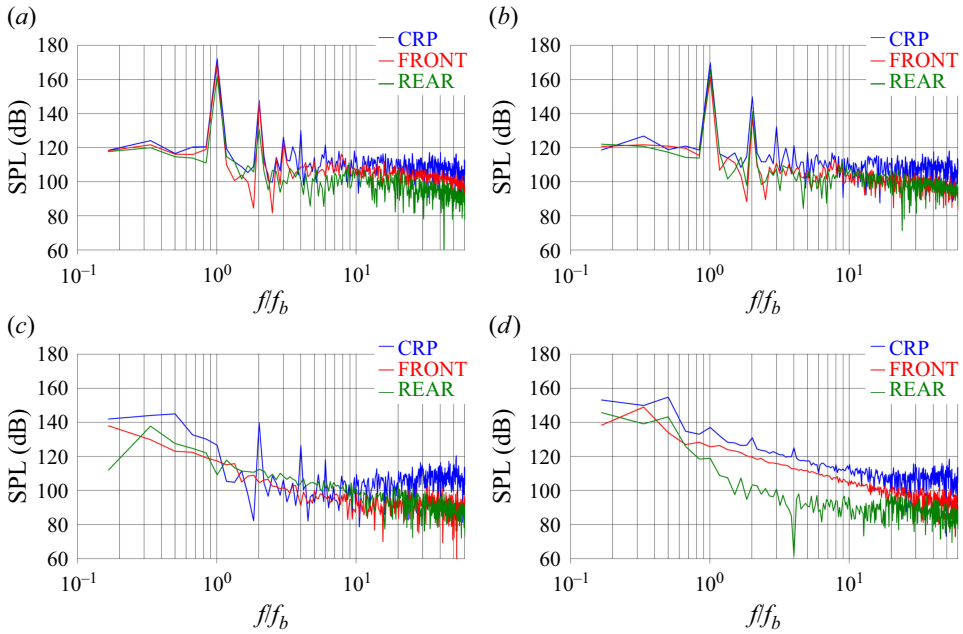


Figure 26. The SPLs in narrow-band spectra for the CRP, FRONT and REAR systems at hydrophones of coordinates  $x/D = 0.0$ ,  $y/D = 1.0$  and (a)  $z/D = -0.1$ , (b)  $z/D = 0.3$ , (c)  $z/D = 2.0$ , (d)  $z/D = 3.0$ .

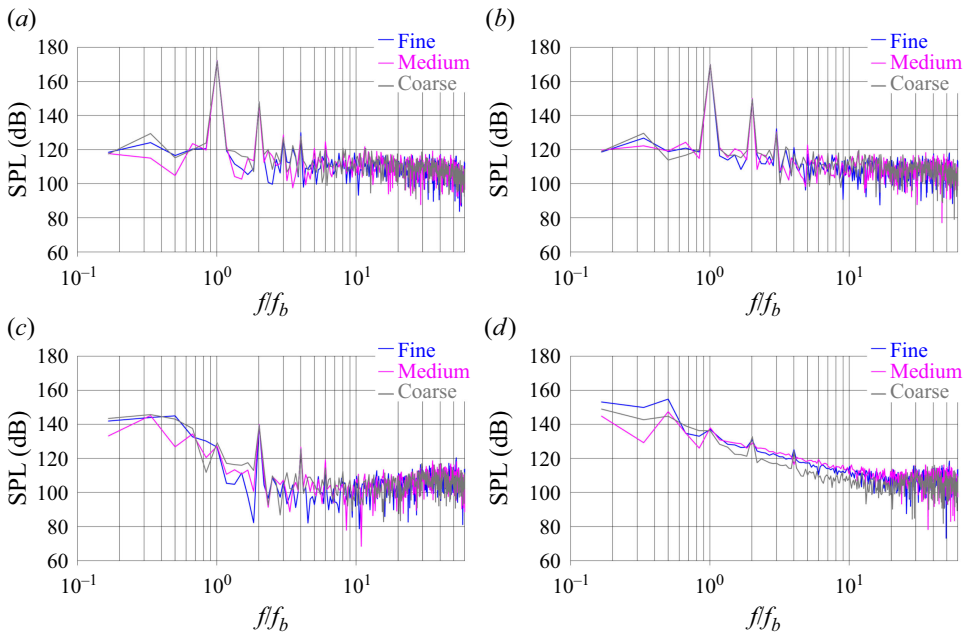


Figure 27. The SPLs in narrow-band spectra from the computations dealing with the CRP system on the fine, medium and coarse grids at hydrophones of coordinates  $x/D = 0.0$ ,  $y/D = 1.0$  and (a)  $z/D = -0.1$ , (b)  $z/D = 0.3$ , (c)  $z/D = 2.0$ , (d)  $z/D = 3.0$ .

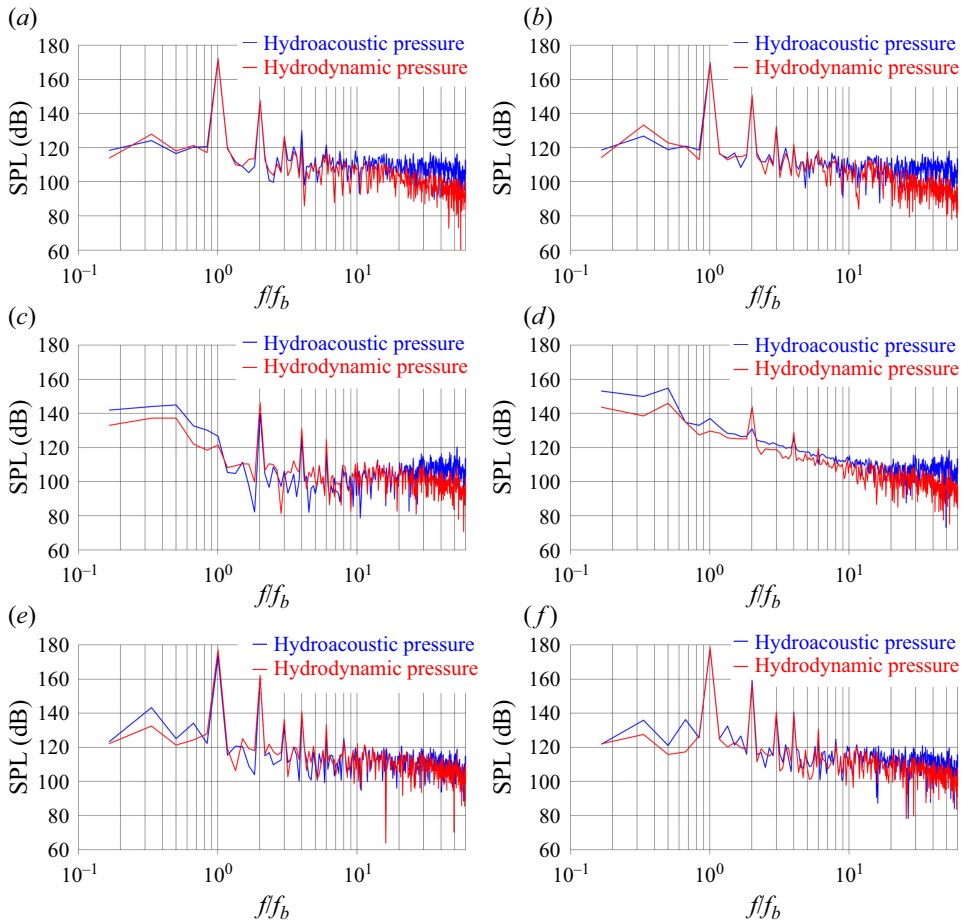


Figure 28. The SPLs in narrow-band spectra from the computations dealing with the CRP system at hydrophones of coordinates  $x/D$ ,  $y/D$ ,  $z/D$  equal to (a) 0.0, 1.0,  $-0.1$ , (b) 0.0, 1.0, 0.3, (c) 0.0, 1.0, 2.0, (d) 0.0, 1.0, 3.0, (e) 0.0, 0.2,  $-0.5$  and (f) 0.0, 0.4,  $-0.5$ : comparison between spectra of hydroacoustic and hydrodynamic pressure.

contra-rotating propellers, especially at tonal frequencies, although some deviations still persist, especially at the lowest frequencies.

In figure 28 narrow-band spectra for the CRP system are reported at the same locations for the comparisons between hydroacoustic and hydrodynamic pressure. As expected, at the closest locations in figure 28(a,b), which are aligned with the streamwise coordinates of the front and rear propellers, respectively, spectra are close between each other, especially at the tonal frequencies, which is a confirmation of the accuracy of the FWH reconstruction of the acoustic field. Differences grow towards higher frequencies, since the distance from the sources of sound is increasing in wavelengths. Moving away from the propellers, towards downstream coordinates, the deviations between the spectra of hydroacoustic and hydrodynamic pressure become more significant, due to compressibility effects, as shown in figure 28(c,d). For additional verification, we also moved to locations closer to the CRP system, that is, at the coordinates  $x/D = 0.0$ ,  $y/D = 0.2, 0.4$  and  $z/D = -0.5$ . Since hydrophones need to be placed outside the control volume selected for the computation of the quadrupole component of sound, in this particular case we considered

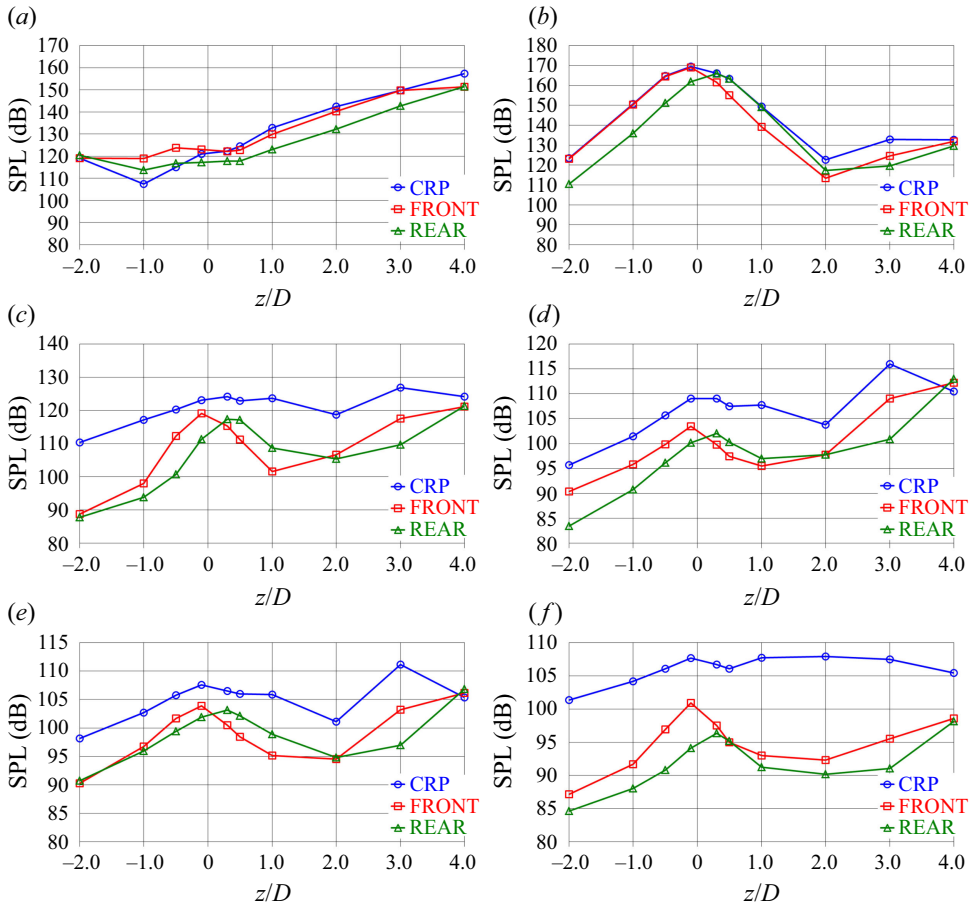


Figure 29. Streamwise evolution of the SPLs from the CRP, FRONT and REAR systems at the radial coordinate  $r/D=1.0$  in the third-octave bands centred at the frequencies (a)  $f/f_b=1/3$ , (b)  $f/f_b=1$ , (c)  $f/f_b=2$ , (d)  $f/f_b=5$ , (e)  $f/f_b=10$  and (f)  $f/f_b=30$ . Azimuthal averages across the 72 hydrophones placed at each streamwise coordinate.

a control volume with an upstream boundary at  $z/D = -0.4$  (rather than  $z/D = -2.5$ ). This choice is based on the assumption that the upstream region  $-2.5 < z/D < -0.4$  of the original control volume discussed in § 5 gives only a small contribution to the overall acoustic signature, being the major sources located on the propeller blades and in the wake flow. Then, we verified that in figure 28(e,f), referring to hydrophones closer to the CRP system, the agreement between the spectra of hydroacoustic and hydrodynamic pressure is even closer at the highest frequencies, if compared with the hydrophones considered in the other panels of figure 28.

### 6.5. The SPLs in third-octave bands: streamwise evolution

Due to the large dataset to be reported, the SPLs were computed in third-octave bands and averaged across the azimuthal direction, with the purpose of producing a more global overview of the acoustic signature and its comparison across cases. Figure 29 shows the streamwise evolution of the SPLs at  $r/D = 1.0$  in the third-octave bands centred at the frequencies (a)  $f/f_b = 1/3$ , (b)  $f/f_b = 1$ , (c)  $f/f_b = 2$ , (d)  $f/f_b = 5$ , (e)  $f/f_b = 10$  and (f)  $f/f_b = 30$ . It is interesting to see that at the shaft frequency, considered in figure 29(a),

the streamwise evolution of the SPLs is growing, due to the instability of the wake system, reinforcing the quadrupole component of the acoustic signature. The results in [figure 29\(b\)](#) deal with the blade frequency. In the vicinity of the propellers ( $z/D \approx 0$ ) the SPLs are similar across cases: the major differences between the FRONT and REAR cases are due to the different streamwise locations of the two propellers. As a result, the acoustic signature of the latter is shifted downstream. Close to the propellers the CRP system displays similar sound levels to the FRONT and REAR systems. This is not the case further downstream, where the increased complexity of the wake system reinforces the quadrupole component of the acoustic emission from the CRP system, compared with the FRONT and REAR systems. However, the impact of the interaction between propellers becomes more evident at the frequency  $f/f_b = 2$ , in [figure 29\(c\)](#), where the SPLs for the CRP system are the highest across all streamwise coordinates. This is also the case at higher frequencies, as demonstrated by the remaining panels of [figure 29](#). It should be noted that, although the SPLs from the contra-rotating system were usually found higher than those from the isolated propellers, these differences can be deemed small, when considering that the former is producing more than twice the thrust of the latter. Meanwhile, the following discussion will demonstrate that this increase of the SPLs of the CRP system is mainly attributable to the reinforced contribution of the nonlinear component to the overall sound.

The streamwise evolution of the SPLs for the CRP case, reported in [figure 29](#), is further analysed through a comparison across the components of the overall acoustic signature in [figure 30](#). In this figure, the linear sound radiated from the surfaces of the upstream shaft (linear 1), the front propeller (linear 2), the rear propeller (linear 3) and the downstream shaft (linear 4) are separated from the nonlinear sound, which is instead mainly associated with the wake flow. The six panels of [figure 30](#) deal with the same frequencies as those of [figure 29](#). The shaft frequency is dominated by the nonlinear component across all streamwise coordinates, as demonstrated by [figure 30\(a\)](#). This is also the reason for the increasing trend in the streamwise direction, due to the growing instability of the wake system downstream of the two propellers. At the blade frequency, considered in [figure 30\(b\)](#), the relative importance of the different components of sound is modified, if compared with that seen in [figure 30\(a\)](#) at the shaft frequency. In the vicinity of the propellers the acoustic signature of the system is dominated by the sound radiated from their surface, represented by linear 2 and linear 3. However, starting at  $z/D = 2.0$  the nonlinear component becomes the leading one. This also explains the switch from a decreasing streamwise trend of the overall SPLs, due to the declining linear sound from the two propellers, to an increasing one, due to the rising quadrupole component from the wake structures. This is the same behaviour verified at higher frequencies, as demonstrated by the other panels of [figure 30](#). In these panels it is also interesting to see that the sound radiated from the rear propeller is always higher than that from the front one. This is the result of the rear propeller operating in the wake of the front propeller and experiencing higher levels of pressure fluctuations on the suction side of its blades, as discussed above.

Comparisons across grid resolutions are presented in [figure 31](#) for the CRP system in terms of streamwise evolution of the SPLs in third-octave bands. Despite the complexity of the flow physics and the resulting acoustic signature and the substantial change of the number of points across grids, the agreement across resolutions is satisfactory, especially between the medium and fine grids. The coarse grid provides similar results, with the exception of [figure 31\(a\)](#), relative to the shaft frequency, at streamwise coordinates in the vicinity of the propellers. Although some differences still persist across resolutions, the comparison with the results in [figure 30](#) shows that the deviations across grids are below those observed between linear and nonlinear terms of the acoustic signature, confirming the importance of the latter as the instability of the wake system develops.

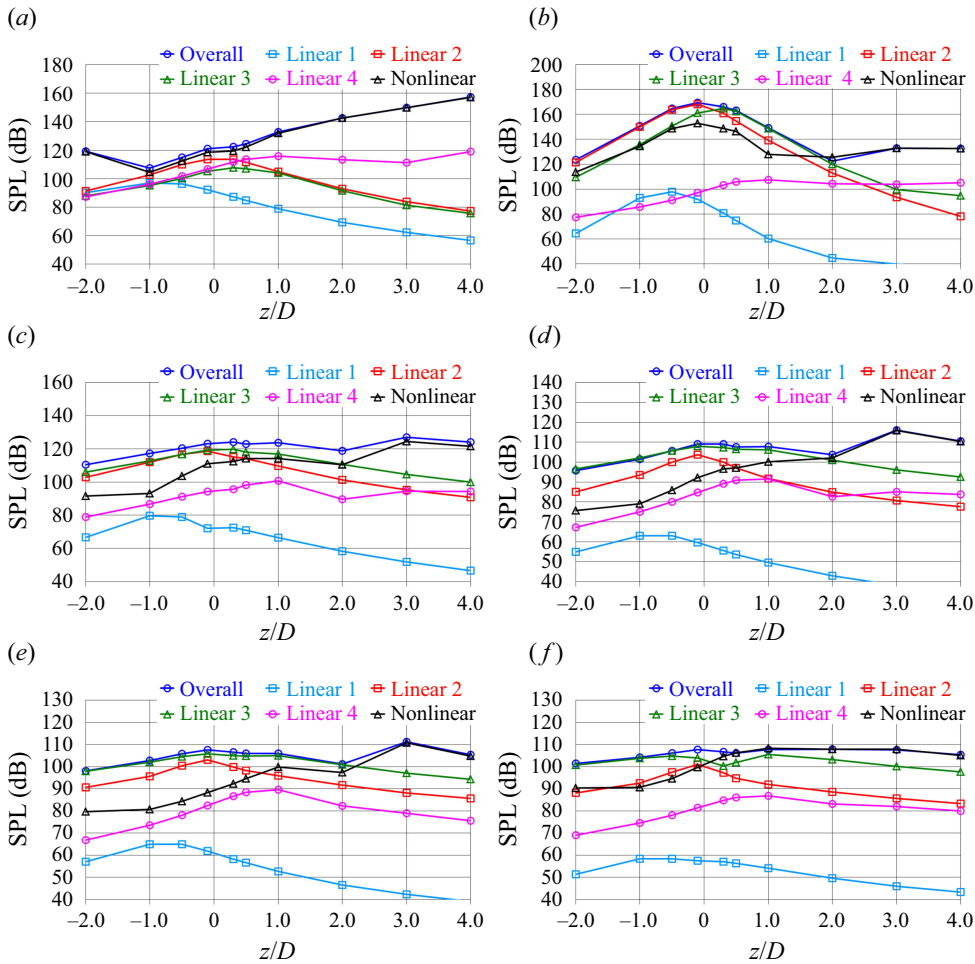


Figure 30. Streamwise evolution of the SPLs from the CRP system at the radial coordinate  $r/D = 1.0$  in the third-octave bands centred at the frequencies (a)  $f/f_b = 1/3$ , (b)  $f/f_b = 1$ , (c)  $f/f_b = 2$ , (d)  $f/f_b = 5$ , (e)  $f/f_b = 10$  and (f)  $f/f_b = 30$ . Azimuthal averages across the 72 hydrophones placed at each streamwise coordinate. Comparison across the SPLs from the upstream shaft (linear 1), the front propeller (linear 2), the rear propeller (linear 3), the downstream shaft (linear 4) and the wake flow (nonlinear).

### 6.6. The SPLs in third-octave bands: radial evolution

Also in this section the SPLs are reported in third-octave bands, computed as their azimuthal averages across the 72 hydrophones placed at each radial and axial location to increase the size of the statistical sample. Figure 32 deals with the radial evolution at the streamwise coordinate  $z/D = 0.3$ , which is aligned with the rear propeller. We verified that this streamwise location is well representative of the radial trend of the SPLs at the other available streamwise coordinates. Again, the frequencies (a)  $f/f_b = 1/3$ , (b)  $f/f_b = 1$ , (c)  $f/f_b = 2$ , (d)  $f/f_b = 5$ , (e)  $f/f_b = 10$  and (f)  $f/f_b = 30$  are considered in figure 32. Figure 32(a) demonstrates that across all radii the acoustic signature at the shaft frequency is not reinforced by the interaction between the front and rear propellers of the CRP system. At the blade frequency in figure 32(b) the same behaviour is found at small radial coordinates. However, moving away from the propellers, the rate of decay of the acoustic signature becomes slower for the CRP system than for the isolated propellers.

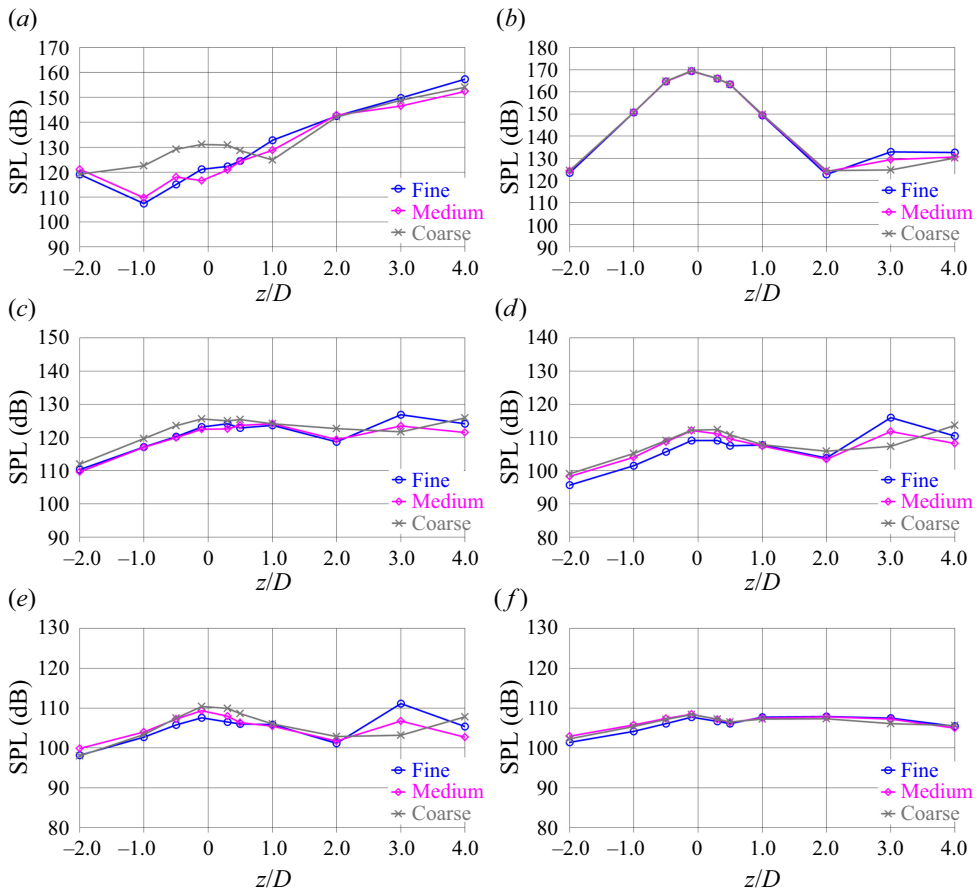


Figure 31. Streamwise evolution of the SPLs from the computations dealing with the CRP system on the fine, medium and coarse grids at the radial coordinate  $r/D = 1.0$  in the third-octave bands centred at the frequencies (a)  $f/f_b = 1/3$ , (b)  $f/f_b = 1$ , (c)  $f/f_b = 2$ , (d)  $f/f_b = 5$ , (e)  $f/f_b = 10$  and (f)  $f/f_b = 30$ . Azimuthal averages across the 72 hydrophones placed at each streamwise coordinate.

This is also the case in [figure 32\(c\)](#), although at the relevant frequency ( $f/f_b = 2$ ) the SPLs from the CRP system are already higher at small radial coordinates and this trend is reinforced moving further away. At the higher frequencies considered in the remaining panels of [figure 32](#) the results are consistent across all radial coordinates: the SPLs are similar between FRONT and REAR systems and are reinforced by the interaction between the two propellers working together within the CRP system.

The result observed in [figure 32\(b\)](#) at the blade frequency is especially interesting. While in the vicinity of the propellers the SPLs are similar across cases, they become higher for the CRP system at outer radial coordinates, due to their slower decay. The source of this behaviour was investigated in more detail. [Figures 33–35](#) show a comparison across several components of the acoustic signature from CRP, FRONT and REAR, respectively, using the same decomposition already considered in [figure 30](#). In [figure 33\(a\)](#), dealing with the shaft frequency for the CRP case, the acoustic near field is dominated by the nonlinear sound, although this changes in part at the outermost radial coordinates. This is not the case at the blade frequency, as shown in [figure 33\(b\)](#), where the radial evolution displays a switch from an acoustic signature dominated by the linear sound from the front

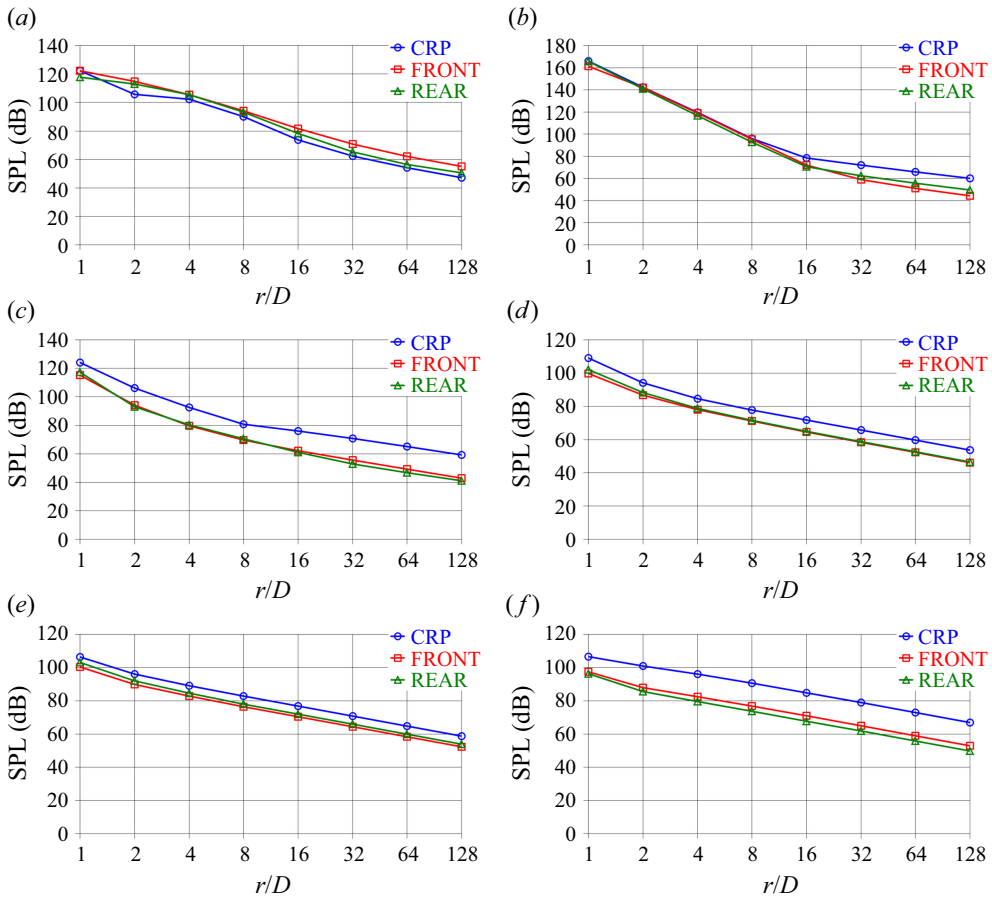


Figure 32. Radial evolution of the SPLs from the CRP, FRONT and REAR systems at the streamwise coordinate  $z/D=0.3$  in the third-octave bands centred at the frequencies (a)  $f/f_b = 1/3$ , (b)  $f/f_b = 1$ , (c)  $f/f_b = 2$ , (d)  $f/f_b = 5$ , (e)  $f/f_b = 10$  and (f)  $f/f_b = 30$ . Azimuthal averages across the 72 hydrophones placed at each radial coordinate. Note that the scale of the horizontal axis is logarithmic.

propeller (linear 2) to one dominated by the nonlinear sound, showing a slower rate of radial decay. In contrast, in figure 34(b), dealing with the isolated front propeller, the linear components are still the leading ones at the outermost radial coordinates and the nonlinear one is smaller than that in figure 33(b) from the CRP system. It should be noted that in figure 34(b) the component linear 3 stands for the SPLs coming from the surface of the dummy hub replacing the rear propeller in the FRONT case. Similar results are shown in figure 35(b), where the linear sound is the leading one across the whole range of radial coordinates. In that case, linear 2 is the linear component of sound radiated from the surface of the dummy hub replacing the front propeller in the REAR case. The nonlinear sound is again smaller than that generated by the wake of the CRP system. A similar behaviour is observed for increasing frequencies, but the radial location where the nonlinear sound becomes the leading one in the acoustic field generated by the CRP system shifts closer to the propellers. Actually, at the highest frequency  $f = 30f_b$  this event occurs even in the cases of the isolated propellers, as shown in figures 34(f) and 35(f), where the nonlinear sound becomes the highest across all components, although keeping smaller in comparison with its levels for the CRP system.

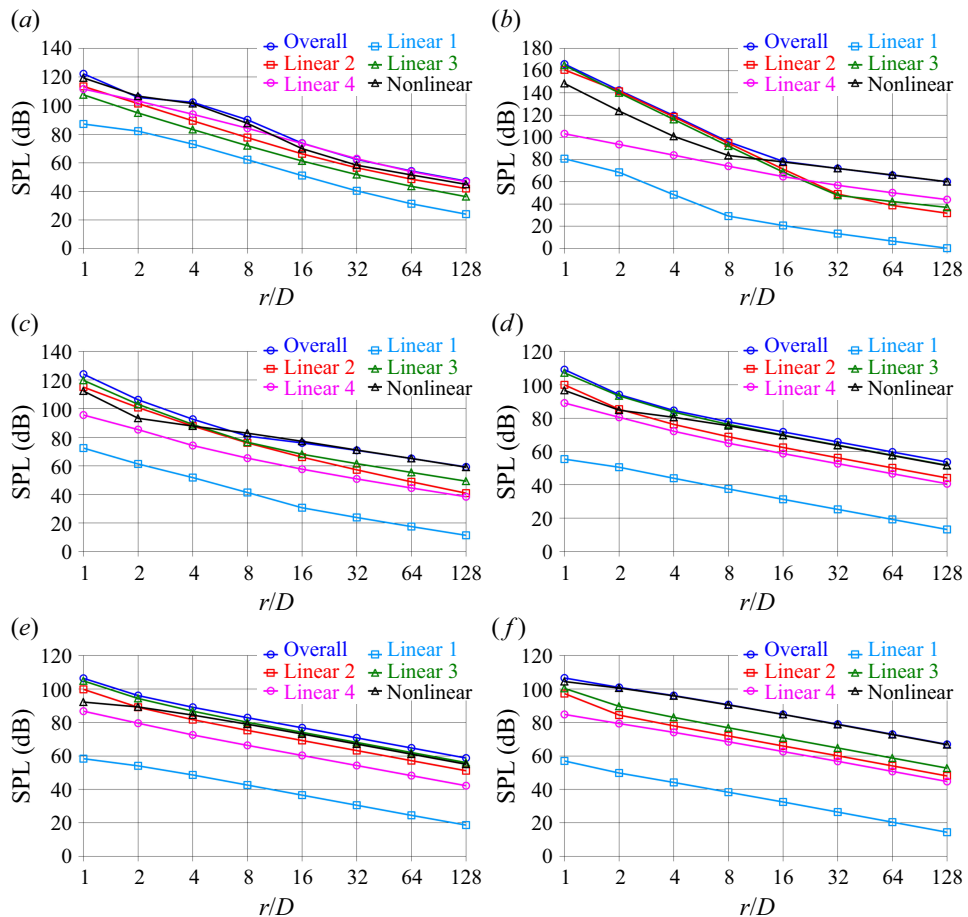


Figure 33. Radial evolution of the SPLs at the streamwise coordinate  $z/D = 0.3$  for the CRP system in the third-octave bands centred at the frequencies (a)  $f/f_b = 1/3$ , (b)  $f/f_b = 1$ , (c)  $f/f_b = 2$ , (d)  $f/f_b = 5$ , (e)  $f/f_b = 10$  and (f)  $f/f_b = 30$ . Azimuthal averages across the 72 hydrophones placed at each radial coordinate. Note that the scale of the horizontal axis is logarithmic. Comparison across the SPLs from the upstream shaft (linear 1), the front propeller (linear 2), the rear propeller (linear 3), the downstream shaft (linear 4) and the wake flow (nonlinear).

The results in figure 33 show that, in contrast with the cases of the isolated propellers, for the CRP system the nonlinear sound at outer radial coordinates becomes stronger than the linear one. This explains, for instance, why at small radii the SPLs at the blade frequency in figure 32(b) are similar across cases, while moving away from the propellers they become higher for the CRP system, in comparison with both propellers working alone. This is not obvious, since the literature usually assumes the nonlinear sound to become negligible as the receiver moves away from the sources. The present results show that, while this may be the case for the isolated propellers, the complex wake system of contra-rotating propellers makes the nonlinear sound significant and non-negligible even at the outermost radial locations. This result was verified also at other frequencies, besides that of the blade passage. In fact, at the highest frequencies we were able to resolve from the database of instantaneous realizations we produced, we found that the nonlinear component of sound was the highest even for the isolated propellers, as shown in figures 34 and 35 for the

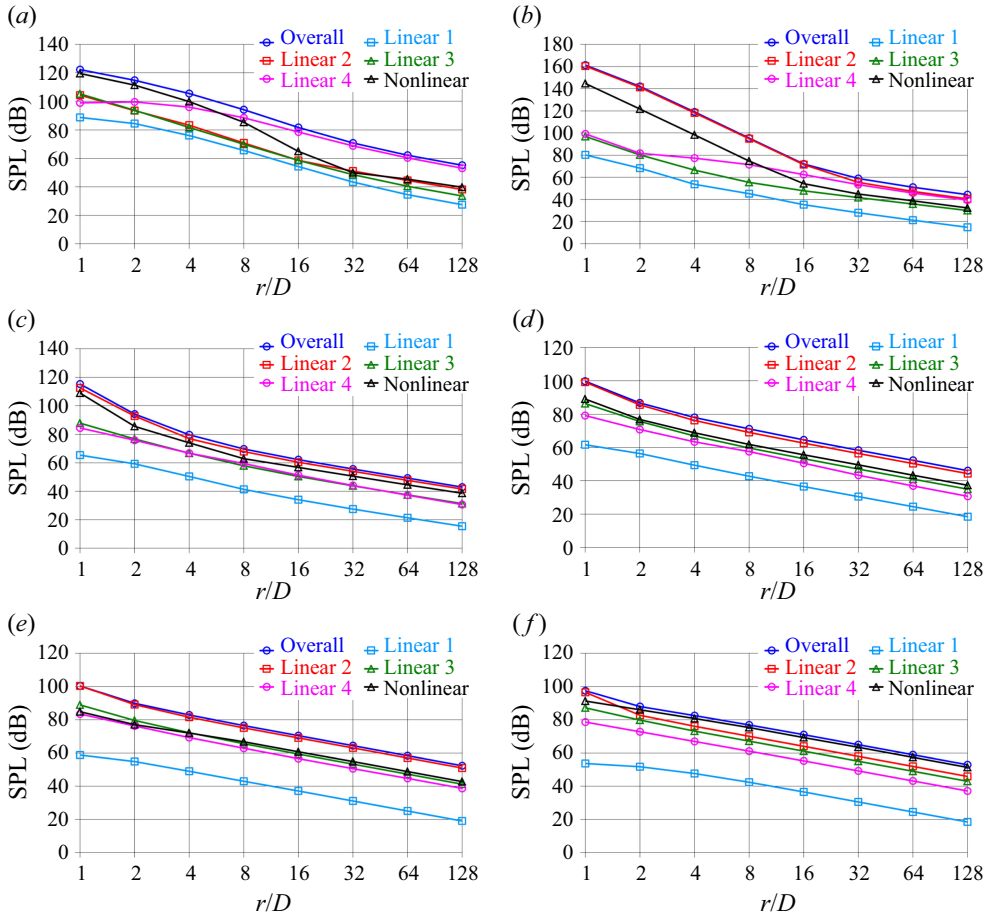


Figure 34. Radial evolution of the SPLs at the streamwise coordinate  $z/D = 0.3$  for the FRONT system in the third-octave bands centred at the frequencies (a)  $f/f_b = 1/3$ , (b)  $f/f_b = 1$ , (c)  $f/f_b = 2$ , (d)  $f/f_b = 5$ , (e)  $f/f_b = 10$  and (f)  $f/f_b = 30$ . Azimuthal averages across the 72 hydrophones placed at each radial coordinate. Note that the scale of the horizontal axis is logarithmic. Comparison across the SPLs from the upstream shaft (linear 1), the front propeller (linear 2), the rear dummy hub (linear 3), the downstream shaft (linear 4) and the wake flow (nonlinear).

frequency  $f = 30f_b$ , although the nonlinear sound from the CRP system is again well above that radiated from the two isolated propellers.

Figure 36 also displays the dependence of the nonlinear component of sound on the selected control volume. An additional control volume, CV1, was considered, smaller than the original one, CV0, reported in magenta in figure 5. Here CV1 has the same upstream boundary as CV0 ( $z/D = -2.5$ ), but a downstream boundary located more upstream, at the streamwise coordinate  $z/D = 2.0$ . The control volume CV2 was also selected, which is the complement of CV1, relative to CV0. This means that the upstream boundary of CV2 is placed at  $z/D = 2.0$ , while its downstream boundary is placed at  $z/D = 4.5$ , as for CV0. The results in figure 36 provide a comparison across nonlinear components of SPLs computed across CV0, CV1 and CV2 for the CRP system. Figure 36(a), dealing with the shaft frequency, even shows that the contribution of the downstream control volume CV2 becomes the leading one at intermediate distances from the propellers ( $r/D \approx 8.0$ ). This changes further away from them, but the signature of CV2 in the overall SPLs remains

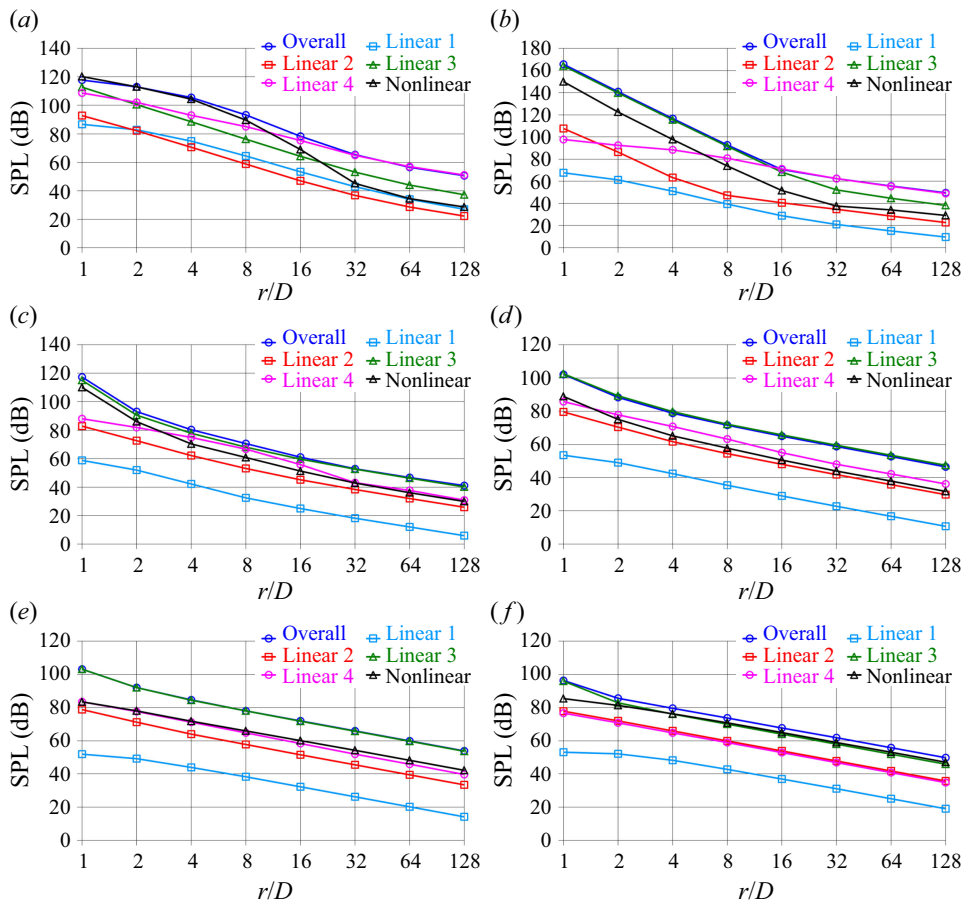


Figure 35. Radial evolution of the SPLs at the streamwise coordinate  $z/D=0.3$  for the REAR system in the third-octave bands centred at the frequencies (a)  $f/f_b=1/3$ , (b)  $f/f_b=1$ , (c)  $f/f_b=2$ , (d)  $f/f_b=5$ , (e)  $f/f_b=10$  and (f)  $f/f_b=30$ . Azimuthal averages across the 72 hydrophones placed at each radial coordinate. Note that the scale of the horizontal axis is logarithmic. Comparison across the SPLs from the upstream shaft (linear 1), the front dummy hub (linear 2), the rear propeller (linear 3), the downstream shaft (linear 4) and the wake flow (nonlinear).

non-negligible. At the blade frequency, considered in figure 36(b), the nonlinear sound from CV1 is initially dominant, but it becomes comparable to that from CV2 moving towards the acoustic far field. This behaviour is also observed at higher frequencies, but the levels of nonlinear sound from CV1 and CV2 achieve similar values at even closer radial distances from the propellers, as demonstrated by the other panels of figure 36. The results in figure 36 highlight the importance of including the downstream development of the wake flow for a proper reconstruction of the nonlinear sound. For limitation of space, the same results are not included for the isolated front and rear propellers, but they were verified similar to those shown in figure 36 in terms of dependence of the nonlinear sound on the size of the control volume.

It is also interesting to see in figure 33(b) a decrease of the negative slope, characterizing the radial decay of the nonlinear component of sound, which is reflected in the radial evolution of the overall SPLs in figure 32(b). This behaviour is investigated in more detail by means of figure 37. In this figure the SPLs tied to the three surface and

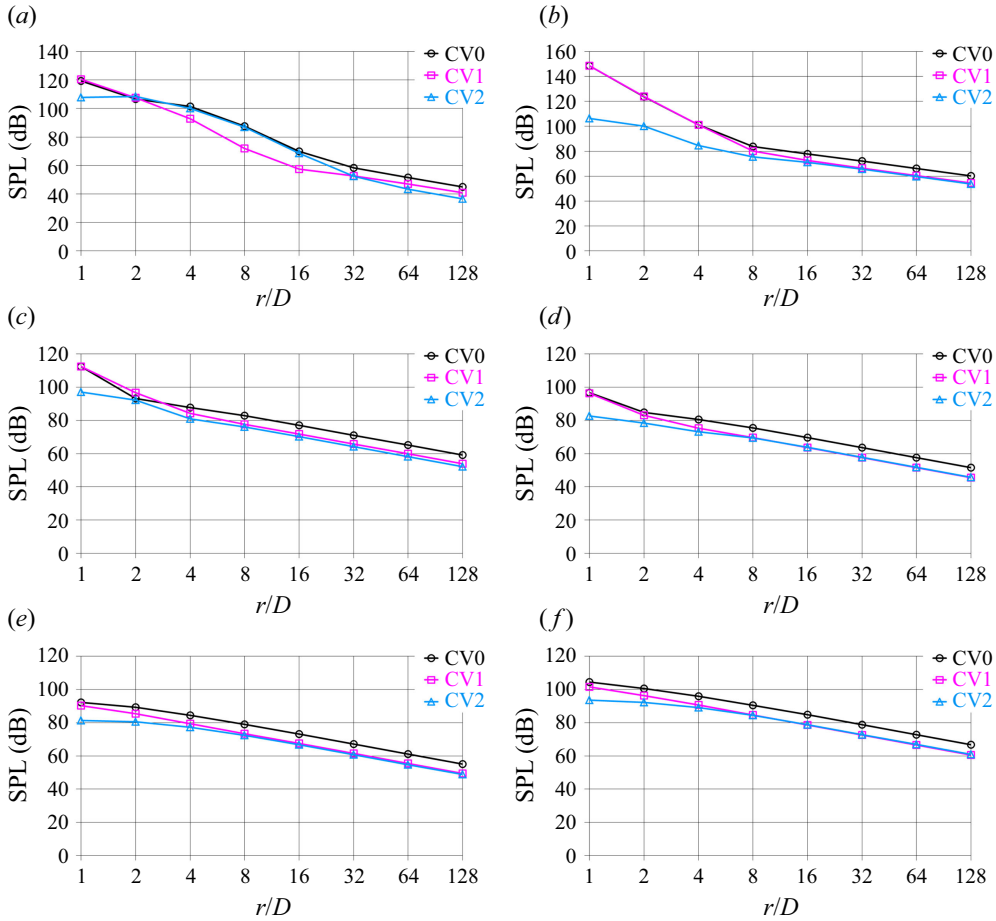


Figure 36. Radial evolution of the SPLs at the streamwise coordinate  $z/D = 0.3$  for the CRP system in the third-octave bands centred at the frequencies (a)  $f/f_b = 1/3$ , (b)  $f/f_b = 1$ , (c)  $f/f_b = 2$ , (d)  $f/f_b = 5$ , (e)  $f/f_b = 10$  and (f)  $f/f_b = 30$ . Azimuthal averages across the 72 hydrophones placed at each radial coordinate. Note that the scale of the horizontal axis is logarithmic. Comparison across the nonlinear components of sound computed over different control volumes: overall control volume CV0 of figure 5 ranging between  $-2.5 < z/D < 4.5$ , control volume CV1 ranging between  $-2.5 < z/D < 2.0$ , control volume CV2 ranging between  $2.0 < z/D < 4.5$ .

three volume integrals on the right-hand side of (2.6) are separated, to gain a better insight on their relative contribution to the overall acoustic signature. The front and rear components deal with the three surface integrals on the right-hand side of (2.6), computed on the Lagrangian grids representing the front and rear propellers, respectively. The three nonlinear components refer to the volume integrals on the right-hand side of (2.6). In figure 37, dealing with the CRP system, the main contributor to the acoustic signature at outer radial coordinates is represented by the first volume integral term, nonlinear 1, whose radial decay is slower compared with that of the other terms, which are the leading ones at inner radial coordinates. This is the case across all frequencies, but it is especially evident at the blade frequency: in figure 37(b), the nonlinear 1 term is the smallest one in the vicinity of the propulsion system, while it becomes the leading one at the outermost radial coordinates. These results also explain the decreasing radial decline of the SPLs at outer coordinates, observed in figure 33(b). In figure 37 it is also interesting to see that, moving

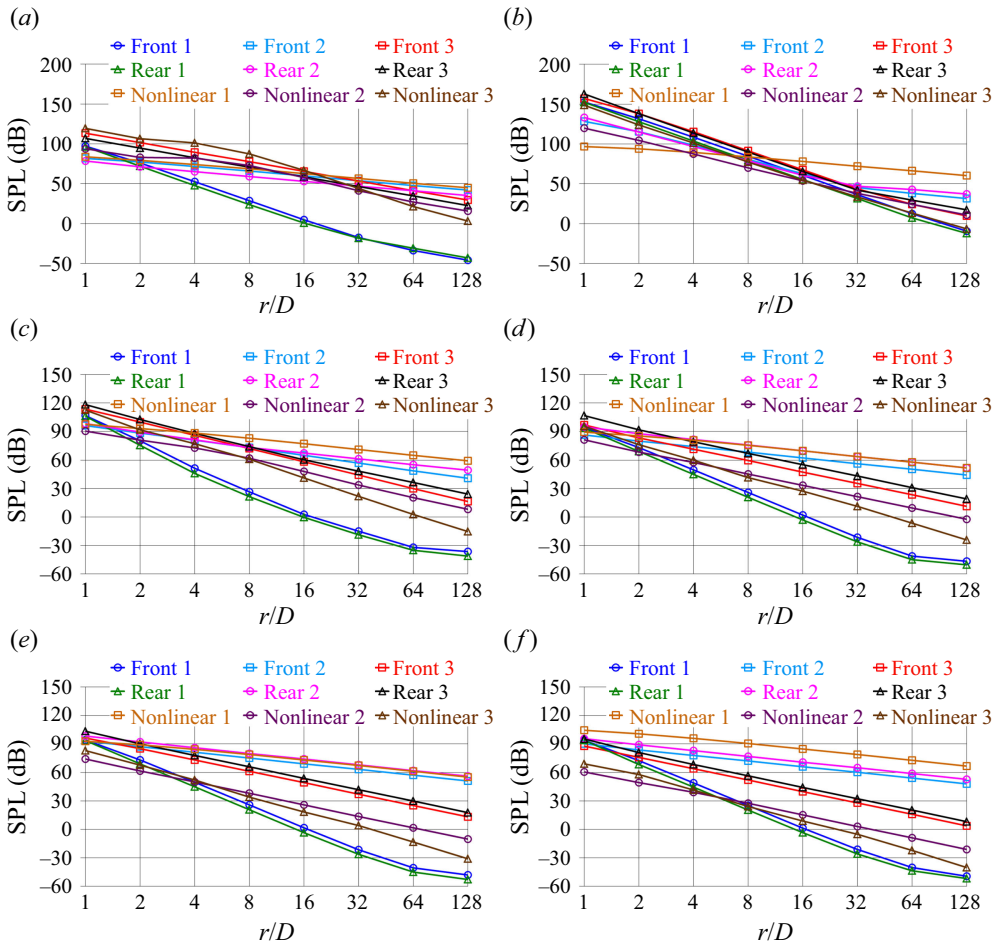


Figure 37. Radial evolution of the SPLs at the streamwise coordinate  $z/D=0.3$  for the CRP system in the third-octave bands centred at the frequencies (a)  $f/f_b = 1/3$ , (b)  $f/f_b = 1$ , (c)  $f/f_b = 2$ , (d)  $f/f_b = 5$ , (e)  $f/f_b = 10$  and (f)  $f/f_b = 30$ . Azimuthal averages across the 72 hydrophones placed at each radial coordinate. Note that the scale of the horizontal axis is logarithmic. Comparison across the SPLs from the acoustic sources at the right-hand side of (2.6): the front and rear terms standing for the three integrals computed on the surfaces of the front and rear propellers; the nonlinear terms standing for the three volume integrals. For clarity, the sound radiated from the surfaces of the upstream and downstream shafts is not included.

towards higher frequencies, the nonlinear 1 term becomes increasingly important at inner radial coordinates. For instance, in figure 37(f), dealing with the frequency  $f = 30f_b$ , it is the largest one across all radial coordinates. This explains the more uniform radial evolution of the SPLs at higher frequencies, observed in figure 32. In figures 38 and 39, concerning the isolated front and rear propellers, respectively, results differ, at least in the range of radial coordinates considered here. Also, for them the nonlinear 1 term declines at a slower rate than most of the other ones, with the exception of the linear terms front 2 and rear 2, respectively. Therefore, also in this case the relative importance of the nonlinear 1 term on the overall acoustic signature grows, moving away from the propellers, especially at the largest frequency. However, it does not become the leading one across all frequencies, in contrast with the results observed for the CRP system, since the nonlinear 1 term is smaller for the isolated propellers than for the contra-rotating ones. This is again

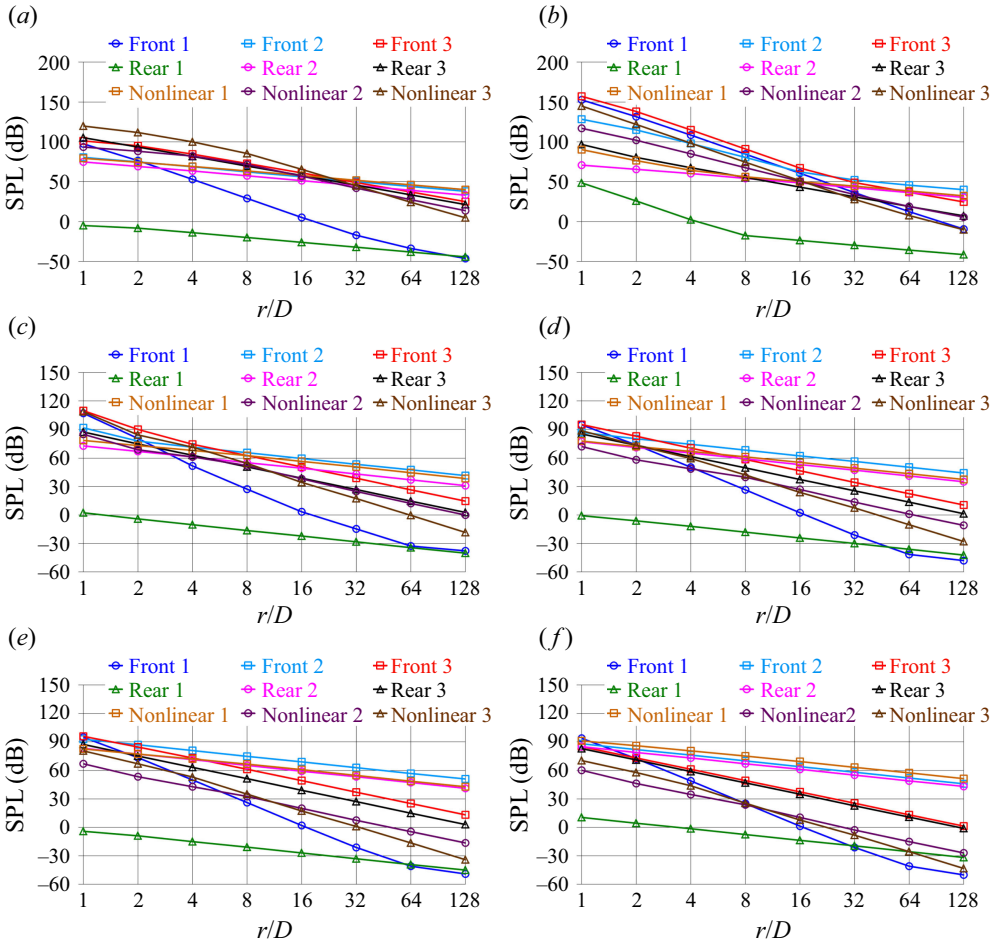


Figure 38. Radial evolution of the SPLs at the streamwise coordinate  $z/D = 0.3$  for the FRONT system in the third-octave bands centred at the frequencies (a)  $f/f_b = 1/3$ , (b)  $f/f_b = 1$ , (c)  $f/f_b = 2$ , (d)  $f/f_b = 5$ , (e)  $f/f_b = 10$  and (f)  $f/f_b = 30$ . Azimuthal averages across the 72 hydrophones placed at each radial coordinate. Note that the scale of the horizontal axis is logarithmic. Comparison across the SPLs from the acoustic sources at the right-hand side of (2.6): the front and rear terms standing for the three integrals computed on the surfaces of the front propeller and the rear dummy hub; the nonlinear terms standing for the three volume integrals. For clarity, the sound radiated from the surfaces of the upstream and downstream shafts is not included.

a result of the increased contribution to the overall acoustic signature from the wake flow downstream of the CRP system, in comparison with both FRONT and REAR cases.

### 6.7. Directivity of the nonlinear component of sound

Details on the directivity of the three nonlinear components of sound are given in figure 40, where polar plots are reported on the plane  $z/D = 0.0$  at a distance from the CRP system equivalent to  $8D$ . Overall, the distribution of the global nonlinear sound (black bullets in figure 40) is rather uniform, which is especially attributable to the nonlinear 1 component. This result is reinforced moving from the lowest to the highest frequencies: at  $f/f_b = 1/3$  the dominant nonlinear sound is due to the nonlinear 3 component, but this is already not the case at the blade frequency in figure 40(b). As one moves away from

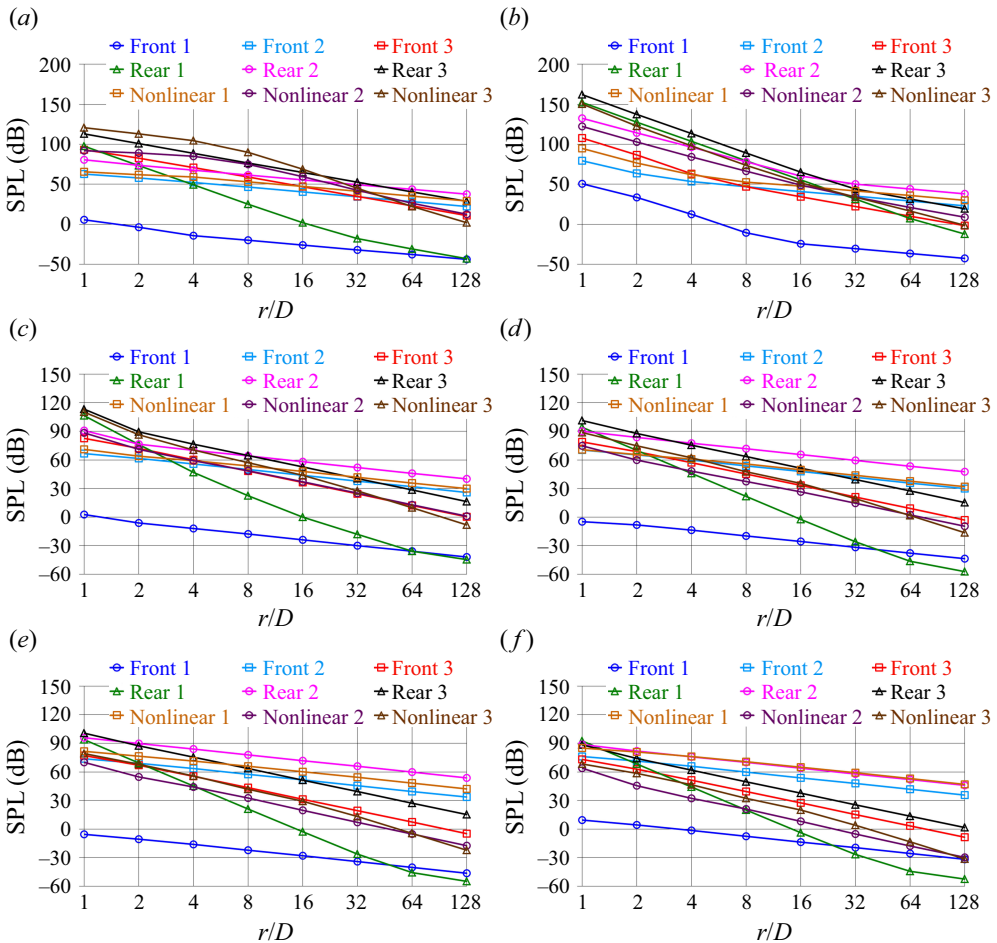


Figure 39. Radial evolution of the SPLs at the streamwise coordinate  $z/D=0.3$  for the REAR system in the third-octave bands centred at the frequencies (a)  $f/f_b = 1/3$ , (b)  $f/f_b = 1$ , (c)  $f/f_b = 2$ , (d)  $f/f_b = 5$ , (e)  $f/f_b = 10$  and (f)  $f/f_b = 30$ . Azimuthal averages across the 72 hydrophones placed at each radial coordinate. Note that the scale of the horizontal axis is logarithmic. Comparison across the SPLs from the acoustic sources at the right-hand side of (2.6): the front and rear terms standing for the three integrals computed on the surfaces of the front dummy hub and the rear propeller; the nonlinear terms standing for the three volume integrals. For clarity, the sound radiated from the surfaces of the upstream and downstream shafts is not included.

the CRP system, the directivity of the nonlinear sound reduces further, due to the slower decline of the nonlinear 1 component, which is the one characterized by the most uniform polar distribution. This is shown at a distance from the propellers equivalent to  $128D$  in figure 41.

The directivity of the nonlinear sound is more evident in the polar plots of figure 42, dealing with the plane of equation  $y/D = 0.0$ . Hydrophones at a distance from the CRP system equivalent to  $8D$  are again considered. Higher SPLs are achieved in the downstream direction (corresponding to the polar angle at  $0^\circ$ ), especially by the nonlinear 3 component. At the lowest frequencies this affects the overall nonlinear sound, which is still dominated by the nonlinear 3 component. However, also in this plane at the highest frequencies the nonlinear 1 component, which displays a much weaker dependence on the polar coordinate, becomes the leading one. Therefore, although both the nonlinear 2



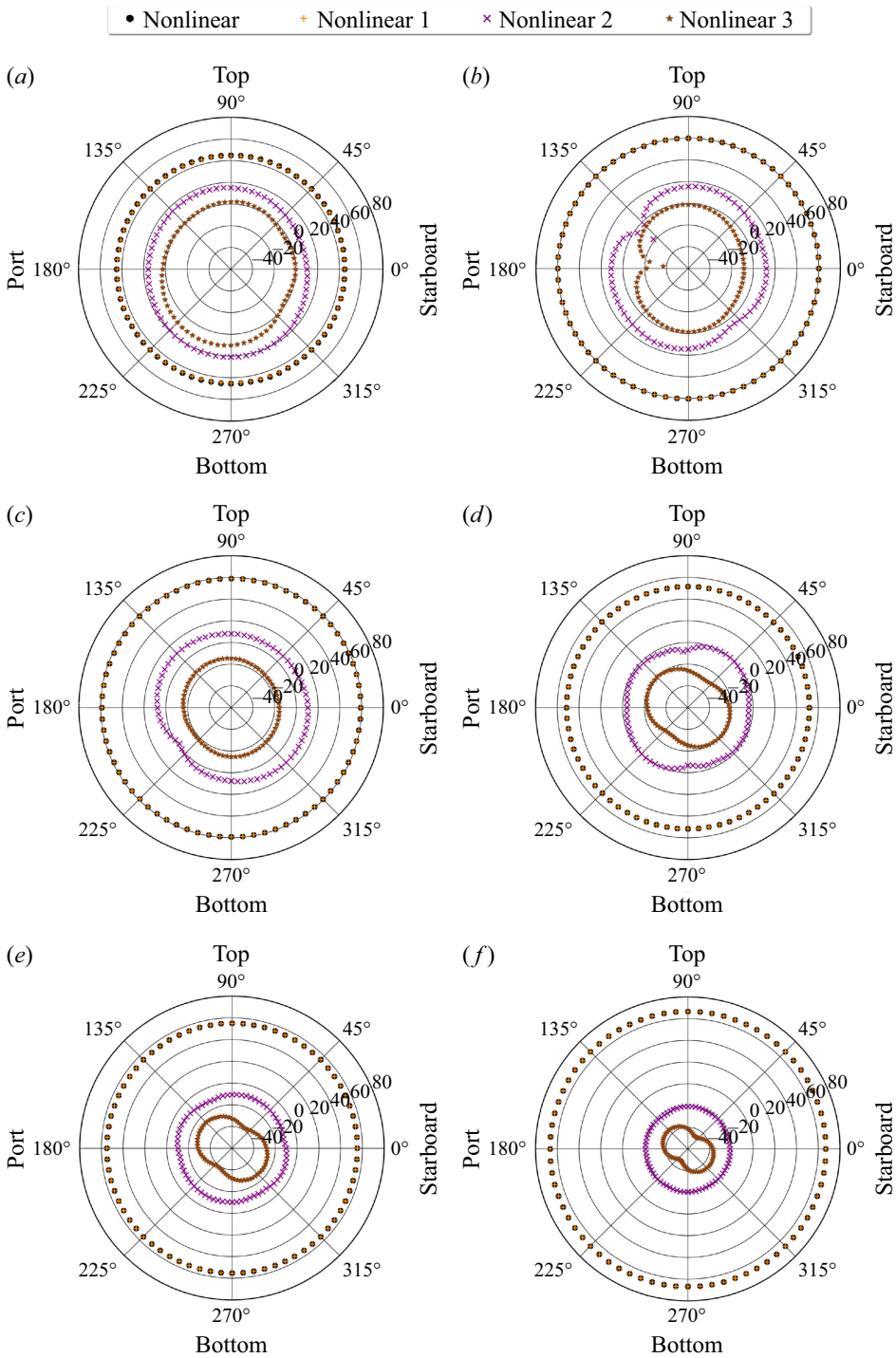


Figure 41. Polar plots of SPLs on the plane  $z/D = 0.0$  at a distance from the CRP system equal to  $128D$  in the third-octave bands centred at the frequencies (a)  $f/f_b = 1/3$ , (b)  $f/f_b = 1$ , (c)  $f/f_b = 2$ , (d)  $f/f_b = 5$ , (e)  $f/f_b = 10$  and (f)  $f/f_b = 30$ . Comparison across the nonlinear components of the acoustic signature.

• Nonlinear + Nonlinear 1 × Nonlinear 2 \* Nonlinear 3

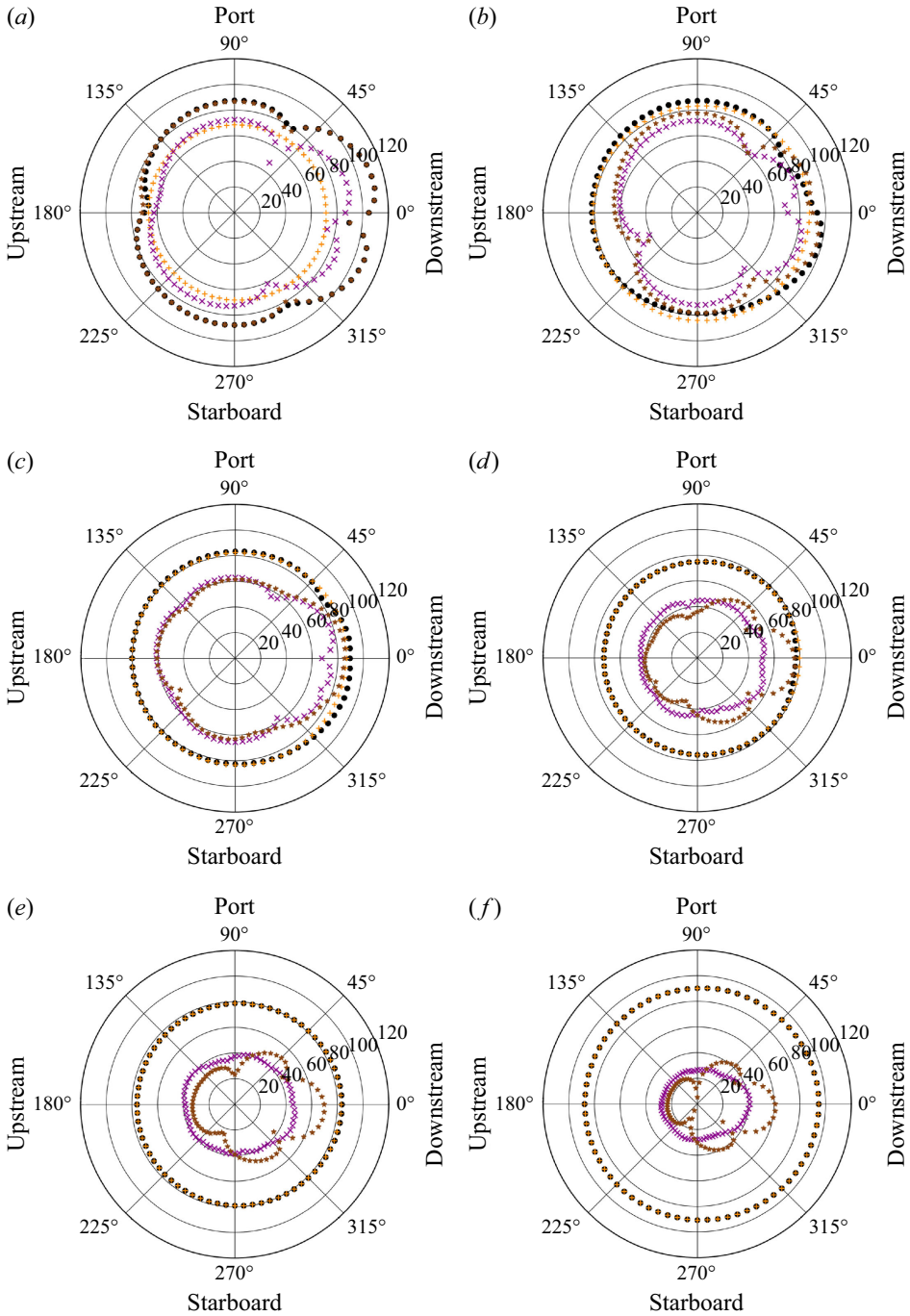


Figure 42. Polar plots of SPLs on the plane  $y/D = 0.0$  at a distance from the CRP system equal to  $8D$  in the third-octave bands centred at the frequencies (a)  $f/f_b = 1/3$ , (b)  $f/f_b = 1$ , (c)  $f/f_b = 2$ , (d)  $f/f_b = 5$ , (e)  $f/f_b = 10$  and (f)  $f/f_b = 30$ . Comparison across the nonlinear components of the acoustic signature.

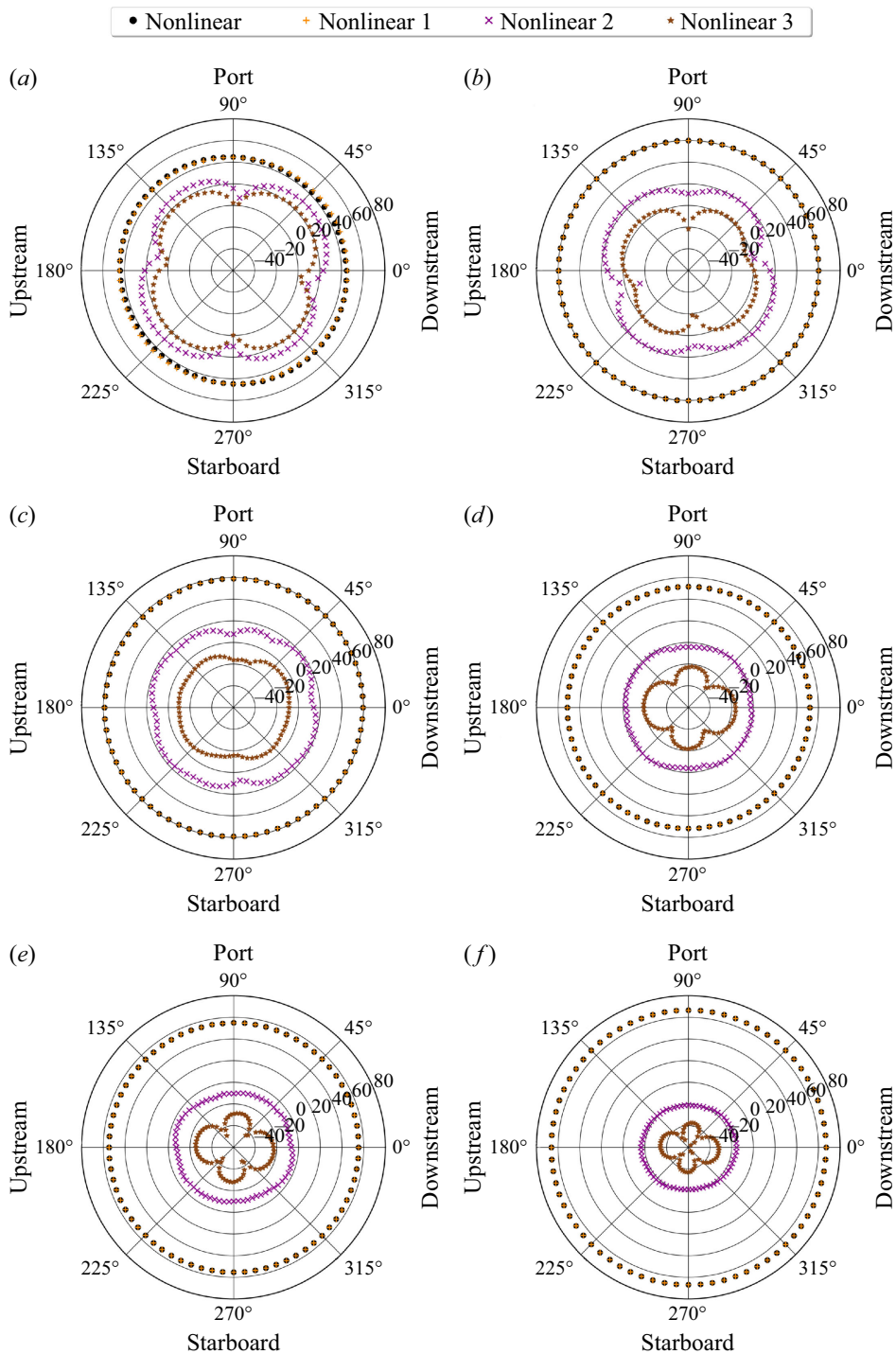


Figure 43. Polar plots of SPLs on the plane  $y/D = 0.0$  at a distance from the CRP system equal to  $128D$  in the third-octave bands centred at the frequencies (a)  $f/f_b = 1/3$ , (b)  $f/f_b = 1$ , (c)  $f/f_b = 2$ , (d)  $f/f_b = 5$ , (e)  $f/f_b = 10$  and (f)  $f/f_b = 30$ . Comparison across the nonlinear components of the acoustic signature.

and nonlinear 3 components show higher levels in the downstream direction across all panels of [figure 42](#), for frequencies higher than  $f_b$  the polar distribution of the overall nonlinear sound, dominated by the nonlinear 1 component, is almost uniform. Also in the plane  $y/D = 0.0$  the directivity of the overall nonlinear sound declines at locations further away from the propellers, as demonstrated at a distance equivalent to  $128D$  in [figure 43](#). This is again the result of the nonlinear 1 component becoming the dominant one across the whole range of frequencies: while the nonlinear 3 component is still a function of the polar coordinate, the nonlinear 1 component is again almost uniform in the polar plots of [figure 43](#).

## 7. Conclusions

In this study, results of high-fidelity computations, conducted on a cylindrical grid of 4.6 billion points and using a LES approach, were utilized to reconstruct in post-processing the acoustic signature of a contra-rotating propulsion system working in wetted conditions, based on the FWH acoustic analogy. Comparisons were also reported against the acoustic emission of the two propellers of the system, working alone, as a reference useful to isolate the effect of their interaction on the levels of sound.

In their vicinity, the sound from the contra-rotating propellers at small frequencies was not substantially modified, compared with that from the isolated front and rear propellers. This was not the case at higher frequencies, especially moving towards downstream coordinates, where the acoustic signature was reinforced. This was due to the nonlinear component of sound, originating from vorticity and turbulence of the wake. Isolated vortex rings were generated downstream of the contra-rotating system, in contrast with the typical helical vortices shed by the two propellers working alone. The increased complexity of the wake of the contra-rotating system and its faster instability, as a result of the shear between the tip vortices shed by the front and rear propellers, respectively, were able to reinforce the nonlinear component of sound, becoming the leading one at downstream coordinates. This phenomenon was found to affect more the highest frequencies of the acoustic signature, propagating downstream to lower frequencies as the wake instability developed.

The radial evolution was also modified by the interaction of the two propellers of the contra-rotating system. The rate of decay of sound was slower, compared with the isolated propellers. This result was found attributable again to the nonlinear component, which was higher from the contra-rotating propellers than from the isolated ones. While in the vicinity of the propellers the acoustic signature was dominated by the linear component radiated from the surface of their blades, which was similar between propellers operating together and in isolation, especially at low frequencies, this was increasingly not the case anymore at outer radial coordinates. In the case of the isolated propellers the sound was still dominated by its linear component, while away from the contra-rotating propellers the nonlinear sound became the most significant, due to its higher levels and its slower radial decay. These higher levels of sound from the contra-rotating system, compared with the isolated propellers, were found to affect more the highest frequencies, even at small radial coordinates, propagating towards lower frequencies for increasing radial distances.

The results of this study were unexpected. They show that the nonlinear component of sound, which is usually assumed negligible moving away from marine propellers, achieves higher values in the case of a contra-rotating system, compared with propellers working alone, and experiences a slower radial decay, compared with the linear component. This makes the nonlinear sound significant even at large distances from contra-rotating propellers, which is a result of the more complex wake dynamics, compared with propulsion systems consisting of isolated propellers. This implies that taking into account

the nonlinear component of sound is even more important for contra-rotating propellers than for more conventional propellers, even away from the acoustic near field and in wetted conditions. We should note that the contra-rotating and isolated propellers were all simulated at the same advance coefficient with the purpose of producing tip vortices of similar intensities and analysing the effect of their interaction in the wake of the contra-rotating system as well as the changes affecting the relative importance of the linear and nonlinear components of the acoustic signature. Therefore, although the radiated sound from the contra-rotating propellers was found stronger than that from the propellers working alone, especially because of the contribution tied to the nonlinear component, it should be acknowledged that in the present study the contra-rotating system was generating a larger thrust, compared with the isolated propellers, given by the action of the two propellers composing the system. Therefore, it may be the case that the contra-rotating system is less noisy than the isolated propellers, when producing the same overall thrust. In one of our earlier studies on marine propellers (Posa & Broglia 2023) we verified indeed a strong, roughly logarithmic dependence of the radiated sound on the advance coefficient. It may be of interest in the framework of our future studies to adjust (reduce) the advance coefficient of the isolated propellers, in order for them to produce the same thrust as the contra-rotating system and to compare the intensity of the sound levels in such conditions.

**Acknowledgements.** We acknowledge EuroHPC Joint Undertaking for awarding the project EHPC-REG-2023R01-066 access to MeluXina CPU at LuxProvide (Luxembourg) in the framework of a Regular Access call.

**Declaration of interests.** The authors report no conflict of interest.

#### REFERENCES

- ABBASI, A.A., FRANZOSI, G., CANEPA, E., GAGGERO, S., VILLA, D., VIVIANI, M. & TANI, G. 2023 Experimental analysis of the flow field around a propeller with inclined shaft. *Ocean Engng* **285**, 115237.
- AHMED, S., CROAKER, P. & DOOLAN, C.J. 2020 On the instability mechanisms of ship propeller wakes. *Ocean Engng* **213**, 107609.
- AKKERMANS, R.A.D., STUERMER, A. & DELFS, J.W. 2016 Active flow control for interaction noise reduction of contra-rotating open rotors. *AIAA J.* **54** (4), 1413–1423.
- ALVES PEREIRA, F., CAPONE, A. & DI FELICE, F. 2021 Flow field and vortex interactions in the near wake of two counter-rotating propellers. *Appl. Ocean Res.* **117**, 102918.
- ARDAVAN, H. 1991 The breakdown of the linearized theory and the role of quadrupole sources in transonic rotor acoustics. *J. Fluid Mech.* **226**, 591–624.
- BAEK, D.-G., YOON, H.-S., JUNG, J.-H., KIM, K.-S. & PAIK, B.-G. 2015 Effects of the advance ratio on the evolution of a propeller wake. *Comput. Fluids* **118**, 32–43.
- BALARAS, E. 2004 Modeling complex boundaries using an external force field on fixed Cartesian grids in large-eddy simulations. *Comput. Fluids* **33** (3), 375–404.
- BALARAS, E., SCHROEDER, S. & POSA, A. 2015 Large-eddy simulations of submarine propellers. *J. Ship Res.* **59** (4), 227–237.
- BLANDEAU, V.P. & JOSEPH, P.F. 2010 Broadband noise due to rotor-wake/rotor interaction in contra-rotating open rotors. *AIAA J.* **48** (11), 2674–2686.
- BRENTNER, K.S. & FARASSAT, F. 2003 Modeling aerodynamically generated sound of helicopter rotors. *Prog. Aerosp. Sci.* **39** (2-3), 83–120.
- CAPONE, A. & ALVES PEREIRA, F. 2020 Unraveling the interplay of two counter-rotating helical vortices. *Phys. Rev. Fluids* **5** (11), 110509.
- CAPONE, A., DI FELICE, F. & ALVES PEREIRA, F. 2021 On the flow field induced by two counter-rotating propellers at varying load conditions. *Ocean Engng* **221**, 108322.
- CASAGRANDE HIRONO, F., ROBERTSON, J. & TORIJA MARTINEZ, A.J. 2024 Acoustic and psychoacoustic characterisation of small-scale contra-rotating propellers. *J. Sound Vib.* **569**, 117971.
- CHAHOURI, A., ELOUAHMANI, N. & OUCHENE, H. 2022 Recent progress in marine noise pollution: a thorough review. *Chemosphere* **291**, 132983.
- CHAITANYA, P., JOSEPH, P., PRIOR, S.D. & PARRY, A.B. 2022 On the optimum separation distance for minimum noise of contra-rotating rotors. *J. Sound Vib.* **535**, 117032.

- CHANG, B.-J. & GO, S. 2011 Study on a procedure for propulsive performance prediction for CRP-POD systems. *J. Mar. Sci. Technol.* **16** (1), 1–7.
- CHEN, W., MA, Z., SPIESER, E., GUO, J., ZHOU, P., ZHONG, S., ZHANG, X. & HUANG, X. 2023 Acoustic imaging of the broadband noise arising in contra-rotating co-axial propellers. *Aerosp. Sci. Technol.* **141**, 108531.
- CIANFERRA, M. & ARMENIO, V. 2021 Scaling properties of the Ffowcs–Williams and Hawkings equation for complex acoustic source close to a free surface. *J. Fluid Mech.* **927**, A2.
- CIANFERRA, M., ARMENIO, V. & IANNIELLO, S. 2018 Hydroacoustic noise from different geometries. *Intl J. Heat Fluid Flow* **70**, 348–362.
- CIANFERRA, M., IANNIELLO, S. & ARMENIO, V. 2019a Assessment of methodologies for the solution of the Ffowcs Williams and Hawkings equation using LES of incompressible single-phase flow around a finite-size square cylinder. *J. Sound Vib.* **453**, 1–24.
- CIANFERRA, M., PETRONIO, A. & ARMENIO, V. 2019b Non-linear noise from a ship propeller in open sea condition. *Ocean Engng* **191**, 106474.
- DI FRANCESCANTONIO, P. 1997 A new boundary integral formulation for the prediction of sound radiation. *J. Sound Vib.* **202** (4), 491–509.
- ENVIA, E. 1994 Asymptotic theory of supersonic propeller noise. *AIAA J.* **32** (2), 239–246.
- FARASSAT, F. & BRENTNER, K.S. 1998a Supersonic quadrupole noise theory for high-speed helicopter rotors. *J. Sound Vib.* **218** (3), 481–500.
- FARASSAT, F. & BRENTNER, K.S. 1998b The acoustic analogy and the prediction of the noise of rotating blades. *Theor. Comput. Fluid Dyn.* **10** (1–4), 155–170.
- FELLI, M., CAMUSSI, R. & DI FELICE, F. 2011 Mechanisms of evolution of the propeller wake in the transition and far fields. *J. Fluid Mech.* **682**, 5–53.
- FELLI, M., DI FELICE, F., GUJ, G. & CAMUSSI, R. 2006 Analysis of the propeller wake evolution by pressure and velocity phase measurements. *Exp. Fluids* **41** (3), 441–451.
- FELLI, M. & FALCHI, M. 2018 A parametric survey of propeller wake instability mechanisms by detailed flow measurement and time resolved visualizations. In *Proceedings of the 32nd Symposium on Naval Hydrodynamics, 5–10 August 2018, Hamburg, Germany*, paper number 110. U.S. Office of Naval Research and Hamburg University of Technology.
- FELLI, M., FALCHI, M. & DUBBIOSO, G. 2015 Experimental approaches for the diagnostics of hydroacoustic problems in naval propulsion. *Ocean Engng* **106**, 1–19.
- FELLI, M., GUJ, G. & CAMUSSI, R. 2008 Effect of the number of blades on propeller wake evolution. *Exp. Fluids* **44** (3), 409–418.
- FFOWCS WILLIAMS, J.E. & HAWKINGS, D.L. 1969 Sound generation by turbulence and surfaces in arbitrary motion. *Phil. Trans. R. Soc. Lond. A Math. Phys. Sci.* **264** (1151), 321–342.
- GLEGG, S. & DEVENPORT, W. 2017 *Aeroacoustics of Low Mach Number Flows: Fundamentals, Analysis, and Measurement*. Academic Press.
- GRASSI, D., BRIZZOLARA, S., VIVIANI, M., SAVIO, L. & CAVIGLIA, S. 2010 Design and analysis of counter-rotating propellers-comparison of numerical and experimental results. *J. Hydrodyn.* **22** (5), 570–576.
- HANSON, D.B. 1985 Noise of counter-rotation propellers. *J. Aircraft* **22** (7), 609–617.
- HANSON, D.B. & FINK, M.R. 1979 The importance of quadrupole sources in prediction of transonic tip speed propeller noise. *J. Sound Vib.* **62** (1), 19–38.
- HOU, L., YIN, L., HU, A., CHANG, X., LIN, Y. & WANG, S. 2021 Optimal matching investigation of marine contra-rotating propellers for energy consumption minimization. *J. Mar. Sci. Technol. (Japan)* **26** (4), 1184–1197.
- HU, J., NING, X., ZHAO, W., LI, F., MA, J., ZHANG, W., SUN, S., ZOU, M. & LIN, C. 2021 Numerical simulation of the cavitating noise of contra-rotating propellers based on detached eddy simulation and the Ffowcs Williams–Hawkings acoustics equation. *Phys. Fluids* **33** (11), 115117.
- HU, J., WANG, Y., ZHANG, W., CHANG, X. & ZHAO, W. 2019 Tip vortex prediction for contra-rotating propeller using large eddy simulation. *Ocean Engng* **194**, 106410.
- HUANG, Y.-S., DONG, X.-Q., YANG, C.-J., LI, W. & NOBLESSE, F. 2019 Design of wake-adapted contra-rotating propellers for high-speed underwater vehicles. *Appl. Ocean Res.* **91**, 101880.
- IANNIELLO, S. 1999 Quadrupole noise predictions through the Ffowcs Williams–Hawkings equation. *AIAA J.* **37** (9), 1048–1054.
- IANNIELLO, S. 2001 Aeroacoustic analysis of high tip-speed rotating blades. *Aerosp. Sci. Technol.* **5** (3), 179–192.
- JEONG, J. & HUSSAIN, F. 1995 On the identification of a vortex. *J. Fluid Mech.* **285**, 69–94.
- KAN, K., LI, H. & YANG, Z. 2023 Large eddy simulation of turbulent wake flow around a marine propeller under the influence of incident waves. *Phys. Fluids* **35** (5), 055124.

- KERWIN, J.E. 1986 Marine propellers. *Annu. Rev. Fluid Mech.* **18** (1), 367–403.
- KHAN, M.R., KUNDU, R., RAHMAN, W., HAQUE, M.M. & ULLAH, M.R. 2018 Efficiency study: Contra-rotating propeller system. *AIP Conf. Proc.* **1980**, 060001.
- KIMMERL, J., MERTES, P. & ABDEL-MAKSOU, M. 2021 Application of large eddy simulation to predict underwater noise of marine propulsors. Part 2: Noise generation. *J. Mar. Sci. Engng* **9** (7), 778.
- KINGAN, M.J. & PARRY, A.B. 2019 Acoustic theory of the many-bladed contra-rotating propeller: analysis of the effects of blade sweep on wake interaction noise. *J. Fluid Mech.* **868**, 385–427.
- KINGAN, M.J. & PARRY, A.B. 2020a Acoustic theory of the many-bladed contra-rotating propeller: the effects of sweep on noise enhancement and reduction. *J. Sound Vib.* **468**, 115089.
- KINGAN, M.J. & PARRY, A.B. 2020b Time-domain analysis of contra-rotating propeller noise: wake interaction with a downstream propeller blade. *J. Fluid Mech.* **901**, A21.
- KU, G., CHO, J., CHEONG, C. & SEOL, H. 2021 Numerical investigation of tip-vortex cavitation noise of submarine propellers using hybrid computational hydro-acoustic approach. *Ocean Engng* **238**, 109693.
- KUMAR, P. & MAHESH, K. 2017 Large eddy simulation of propeller wake instabilities. *J. Fluid Mech.* **814**, 361–396.
- LIDTKE, A.K., HUMPHREY, V.F. & TURNOCK, S.R. 2016 Feasibility study into a computational approach for marine propeller noise and cavitation modelling. *Ocean Engng* **120**, 152–159.
- LIDTKE, A.K., LOYD, T., LAFEVER, F.H. & BOSSCHERS, J. 2022 Predicting cavitating propeller noise in off-design conditions using scale-resolving CFD simulations. *Ocean Engng* **254**, 111176.
- LIEFVENDAHL, M. 2010 Investigation of propeller wake instability using LES. *Ship Technol. Res.* **57** (2), 100–106.
- LIGHTHILL, M.J. 1952 On sound generated aerodynamically I. General theory. *Proc. R. Soc. Lond. A* **211** (1107) 564–587.
- LOWSON, M.V. 1965 The sound field for singularities in motion. *Proc. R. Soc. Lond. A* **286** (1407), 559–572.
- MCKAY, R.S., KINGAN, M.J., GO, S.T. & JUNG, R. 2021 Experimental and analytical investigation of contra-rotating multi-rotor UAV propeller noise. *Appl. Acoust.* **177**, 107850.
- MIN, K.-S., CHANG, B.-J. & SEO, H.-W. 2009 Study on the contra-rotating propeller system design and full-scale performance prediction method. *Intl. J. Nav. Archit. Ocean Engng* **1** (1), 29–38.
- NICOUD, F. & DUCROS, F. 1999 Subgrid-scale stress modelling based on the square of the velocity gradient tensor. *Flow Turbul. Combust.* **62** (3), 183–200.
- NOURI, N.M., MOHAMMADI, S. & ZAREZADEH, M. 2018 Optimization of a marine contra-rotating propellers set. *Ocean Engng* **167**, 397–404.
- ÖZDEN, M.C., GÜRKAN, A.Y., ÖZDEN, Y.A., CANYURT, T.G. & KORKUT, E. 2016 Underwater radiated noise prediction for a submarine propeller in different flow conditions. *Ocean Engng* **126**, 488–500.
- PAIK, K.-J., HWANG, S., JUNG, J., LEE, T., LEE, Y.-Y., AHN, H. & VAN, S.-H. 2015 Investigation on the wake evolution of contra-rotating propeller using RANS computation and SPIV measurement. *Intl. J. Nav. Archit. Ocean Engng* **7** (3), 595–609.
- PARRY, A.B. & KINGAN, M.J. 2019 Acoustic theory of the many-bladed contra-rotating propeller: physics of the wake interaction noise critical sources. *J. Fluid Mech.* **880**, R1.
- PARRY, A.B. & KINGAN, M.J. 2021 Acoustic theory of the many-bladed contra-rotating propeller: the event line and the precession of the interaction source. *J. Fluid Mech.* **909**, R1.
- PEAKE, N. & CRIGHTON, D.G. 1991 Lighthill quadrupole radiation in supersonic propeller acoustics. *J. Fluid Mech.* **223**, 363–382.
- POSA, A. 2022 Tip vortices shed by a hydrofoil in the wake of a marine propeller. *Phys. Fluids* **34** (12), 125134.
- POSA, A. 2023a Anisotropy of turbulence at the core of the tip and hub vortices shed by a marine propeller. *J. Fluid Mech.* **969**, A23.
- POSA, A. 2023b End effects in the wake of a hydrofoil working downstream of a propeller. *Phys. Fluids* **35** (4), 045122.
- POSA, A. & BROGLIA, R. 2022a Influence by the hub vortex on the instability of the tip vortices shed by propellers with and without winglets. *Phys. Fluids* **34** (11), 115115.
- POSA, A. & BROGLIA, R. 2022b Spanwise distribution of the loads on a hydrofoil working in the wake of an upstream propeller. *Ocean Engng* **264**, 112542.
- POSA, A. & BROGLIA, R. 2023 Influence of the load conditions on the acoustic signature of a tip-loaded propeller with winglets. *Phys. Fluids* **35** (4), 045147.
- POSA, A., BROGLIA, R. & BALARAS, E. 2022a The dynamics of the tip and hub vortices shed by a propeller: Eulerian and Lagrangian approaches. *Comput. Fluids* **236**, 105313.
- POSA, A., BROGLIA, R. & FELLI, M. 2022b Acoustic signature of a propeller operating upstream of a hydrofoil. *Phys. Fluids* **34** (6), 065132.

- POSA, A., BROGLIA, R., FELLI, M., CIANFERRA, M. & ARMENIO, V. 2022c Hydroacoustic analysis of a marine propeller using large-eddy simulation and acoustic analogy. *J. Fluid Mech.* **947**, A46.
- POSA, A., BROGLIA, R., FELLI, M., FALCHI, M. & BALARAS, E. 2019 Characterization of the wake of a submarine propeller via large-eddy simulation. *Comput. Fluids* **184**, 138–152.
- POSA, A., CAPONE, A., ALVES PEREIRA, F., DI FELICE, F. & BROGLIA, R. 2024 Interaction between the helical vortices shed by contra-rotating propellers. *Phys. Fluids* **36** (5), 055116.
- POSA, A., FELLI, M. & BROGLIA, R. 2022d Influence of an upstream hydrofoil on the acoustic signature of a propeller. *Phys. Fluids* **34** (4), 045112.
- POSA, A., FELLI, M. & BROGLIA, R. 2022e The signature of a propeller–rudder system: acoustic analogy based on LES data. *Ocean Engng* **259**, 112059.
- POWELL, A. 1964 Theory of vortex sound. *J. Acoust. Soc. Am.* **36** (1), 177–195.
- ROSSI, T. & TOIVANEN, J. 1999 Parallel fast direct solver for block tridiagonal systems with separable matrices of arbitrary dimension. *SIAM J. Sci. Comput.* **20** (5), 1778–1793.
- SEZEN, S. & ATLAR, M. 2023 Marine propeller underwater radiated noise prediction with the FWH acoustic analogy Part 1: Assessment of model scale propeller hydroacoustic performance under uniform and inclined flow conditions. *Ocean Engng* **279**, 114552.
- SEZEN, S., ATLAR, M. & FITZSIMMONS, P. 2021a Prediction of cavitating propeller underwater radiated noise using RANS & DES-based hybrid method. *Ships Offshore Struct.* **16** (S1), 93–105.
- SEZEN, S., COSGUN, T., YURTSEVEN, A. & ATLAR, M. 2021b Numerical investigation of marine propeller underwater radiated noise using acoustic analogy Part 2: The influence of eddy viscosity turbulence models. *Ocean Engng* **220**, 108353.
- SMITH, D.A., FILIPPONE, A. & BARAKOS, G.N. 2022 Noise source analysis in counter-rotating open rotors. *AIAA J.* **60** (3), 1783–1796.
- SMITH, T.A. & RIGBY, J. 2022 Underwater radiated noise from marine vessels: a review of noise reduction methods and technology. *Ocean Engng* **266**, 112863.
- STARK, C. & SHI, W. 2021 Hydroacoustic and hydrodynamic investigation of bio-inspired leading-edge tubercles on marine-ducted thrusters. *R. Soc. Open Sci.* **8** (9), 210402.
- STELLA, A., GUJ, G., DI FELICE, F. & ELEFANTE, M. 2000 Experimental investigation of propeller wake evolution by means of LDV and flow visualizations. *J. Ship Res.* **44** (3), 155–169.
- SU, Y. & KINNAS, S.A. 2017 A BEM/RANS interactive method for predicting contra-rotating propeller performance. *Ocean Syst. Engng* **7** (4), 329–344.
- SU, Y., KINNAS, S.A. & JUKOLA, H. 2017 Application of a BEM/RANS interactive method to contra-rotating propellers. In *Proceedings of the Fifth International Symposium on Marine Propulsion, Espoo, Finland*. VTT Technical Research Centre of Finland, pp. 637–643.
- TADROS, M., VENTURA, M. & GUEDES SOARES, C. 2022 Towards fuel consumption reduction based on the optimum contra-rotating propeller. *J. Mar. Sci. Engng* **10** (11), 1657.
- TAGHADDOSI, F. & AGARWAL, R.K. 2000 Quadrupole modeling for prediction of high-speed impulsive noise of propellers. In *6th Aeroacoustics Conference and Exhibit, 12–14 June 2000, Lahaina, HI, USA*, American Institute of Aeronautics and Astronautics, pp. 2089.
- VAKILI, S., ÖLÇER, A.I. & BALLINI, F. 2021 The development of a transdisciplinary policy framework for shipping companies to mitigate underwater noise pollution from commercial vessels. *Mar. Pollut. Bull.* **171**, 112687.
- VAN KAN, J. 1986 A second-order accurate pressure-correction scheme for viscous incompressible flow. *SIAM J. Sci. Stat. Comput.* **7** (3), 870–891.
- VIITANEN, V.M., HYNINEN, A., SIPILÄ, T. & SIIKONEN, T. 2018 DDES of wetted and cavitating marine propeller for CHA underwater noise assessment. *J. Mar. Sci. Engng* **6** (2), 56.
- VILLA, D., GAGGERO, S., TANI, G. & VIVIANI, M. 2020 Numerical and experimental comparison of ducted and non-ducted propellers. *J. Mar. Sci. Engng* **8** (4), 257.
- WANG, C., LI, P., GUO, C., WANG, L. & SUN, S. 2022a Numerical research on the instabilities of CLT propeller wake. *Ocean Engng* **243**, 110305.
- WANG, L., LIU, X., GUO, J., LI, M. & LIAO, J. 2023 The dynamic characteristics in the wake systems of a propeller operating under different loading conditions. *Ocean Engng* **286**, 115518.
- WANG, L., LIU, X. & WU, T. 2022b Modal analysis of the propeller wake under the heavy loading condition. *Phys. Fluids* **34** (5), 055107.
- WANG, L., LUO, W. & LI, M. 2022c Numerical investigation of a propeller operating under different inflow conditions. *Phys. Fluids* **34** (10), 105118.
- WANG, L., WU, T., GONG, J. & YANG, Y. 2021 Numerical simulation of the wake instabilities of a propeller. *Phys. Fluids* **33** (12), 125125.

- XIONG, Y., ZHANG, K., WANG, Z.-Z. & QI, W.-J. 2016 Numerical and experimental studies on the effect of axial spacing on hydrodynamic performance of the hybrid CRP pod propulsion system. *Chin. Ocean Engng* **30** (4), 627–636.
- YANG, J. & BALARAS, E. 2006 An embedded-boundary formulation for large-eddy simulation of turbulent flows interacting with moving boundaries. *J. Comput. Phys.* **215** (1), 12–40.
- ZHANG, Y., CHENG, X. & FENG, L. 2020 Numerical investigation of the unsteady flow of a hybrid CRP pod propulsion system at behind-hull condition. *Intl. J. Nav. Archit. Ocean* **12**, 918–927.
- ZHANG, Y.-X., WU, X.-P., ZHOU, Z.-Y., CHENG, X.-K. & LI, Y.-L. 2019 A numerical study on the interaction between forward and aft propellers of hybrid CRP pod propulsion systems. *Ocean Engng* **186**, 106084.